Nanotube and nanowire devices

Thesis by

Ali Husain

In Partial Fulfillment of the Requirements for the

degree of

Doctor of Philosophy

CALIFORNIA INSTITUTE OF TECHNOLOGY

Pasadena, California

2004

(Defended May 13, 2004)

Acknowledgements

First and foremost, I would like to thank my advisor, Prof. Axel Scherer, for his guidance through the years of thesis work, his patience, and the freedom to explore diverse areas of science. Without the opportunity he gave me, I would not be here today. There have been many group members that have encouraged, consoled and taught me. David Barsic has been a colleague and friend since the beginning. Oskar Painter took me under his wing when I first started in research. Joyce Wong has listened no matter what I needed to talk about. I also want to thank all the members of Axel's group who have come and gone, particularly Mark Adams and Terrell Neal. Our group admin, Kate Finnigan has frequently lent me support.

I would also like to thank Prof. Michael Roukes for treating me as a member of his group, his collaboration and encouragement. I have learned many things from his group, particularly Inna Kozinsky who's cheerful attitude and depth of insight I could not have done without. Also, Henry Huang and Warren Fon have helped me in many situations in the clean room.

Special thanks go out to three postdocs (at the time): Jim Hone, Mladen Barbic and Henk Postma. I have learned so much about science, research, and life from these three people. Whenever I ran into a problem, one of them would help me find a way out.

Finally, I want to thank my family. My parents supported me no matter what happened and my siblings just helped me to relax when I needed to.

Abstract

The microelectronic revolution has spawned many fields that take advantage of the incredibly small size devices that can be made. However, the limits of photolithography and even electron beam lithography are fast approaching. Future progress in miniaturization of electronics, mechanical devices and optical structures will require new processes and materials.

The work presented in this thesis is an investigation into the possibilities of using new nanomaterials to fabricate simple devices. It is a challenge to integrate these materials with traditional microfabrication techniques. The processes commonly used to make electronics can damage or destroy some nanomaterials. Also, it is difficult to place and orient these novel substances. Finally, at the nanometer scale, different physical properties emerge due to confinement effects and the large surface-area-to-volume ratio.

We have fabricated devices out of carbon nanotubes and electrodeposited nanowires. The nanowires have been fabricated in gold, platinum, silver and nickel. For all the nanowires except silver we have measured the temperature dependence of the resistance and found that it is consistent with bulk metals. We have created and tested crossed nickel nanowires for magnetoresistive effects and found none.

From the platinum wires we have fabricated and tested the first doubly clamped resonator fabricated out of “bottom-up” materials. This resonator has much lower Q than comparable devices made by traditional techniques. The resonator also exhibits non-linear behavior well described by the Duffing oscillator.

From carbon nanotubes we have created a doubly-clamped beam. In addition, we have created a novel carbon nanotube field emission device with integrated grid. Work is ongoing to achieve experimental results from these devices.

The appendix describes photonic crystal defect cavity lasers, which offers interesting potential for integration with nanotubes and nanowires.

Table of Contents

List of Figures

List of Tables

Chapter 1

Introduction

Though comprising a variety of experiments using several different nanomaterials and involving various physical effects involving a range of different branches of physics, this thesis is unified by several common themes. All of the projects described use nano-scale materials that generally have a wire or tube-like geometry. In some cases, the nanowires are the key element in the device, while in one situation the nanowires play an important part in the fabrication of the device. Another unifying theme is the hybrid fabrication techniques employed in these projects. The nanowires or nanotubes are fabricated using bottom-up techniques, which result in random distributions of the nanomaterials. A recent challenge has been to integrate these materials with top-down fabrication techniques common to the semiconductor industry such as lithography, etching and deposition.

It is important to investigate methods to bridge top-down fabrication and bottom-up materials, to make useful devices. To be useful, nano-signals have to be transduced to the scale of humans and their machines.

As material and device dimensions shrink, the surface area to volume ratio decreases linearly. An increasing percentage of the atoms are at surfaces or junctions, causing properties to deviate from bulk.

The next chapter describes the fabrication and properties of the metallic nanowires used for several projects. We made basic measurements of their electrical transport properties using a four probe measurement. Finally, several unsuccessful projects are described as well as some unexplored ideas.

Chapter three details the most successful of my experiments, the study of a nanowire based very-high-frequency mechanical resonator. This device exhibits nonlinear behavior, which becomes increasingly important as the size of resonators continues to shrink.

Chapter four describes another nanomaterial I gained experience in—carbon nanotubes. The history and properties of carbon nanotubes is described, then several projects involving this material are described, each of which had interesting issues with fabrication and integration. One project is an attempt to create an integrated CNT field-emission device. Finally, I will describe attempts to create and measure a CNT mechanical resonator, an effort that is still in progress by my collaborators.

The appendix covers a seemingly unrelated project of the fabrication and measurement of photonic crystal laser defect cavities. However, the integration of photonic crystal structures and nanomaterials could yield tantalizingly interesting devices for completely new applications.

Chapter 2

Metallic nanowires:

properties and devices

2.1 Introduction

A key component of the approaching nanotechnology revolution will require high aspect ratio nanomaterials for a variety of applications such as electrical interconnects, optical waveguides and mechanical resonators. Since the 1980's, a simple technique for making micron and sub-micron diameter wires has been known.[1] This technique makes use of porous membranes as a template in which to deposit the metal of choice. The pores restrict the size and shape of the material being deposited, with the diameter of the wires determined by the diameter of the pores. This technique can be applied to porous membranes of materials such as glass[2] and anodized alumina[3], as well as various polymers[4,5]. For the wires used in our experiments, metal was electrodeposited into a commercially available polycarbonate membrane (SPI Supplies, West Chester, PA), which is available in a variety of pore sizes. The nanowires that resulted from this process had diameters from 20 to 60 nm, though most were close to 40 nm with lengths from 1 to10 μm. We have created nanowires out of gold, platinum, nickel and silver and

made efforts to integrate them into a variety of devices described in the sections of this chapter. One type of device in particular, a mechanical resonator, is fully described in Chapter 3.

2.2 Fabrication

Nanomaterials offer novel challenges with respect to their fabrication and integration. Generally, nanowires, regardless of material, cannot be synthesized monolithically, i.e., in the exact location and orientation required on a substrate with preexisting structures. Alternative techniques must be utilized to fabricate useful devices from these "bottom-up" materials and integrate them with "top-down" processes, a theme which runs through this work. The next section will describe how we make the nanowires and the next explains our primary method of accessing them with top-down processing.

2.2.1 Nanowire synthesis

The process to create metallic nanowires, brought to Prof. Scherer's group by postdoc Mladen Barbic, starts with a commercially available polycarbonate membrane with nominal pore size of 20 nm. A layer of gold (thickness 100 nm) is thermally evaporated onto one side of the membrane. It is important that the gold layer completely blocks the pores. The opposite side of the membrane is placed into contact with a commercially available plating solution for the desired metal (Technic, Cranston, RI). Figure 2.1 depicts the plating setup. A current source drives the metal to plate onto the gold layer, through the pores, with a current of 1-100 μA (typically 10 μA). The plating

runs for several hours, depending on what length of wires is desired. Once plating is completed, the membrane is removed from the solution and carefully washed with water and isopropyl alcohol. Gentle sonication in isopropyl alcohol removes the evaporated gold coating from the membrane. Finally, to release the wires, the membrane is dissolved in chloroform, resulting in a suspension of metallic nanowires.

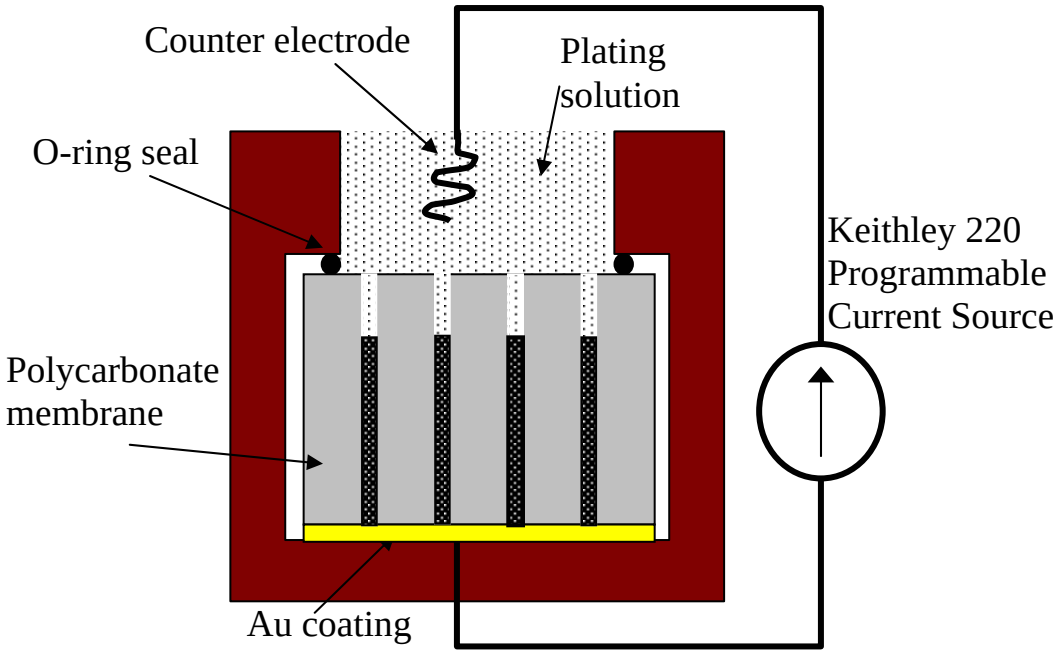

Figure 2.1: Diagram of process to synthesize metallic nanowires in porous membranes.

A variation on this process yields single-crystal silver wires.[6] In this variation, the electrical driving is unnecessary. A commercially available silver enhancement solution (Ted Pella, Redding CA) containing silver ions provides the material. This solution spontaneously deposits single crystal silver on any gold or silver surface. Silver enhancement has been commonly used to enhance the visibility of gold nanoparticles in the tagging of biological molecules. Silver is of particular interest for optical applications due to its property of low loss at the localized plasmon resonance frequency, which is

occurs at visible wavelengths. The resonance frequency is heavily influenced by the size of the particle at nanometer scales.[7] Due to the plasmon resonance, silver nanoparticles glow brightly when imaged by optical microscopy.[8]

Variations and combinations of these processes have the potential to make more complex structures than homogeneous cylinders of metal. For example, by changing the plating solution after only partially filling the holes, one can grow heterowires, composed of more than one metal with a well defined boundary between them. One could imagine a making a nano-thermocouple with an appropriate junction.[9] By overplating, i.e., over filling the pores, mushroom shaped structures would result. The isotropic deposition of Ag can yield other interesting structures, an example of which will be described in Section 2.5 below.

2.2.2 Making electrical contact to nanowires

It is important for many potential applications of metallic nanowires to be able to carry out electrical measurements upon them. For example, it is well known that the resistance of carbon nanotubes changes depending on what gas is adsorbed on the surface. Electronics also offers fast signal transfer, high data rates and a large variety of components and devices that can be used to create measurement circuitry. Finally, future researchers will be able to integrate nanomaterials with on-chip electronics for signal processing or feedback.

We developed a process to fabricate electrical contacts to single, isolated nanowires, depicted schematically in Figure 2.2. A Si wafer with thermally grown

silicon dioxide (SiO_2) is pre-patterned with both large gold pads using photolithography and alignment marks using electron-beam lithography. The substrate was chosen to provide electrical isolation. In each of these steps, 5 nm/80 nm of Cr/Au is evaporated onto the patterned resist and then lift-off is performed by soaking in acetone, leaving the pattern in metal (Figure 2.2a). Next, a suspension of nanowires in chloroform is dried on the sample one drop at a time, depositing the nanowires randomly on the surface as in Figure 2.2b. The wires can be seen in an optical microscope due to their strong light scattering properties.[10] The nanowires are mapped relative to the alignment marks and then e-beam lithography, evaporation and lift-off complete the process leaving a nanowire with electrical contacts patterned on it (Figure 2.2c).

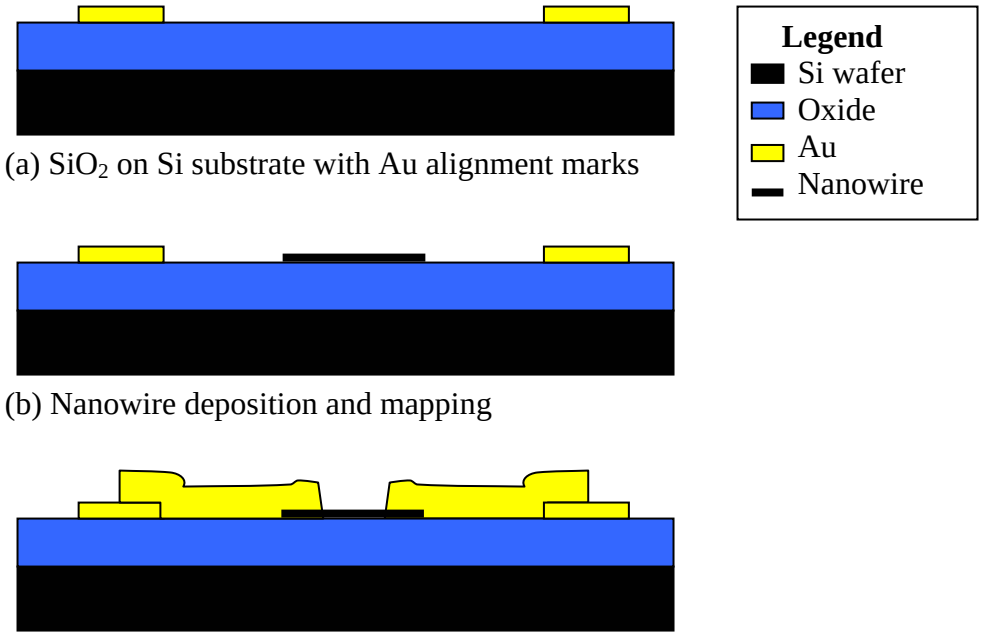

(a) SiO_2 on Si substrate with Au alignment marks

(b) Nanowire deposition and mapping

(c) E-beam lithography, evaporation and lift-off

Figure 2.2: Fabrication process to make electrical contact to nanowires.

We tried many different methods to make electrical contact to the silver wires, including depositing a variety of metals such as Cr/Au, Ti/Au and Pt, in-situ milling before evaporation, and post-annealing. Nearly every attempt measured as an open circuit across the wires. Unfortunately, electrical contacts were extremely difficult to make to the silver wires, possibly because of sulfides that form on the surface of the wires. The smog problems of the Los Angeles area are well known; this may have caused the wires to tarnish all the way through before they could be measured. Taking an Ag lattice spacing of ~.4 nm, the typical wire is only about 100 atoms across. Often, SEM pictures would show crumbled, broken pieces, as in Figure 2.3.

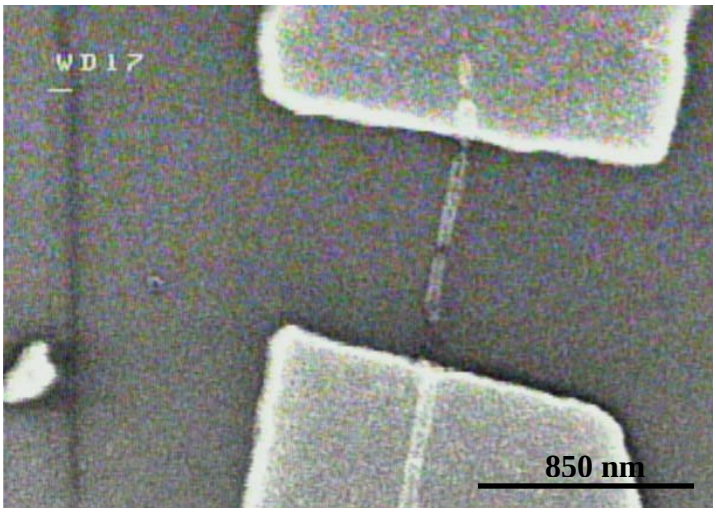

Figure 2.3: SEM image of broken silver wire.

It should be noted that the nanowires we worked with were very sensitive to electrostatic discharge. Often, in the absence of rigorous controls, the wires would act as nano-fuses, melting and severing the circuit, as shown in Figure 2.4. To protect the wires when they were initially characterized, personnel wore grounding wristbands and

employed a make-before-break switch sequence when lowering probes onto the chip. These precautions eliminated destruction of gold and platinum wires on the probe station. However, nickel wires were particularly hard to protect and would break unexpectedly and inexplicably. Nickel, possibly due to oxides, also had very high contact resistance, hindering experiments in many samples.

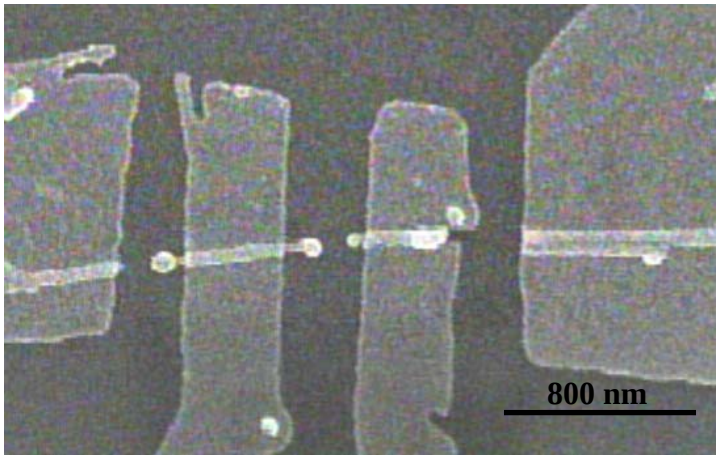

Figure 2.4: SEM picture of platinum nanowire broken by electrostatic discharge.

2.3 R vs. T measurements of nanowires

As an initial experiment, and to characterize the wires, leads were attached to the nanowires in a four probe configuration. Four-probe electrical measurement allows us to measure the resistance of the wires free of contact and lead resistance. Figure 2.5 shows a schematic of four probe electrical measurement. A current source is connected to the outer two electrodes. The flow of current produces a voltage drop through the wire, which is measured with a voltmeter at the inner two electrodes. In this way the effects of contact resistance and lead resistance are excluded from the measurement of the voltage

drop. To create a simple current source, a 10 MΩ resistor was placed in series with the nanowire. As long as the two probe resistance of the wire is much less than10 MΩ, this is a valid circuit to deliver a known current to the nanowire. All the samples for which data is shown had a two probe resistance, which includes the contact resistance, less than 10 kΩ. The digital lock-in amplifier used put out periodic voltage spikes for calibration so low pass filters, each with cut-off frequency of 1 kHz, at the input and output were included. For the measurements presented here, a 13Hz AC current of 100 nA (V_{out} = 1 V) was applied by the lock-in amplifier.

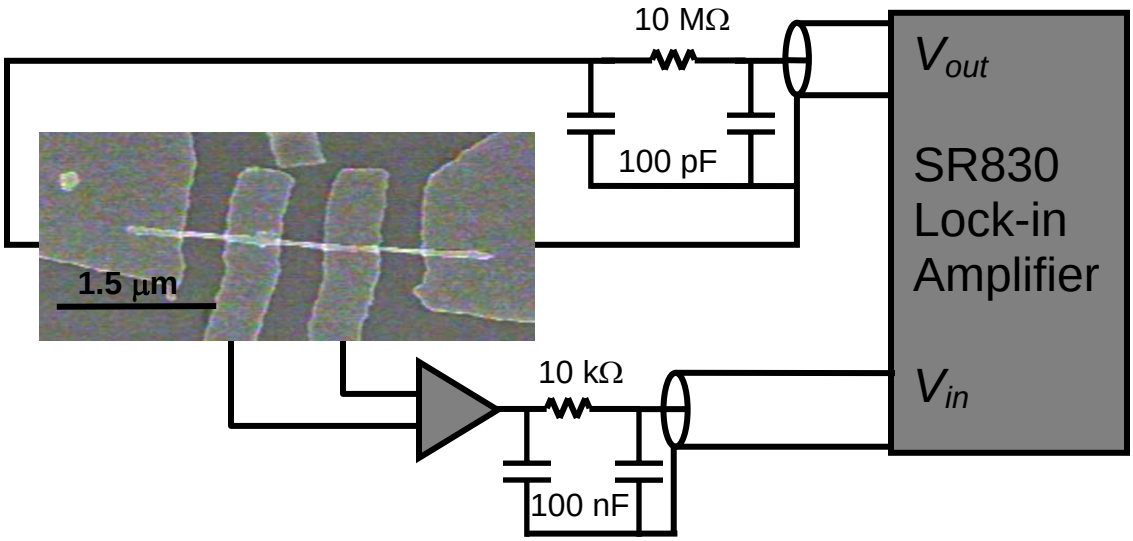

Figure 2.5: Four-probe electrical resistance measurement setup for nanowires with bias resistor and preamplifier.

The samples were loaded into a cryostat, pumped out to about 1 x 10^{-5} torr, which included a heater and temperature sensor. The cryostat was cooled using liquid helium, and allowed to stabilize at 4K. Then the resistance of the wires was measured, as a function of temperature. Figure 2.6 displays the results for gold, platinum, and nickel.

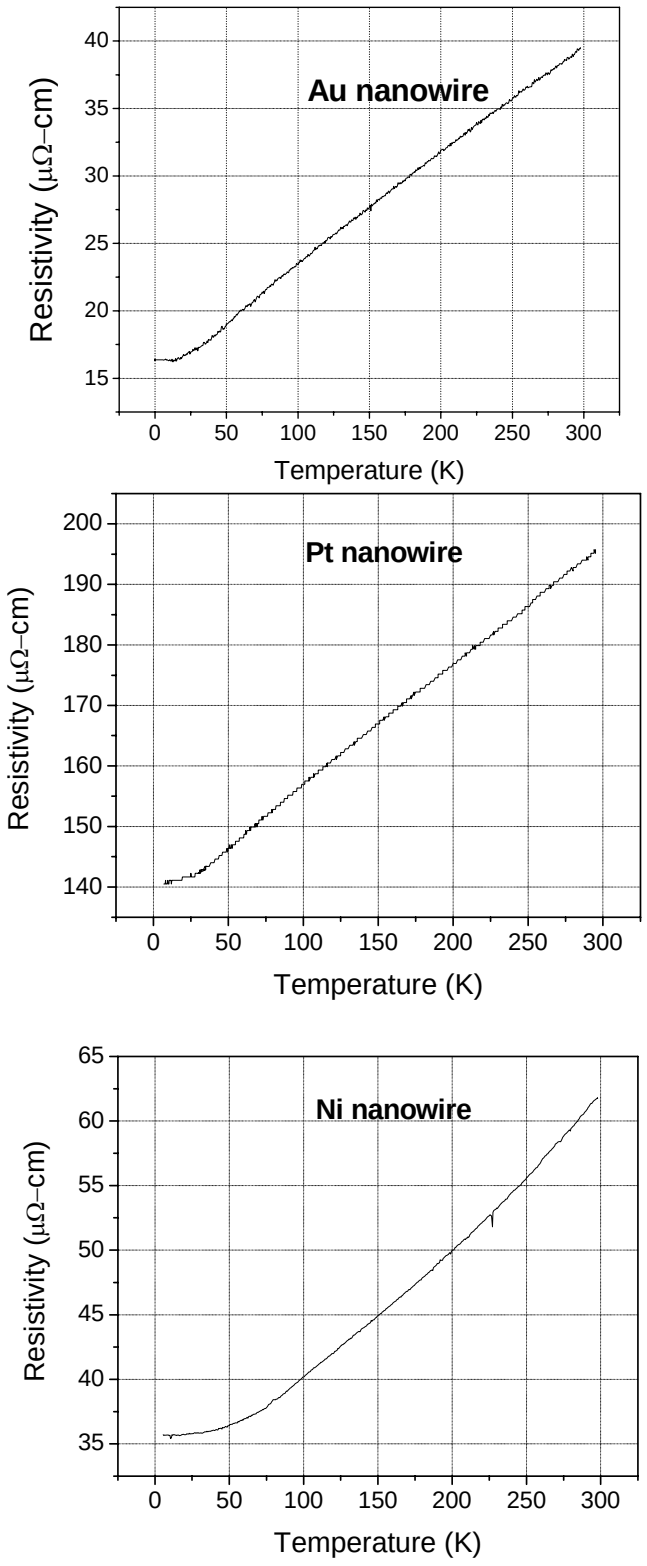

Figure 2.6: Resistivity vs. temperature for Au, Pt and Ni nanowires.

The bulk resistivities at room temperature of Au, Pt, and Ni are 2.4, 10.6 and 8.7 μΩ-cm.[11] Each sample tested displayed a resistivity about an order of magnitude larger than the bulk values. There are several possible reasons for this discrepancy. The plating process creates polycrystalline wires, which would increase the resistivity. Additionally, impurities arising from the plating solution would have the same effect. The small size of the wires may also come into play, with increased resistance from surface states, relative to the bulk conduction.

In metals, at room temperature lattice vibrations, or phonons, are the dominant scattering mechanism for electron transport.[12] At low temperature, phonon states are unpopulated and scattering is dominated by grain boundaries and impurities. For all the metals tested, the resistivity saturated at low temperature once the phonons had frozen out, as expected for metals. As described in Section 2.1, we were not able to produce results for silver due to problems creating contacts to the silver nanowires, possibly due to the development of sulfides.

2.4 Magnetoresistance and crossed magnetic nanowires

Nanomagnetic materials have application in data storage media and spintronics. Hard drives and other magnetic storage technologies are a $100 billion/yr industry, based upon the alignment and detection of nanomagnets to store and retrieve information.[13] Magnetic nanoparticles have been used for data storage since the time of tape drives. However, only recently have researchers been able to probe single nanomagnetic particles through the magneto-optical Kerr effect, magnetic force microscopy and other

techniques. In this work, electrical transport acts as a probe of the magnetization of nanoparticles.

Research into spin transport, as well as new magnetic materials, has spawned spintronics, a new field analogous to electronics, but where charge is replaced by the spin of the electrons. Also, manipulation of spins is currently recognized as a plausible method of scaling up quantum computing to a large number of bits.[14] A large amount of research is being done in magnetic semiconductors[15], magnetic junctions[16], and spin injection for devices such as spin-valve transistors.[17] Research into magnetic tunnel junctions has led to innovations such as a magnetic random access memory (MRAM) by IBM, which has a very low power consumption compared to electronic circuits, as well as a very short boot-up time.

To realize such future technology, nanoscale anisotropic magnetic effects must be understood to improve data storage densities and advance the field of spintronics. Ferromagnetic materials can serve as a source of spin-polarized electrons.[18] Nanowires of nickel, which is ferromagnetic, are an ideal structure to study nanoscale physics and to fabricate and measure simple devices. Wires of multiple metals, lithographic contacts and other junctions can be used to study interactions of spin, magnetization, and electron transport.

Magnetization and magnetic fields interact with electron transport in a number of ways, many of which can be placed under the heading of magnetoresistance, several types of which are relevant to this work. Anisotropic magnetoresistance (AMR) is an effect where the resistance of a magnetic material is related to the relative directions of the magnetization, M, and the current, J. The resistance is lower if M is perpendicular to

J, and higher if *M* is parallel to *J*. Tunneling magnetoresistance (TMR) can be measured in structures where the current tunnels from a magnetic metal through an insulating material to another magnetic metal. The resistance is dependent upon the relative orientation of the magnetizations. So called ballistic magnetoresistance (BMR) may play a part in the structures presented here. BMR occurs at nano- or atomic-scale point contacts between ferromagnetic electrodes. It is not clear if ballistic transport actually takes place, though this effect can change conductance by several orders of magnitude.[19]

Shape and size play an important part in the magnetic properties of nickel nanowires. Due to their small size, nickel nanowires of the dimensions we fabricated are single domain magnets, uniformly magnetized along the wire, or easy, axis, with two possible stable magnetizations in the absence of an applied field. This property is referred to as shape anisotropy.

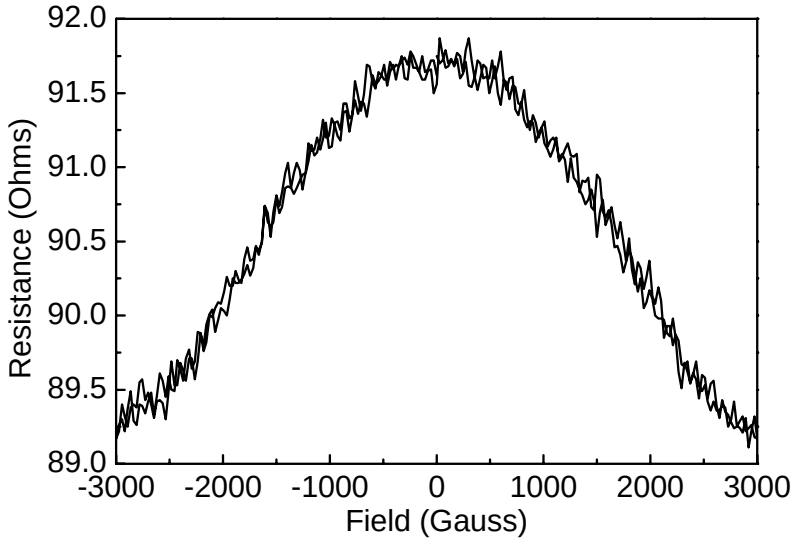

Figure 2.7: Resistance of nickel nanowire vs. magnetic field perpendicular to wire axis.

We measured the (AMR) of a single nickel nanowire. Using an electrical setup identical to Figure 2.5 above, with four contacts to the wire, the sample was placed in an electromagnet with the field oriented perpendicular to the axis of the wire. The resistance of the wire was recorded as the magnetic field was swept. Figure 2.7 plots the data. For a magnetic field orthogonal to current flow, the resistance of the wire decreases for increasing field, as has been reported previously.[20] The AMR can be explained briefly as follows. The magnetization *M* of the wire in the absence of a magnetic field is along the axis of the wire. As the field is increased, *M* tilts toward the field direction until the magnetization is aligned with the field. As *M* rotates, the resistance decreases until *M* is perpendicular to *J*, at which point the conductance saturates. The AMR is predicted to follow a cos^2B dependence for the magneto-resistance of a uniformly magnetized ferromagnet with respect to the applied field, and our measurements confirm this type of field dependence. In addition, an AMR value of ~2.5% is typical for nickel, and also matches well our measurement. Such a measurement therefore confirms that our nickel nanowire structure is a single domain magnet and behaves as expected when subject to an external magnetic field.

Crossed nickel nanowires give the possibility of creating a TMR spin-transport device where the relative magnetizations of the two wires can be varied continuously. Figure 2.8 shows the expected component of magnetization parallel to the magnetic field, $M_{||}$, vs. external field *B* for wires oriented parallel and perpendicular to *B*. A nickel nanowire cross could create a junction where spin polarized electrons travel from one magnetic domain to another through a possible tunnel junction due to oxidation of the wires. Ironically, oxidation may be to blame for the low yield in contacting nickel

nanowires. The resistance of the junction should decrease as the magnetization of the wires is aligned. In contrast to thin film techniques, template sythesized nanowires are cylinders. Laying one nanowire on top of another should create a very small contact area, introducing the possibility of observing BMR effects.

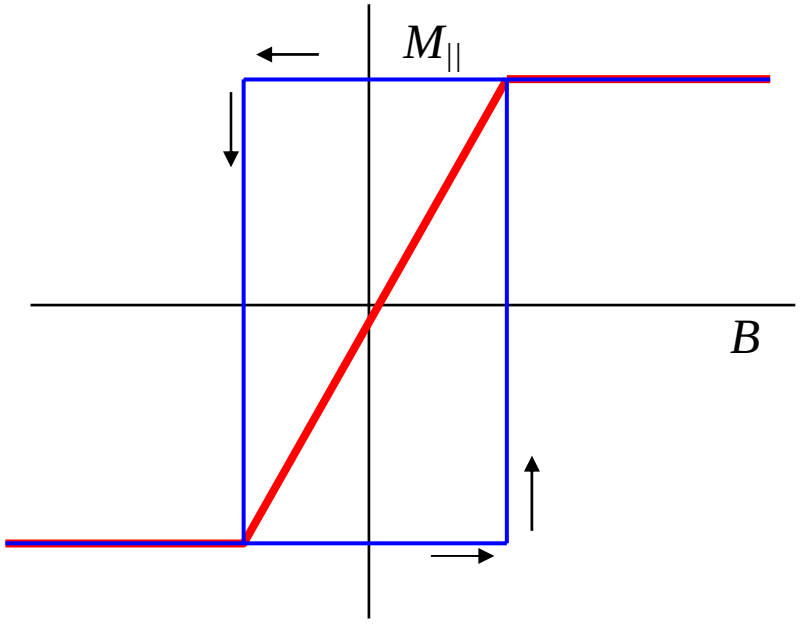

Figure 2.8: Theoretical parallel magnetization vs. magnetic field for nanowire oriented parallel (blue) and perpendicular (red) to magnetic field.

To create crossed nanowires, we begin with a suspension of nickel nanowires in chloroform. The suspension is gently washed over a thermal SiO2 on Si substrate in a magnetic field oriented parallel to the flow direction. This leaves Ni nanowires oriented parallel to the magnetic field deposited on the surface. The chip is turned by 90 degrees and the process is repeated. The result is as depicted in Figure 2.9, with Ni nanowires oriented in two perpendicular directions. Occasionally two nanowires will cross with enough overlap to place up to four contacts onto each wire.

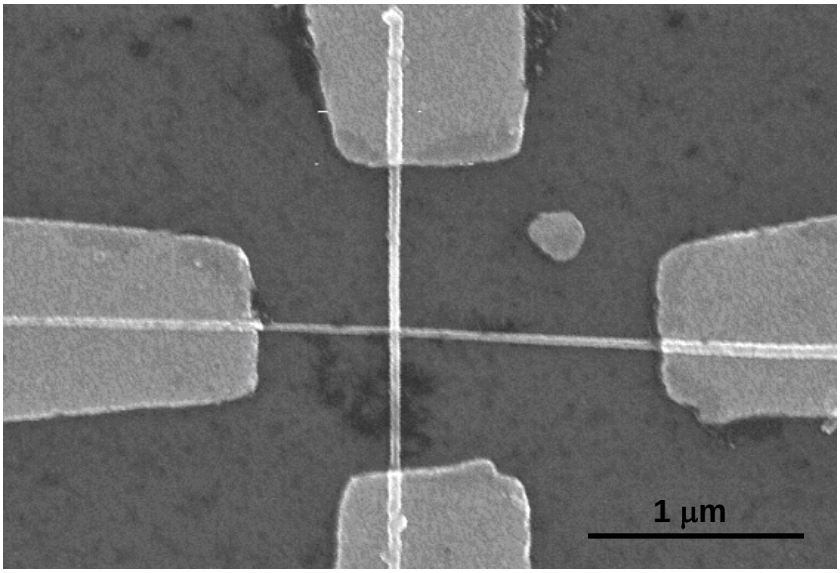

Figure 2.9: Crossed magnetic nanowires with microfabricated electrical contacts.

Very few devices had sufficiently low contact resistances for measurement. The yield was considerably reduced in the course of basic characterization and sample mounting. Of the devices that we measured in the cross configuration, we did not see any magnetoresistive effects at all. There is currently an ongoing controversy on the subject of atomic scale magnetic point contact with some groups observing dramatic effects, while others observing none. Our measurements fall into the second group.[21]

2.5 Magnetic nanowire resonator with plasmonic reflector

Motivation for nanoresonators is covered in depth in Chapter 3. Nanoresonator research often features structures that are actuated magnetomotively or capacitatively.

Here is described a proposal for a resonator fabricated using the methods described above that can be driven magnetically and detected optically.

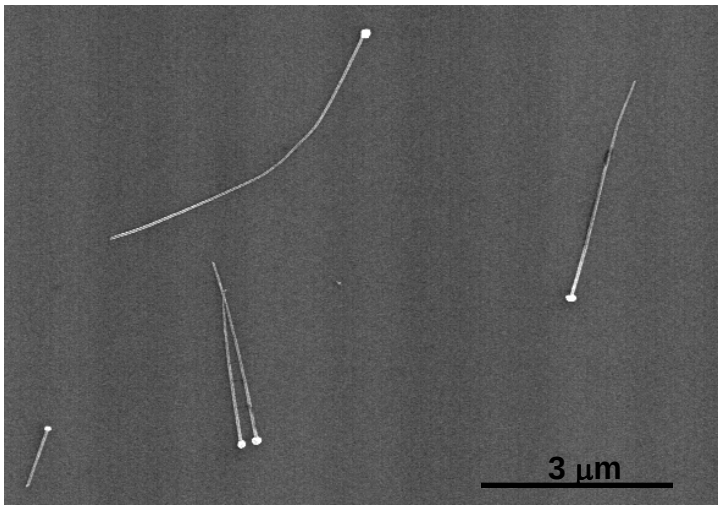

Figure 2.10: SEM picture of nickel nanowires with silver plasmonic reflectors

Beginning with the plating method described above, nickel wires were synthesized, taking care not to overplate the pores. Next, change the plating solution to Au, and plate it for a shorter time, to tip the wires in gold. Release the wires in chloroform and deposit them onto a substrate by gentle washing with the chloroform suspension. Place the substrate, with nanowires, into the Ag enhancement solution. The silver will deposit isotropically onto the gold tips forming a ball with very strong light scattering properties due to the plasmon resonance of silver. These have been fabricated here at Caltech, as shown in Figure 2.10.[8]

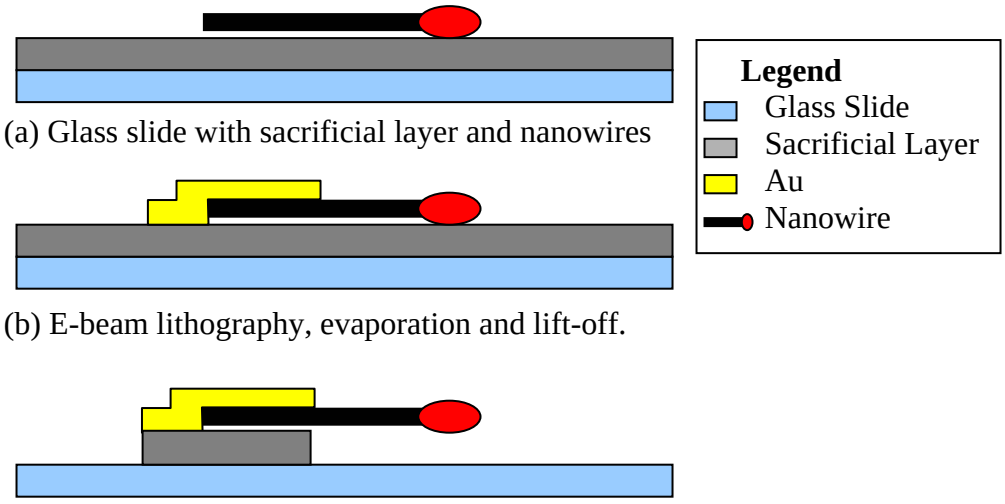

(a) Glass slide with sacrificial layer and nanowires

(b) E-beam lithography, evaporation and lift-off.

(c) Etch away sacrificial layer

Figure 2.11: Fabrication process for nickel nanowire resonator with plasmonic reflector.

Standard microfabrication techniques such as lithography, evaporation and etching can be employed to suspend the nanowire in a cantilever configuration with the silver sphere on the free end of the beam as shown in Figure 2.11. First the nanowires are deposited onto a glass slide which has had a 100 nm sacrificial layer deposited on the surface as in Figure 2.11a. The sacrificial layer could be Si, SiO_2 or even Si_2N_3. Electron beam lithography, evaporation and lift-off leave the wire clamped by one end on to the surface (Figure 2.11b). Finally the sacrificial layer is etched away leaving the nanowire cantilever (Figure 2.11c). Preliminary attempts to release it by isotropic dry plasma etching of a sputtered Si sacrificial layer were unsuccessful, as shown in Figure 2.12. An alternative method would be to use SiO_2 as the sacrificial layer and then perform a wet etch in hydrofluoric acid followed by critical point drying. Critical point drying evades surface tension effects that can damage a delicate suspended structure.

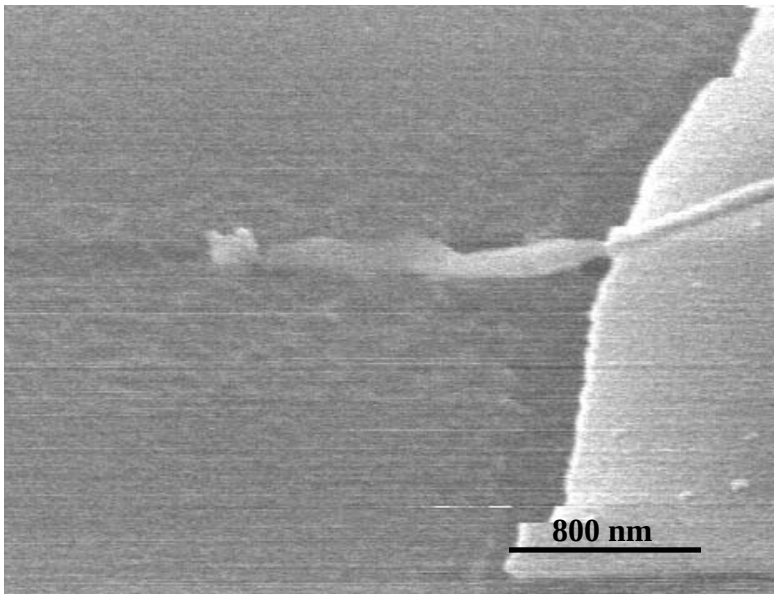

Figure 2.12: SEM picture of nanowire stuck to surface after isotropic dry etching in an attempt to create a cantilever device.

The silver nanosphere adds very little mass to the cantilever, yet presents a significantly increased scattering cross section due to its plasmon resonance when illuminated with visible light. Such a nanoparticle can serve as an efficient reflector for sensitive optical measurements. Because the Ni beam is a single-domain magnet, it can be actuated with a nearby electromagnet. To detect the oscillation, a laser would be reflected off the plasmonic silver ball. Figure 2.13 shows a possible experimental setup. The interface between the glass slide and vacuum provides a reflection that can be used with the reflection off the Ag ball to make a very sensitive interferometric measurement. An oil immersion lens prevents reflection from the first glass interface.[22]

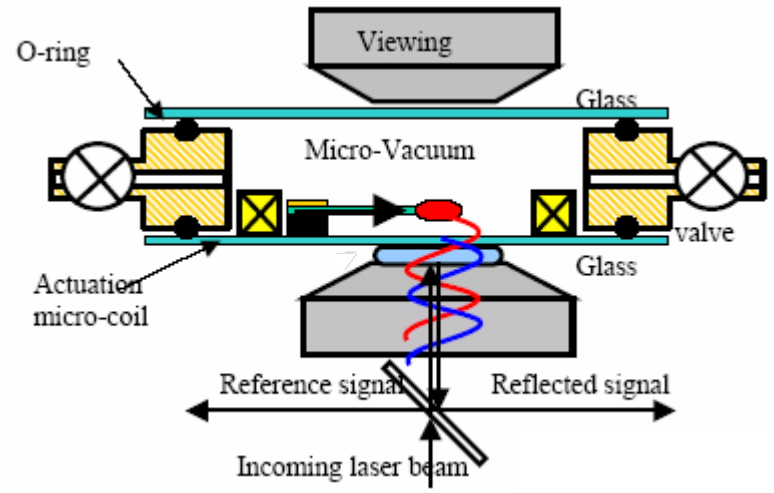

Figure 2.13: Schematic of proposed measurement setup for magnetic resonator.

2.6 Summary

Metallic nanowires are a useful and versatile bottom-up material for the development of interesting and novel devices. We have synthesized and measured the resistivity as a function of temperature of metal nanowires of gold, nickel and platinum. Though all the nanowires had resistivities larger than the bulk value for its metal, the temperature dependence was consistent with that observed in bulk metals.

Magnetic nanowire devices have been explored and the AMR of a single nanowire was measured. A crossed nickel nanowire device has been fabricated, though magnetoresistance effects were not observed. A novel nickel nanowire cantilevered resonator has been proposed. Further work is required to realize this device.

References

[1] C. R. Martin, "Nanomaterials - a membrane-based synthetic approach," *Science* **266** (5193), 1961-1966 (1994).

[2] R. J. Tonucci, B. L. Justus, A. J. Campillo et al., "Nanochannel array glass," *Science* **258** (5083), 783-785 (1992).

[3] H. Masuda and K. Fukuda, "Ordered metal nanohole arrays made by a 2-step replication of honeycomb structures of anodic alumina," *Science* **268** (5216), 1466-1468 (1995).

[4] T. M. Whitney, J. S. Jiang, P. S. Searson et al., "Fabrication and magnetic properties of arrays of metallic nanowires," *Science* **261** (5126), 1316-1319 (1993).

[5] T. Thurn-Albrecht, J. Schotter, C. A. Kastle et al., "Ultrahigh-density nanowire arrays grown in self-assembled diblock copolymer templates," *Science* **290** (5499), 2126-2129 (2000).

[6] M. Barbic, J. J. Mock, D. R. Smith et al., "Single crystal silver nanowires prepared by the metal amplification method," *Journal of Applied Physics* **91** (11), 9341-9345 (2002).

[7] U. Kreibig and M. Vollmer, *Optical properties of metal clusters*. (Springer-Verlag, Berlin ; New York, 1994), pp.xx, 532.

[8] J.J. Mock, D.R. Smith, M. Barbic et al., "Spectroscopic studies of individual plasmon resonant nanoparticles," *Proceedings of SPIE* **5221**, 66-75 (2003).

[9] L. Shi, O. Kwon, A. C. Miner et al., "Design and batch fabrication of probes for sub-100 nm scanning thermal microscopy," *Journal of Microelectromechanical Systems* **10** (3), 370-378 (2001).

[10] J. J. Mock, S. J. Oldenburg, D. R. Smith et al., "Composite plasmon resonant nanowires," *Nano Letters* **2** (5), 465-469 (2002).

[11] *CRC handbook of chemistry and physics*. (CRC Press, Cleveland, Ohio, 1977), p.v.

[12] Charles Kittel, *Introduction to solid state physics*, 7th ed. (Wiley, New York, 1996), pp.xi, 673.

[13] S. X. Wang and A. M. Taratorin, *Magnetic information storage technology*. (Academic Press, San Diego, 1999), pp.xxxii, 536.

[14] Y. Ohno, D. K. Young, B. Beschoten et al., "Electrical spin injection in a ferromagnetic semiconductor heterostructure," *Nature* **402** (6763), 790-792 (1999).

[15] H. X. Tang, R. K. Kawakami, D. D. Awschalom et al., in *Physical Review Letters* (2003), Vol. 90, pp. art.no.-107201.

[16] F. G. Monzon, H. X. Tang, and M. L. Roukes, "Magnetoelectronic phenomena at a ferromagnet-semiconductor interface," *Physical Review Letters* **84** (21), 5022 (2000).

[17] D. J. Monsma, R. Vlutters, and J. C. Lodder, "Room temperature - Operating spin-valve transistors formed by vacuum bonding," *Science* **281** (5375), 407-409 (1998).

[18] M. L. Roukes, "Electronics in a spin," *Nature* **411** (6839), 747-748 (2001).

[19] N. Garcia, M. Munoz, and Y. W. Zhao, "Magnetoresistance in excess of 200% in ballistic Ni nanocontacts at room temperature and 100 Oe," *Physical Review Letters* **82** (14), 2923-2926 (1999).

[20] J. E. Wegrowe, D. Kelly, A. Franck et al., "Magnetoresistance of ferromagnetic nanowires," *Physical Review Letters* **82** (18), 3681-3684 (1999).

[21] E. B. Svedberg, J. J. Mallett, H. Ettedgui et al., "Resistance changes similar to ballistic magnetoresistance in electrodeposited nanocontacts," *Applied Physics Letters* **84** (2), 236-238 (2004).

[22] M. Barbic, A. Husain, and A. Scherer, presented at the Nanoscale/molecular mechanics, Maui, Hawaii, 2002 (unpublished).

Chapter 3

Platinum nanowire resonator

The most complete of my projects was the fabrication and measurement of doubly-clamped platinum nanowire resonators. It is complete in the sense that we conceived, fabricated, and measured this type of device and explained its behavior from theory. It is the first instance of a resonator fabricated from “bottom-up” materials. This device exhibited fascinating non-linear behavior which will become important to future research in nanomechanical resonators as dimension get even smaller.

3.1 Introduction

Fabrication and readout of mechanical resonators of increasingly small size is an active and interesting area of research, and critical for the development of high-frequency nanoelectromechanical systems (NEMS) for low mass, high sensitivity devices. Cutting-edge applications of NEMS require both high responsivity and ultrahigh-frequency devices for sensing applications such as sub-attonewton, high-frequency force sensing

and electrometry as well as fundamental physical studies of dissipation mechanisms and mechanical systems in the quantum mechanical regime.[1]

As NEMS shrink down to the single molecule regime, integration with top-down fabrication techniques will be a crucial challenge. Researchers typically employ these top-down techniques to create mechanical structures out of semiconductor materials such as silicon[2], silicon carbide[3], gallium arsenide[4] and aluminum nitride.[5] However, conventional techniques yield device dimensions that are limited by the resolution of electron-beam lithography, etch roughness, the synthesis of epitaxially grown substrates, and other factors. As a result, there has been much interest in fabricating devices from "bottom-up" materials such as carbon nanotubes[6] and semiconductor[7] and metal nanowires.[8] These bottom-up materials can be synthesized in diameters down to single-nanometers which is smaller than can be achieved with conventional e-beam lithography. These materials can be atomically perfect, reducing surface dissipation due to defects. These advantages and others have led researchers to investigate nanomaterials for a large variety of uses.

3.2 Nanoresonator fabrication

We have developed a process to locate nanomaterials randomly deposited on a substrate and to lithographically align to them, an example of which is shown in an SEM image in Figure 3.1, left. To do this, it is necessary to fabricate a grid and alignment marks on the chip before adding the nanowires. A PMMA bi-layer (2% 495 mol wt, 2% 950 mol wt) was spun at 5000 RPM onto the surface of the chip. The purpose of the bi-

layer is to create an undercut resist patter that will improve a later lift-off. The PMMA coated chip is baked on a hot plate at 180°C for 5 min. Electron-beam lithography is used to expose a grid pattern and alignment crosses on the chip. After developing the PMMA in 3:1 IPA (isopropyl alcohol):MIBK (methyl isobutylketone), 5 nm and 80 nm of Cr and Au, respectively, are evaporated onto the surface. The PMMA is removed with acetone in a lift-off process, leaving the metalized alignment marks and grid.

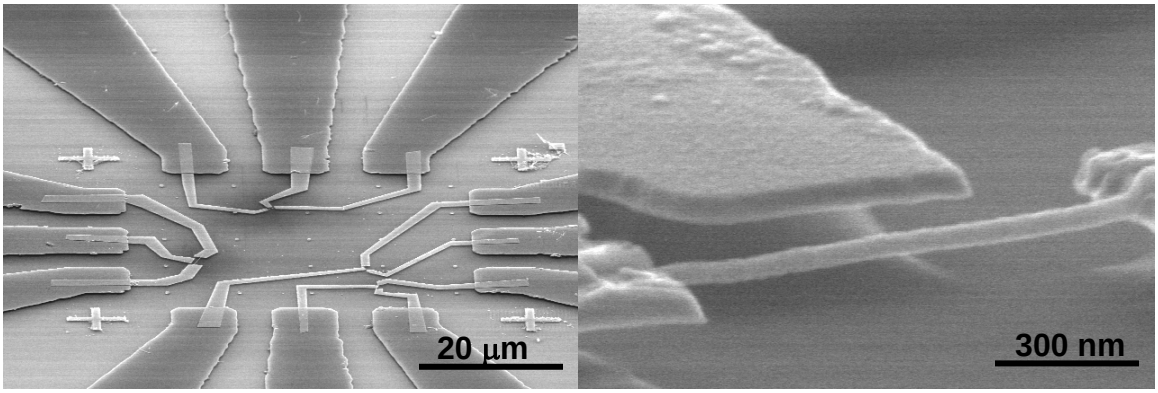

Figure 3.1: Left—low magnification image of pads, grid and alignment marks. Right—high magnification image of nanowire resonator.

To fabricate a suspended platinum nanowire, we first synthesize the nanowires by the electro-deposition method described in Section 2.1. Next, the wires are suspended in a solvent, chloroform, which dissolves the polycarbonate membrane. Drops of the suspension are deposited on a degenerately doped silicon chip with a 300 nm thick thermally grown silicon dioxide layer. As each drop dries, wires are left randomly distributed on the surface. To place electrical leads on the wires, we need to locate the positions of candidate wires. An atomic force microscope (AFM) is used to map the topology of the surface, revealing the position of nanowires with respect to the grid. The

mapping can also be carried out with an optical microscope because of the strong light scattering of the nanowires, but with much lower accuracy. A PMMA bi-layer is spun on, identical to the last, and contact leads are defined using electron beam lithography. Finally, Cr/Au is evaporated and lifted off, leaving a Pt nanowire which is electrically accessible. The nanowire is suspended by wet etching for 1 min in 8% buffered hydrofluoric acid, which etches about 100 nm. Critical point drying completes the process, avoiding the damaging effects of the surface tension of the evaporating solvent. The right image in Figure 3.1 shows the final device. The third electrode, not in contact with the wire, was meant to be a capacitive gate. It was not used in the initial experiment due to a broken electrical lead on the sample holder.

3.3 NEMS theory and measurement techniques

Mechanical resonance modes of cantilevers and doubly-clamped beams are well understood. Modeling as an unstrained doubly-clamped beam yields a predicted fundamental mechanical resonance frequency f_0 given by[9]

$$f_0 = \frac{22.4}{2\pi}\frac{R}{2L^2}\sqrt{\frac{Y}{\rho}}, \quad (1)$$

where Y is the Young's modulus, ρ is the density of the beam, R is the beam radius and L is the beam length. Using the bulk values for the Young's modulus and density of platinum (168 GPa and 21090 kg/m^3, respectively[10]) and the dimensions of a typical device (length of 1.3 μm and diameter of 43 nm), equation (1) predicts a fundamental

frequency of 64 MHz, so that experiments will be in the microwave regime. This turns out to be lower than the measured response; reasons for this will be discussed later.

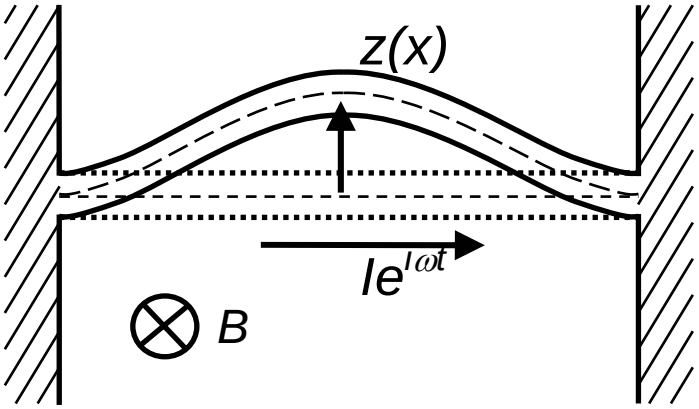

Figure 3.2: Schematic of magnetomotive actuation where *B* is the magnetic field, *I* is the current and *z* is the displacement of the beam.

In nanomechanical systems research, a common method of actuating and detecting such a device is the magneto-motive method pioneered in the group of Prof. Michael Roukes here at Caltech[2] and used by many others[11]. A diagram of this scheme is shown in Figure 3.2. In this technique, the resonator is placed in a large magnetic field oriented perpendicular to the beam. The resonator is integrated with a wire which is connected to electrical leads, through which an AC current is passed. The wire experiences a Lorentz force due to the time varying current in a magnetic field. At resonance, the resonator (and integrated wire) is moving through a magnetic field, producing a back electromotive field (EMF) that is detected as a change in the power delivered to the device. The back EMF will maximize when the frequency of the current through the resonator matches its resonant frequency. In standard top-down NEMS the current carrying wire is integrated into the structure by evaporating gold leads onto the

resonator. In contrast, in this hybrid bottom-up/top-down device, the resonator is the wire.

The resonator can be modeled as an *LCR* tank circuit with an intrinsic resistance that accounts for the intrinsic dissipation of the vibrating beam.[12] The value of the capacitance, inductance and resistance in this model can be written as,

$$C_m = \frac{m}{\xi l^2 B^2}, L_m = \frac{\xi l^2 B^2}{m}, R_m = \frac{\xi l^2 B^2}{\omega_0^2 m} Q, \quad (2)$$

respectively, where l is the length of the beam, m is the (effective) mass of the beam, B is the magnetic field, ω_0 is the natural frequency and ξ is a numerical factor (0.83 for the fundamental mode) that depends on the mode shape. The quality factor that appears in R_m is the unloaded Q, accounting for intrinsic dissipation within the beam. The circuit model for the resonator is shown in Figure 3.3 where R_e is the intrinsic electrical resistance of the nanowire, i.e., the two probe resistance of the wire including contact and lead resistance. In our R_e devices, was around 500 Ω.

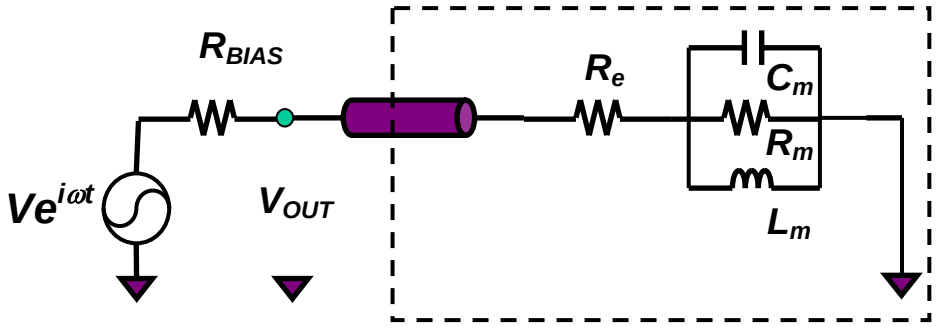

Figure 3.3: Electrical schematic showing measurement setup. All components within the dashed box are in a liquid He dewar at 4.2 K.

The method of detecting the reflected power is specifically designed for samples that are well matched to RF power generating equipment. Typical top-down NEMS devices have R_e~10-100 Ω and R_m~1 Ω while RF sources are generally designed to be impedance matched to 50 Ω. However, our devices have a resistance R_e at least one order of magnitude higher. A small change in the total resistance of the device, $R_e + R_m$, will result in very small change in the reflected power, requiring a modification of the method. In the traditional scheme, the drive and detected signal utilize the same port. Our modified circuit drives from one port, and detects the signal at the other terminal of the device. Figure 3.4 is the schematic of this alternate circuit. The input and output ports are 50 Ω terminated to eliminate reflections of RF power. Of course, this results in a loss of signal at the output due to the voltage division. It turns out that the 50 Ω resistor on the output side is not necessary because the transmission line is already matched to 50 Ω. The extra resistor reduces our output signal by a factor of two.

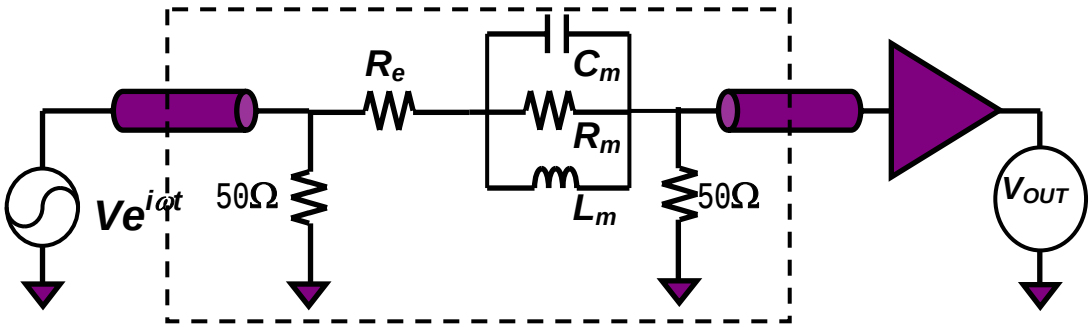

Figure 3.4: Electrical schematic of measurement circuit for high impedance samples.

With this electrical setup, the resonance appears as a dip in the transmitted power to the output port. The impedance of the resonator can be calculated by simple circuit

analysis. For a total resonator impedance $Z_S(f)$ >>50 Ω, the output voltage at the input to the preamplifier is

$$\frac{V_{out}}{V_{in}} \approx \frac{25\Omega}{Z_S + 25\Omega} \approx \frac{25\Omega}{Z_S} \text{ where } Z_S(f) = R_e + (L_m \,||\, R_m \,||\, C_m) = R_e + Z_m(f).$$

The factor of 25 Ω is due to the 50 Ω termination of the detect line in parallel with the 50 Ω input impedance of the preamplifier. The resonance appears on top of a large background signal which can be removed by dividing it out. We do this by estimating the background amplitude V_b at each point in the resonance using a linear approximation off of resonance. The electromechanical impedance $|Z_m(f)|$ can be easily extracted using the background from,

$$\frac{|Z_m(f)|}{R_e} \cong \frac{V_b - V_{out}}{V_b}. \quad (3)$$

The resonance curve indirectly measures the oscillation amplitude because the back EMF is proportional to the velocity of the beam. The displacement can be easily found by multiplying the left side of (3) by $V_{in}/\zeta Bl\omega_0$. This overestimates the displacement slightly because of unaccounted losses in the signal lines.

3.4 Nanowire resonator results

Due to the fact that the sample resonance is expected to be in the tens of megahertz frequency range, on chip cross talk between the signal lines is a problem. The impedance of the device is about 500 Ω, much greater than the 25 Ω seen at the output port. If the parasitic capacitive coupling impedance ($1/j\omega C$) between the input and output

lines is comparable to 25 Ω, then the RF signal will not pass through the resonator. To deal with this problem, the stray capacitance was minimized with a sample holder that surrounds the sample with ground planes.

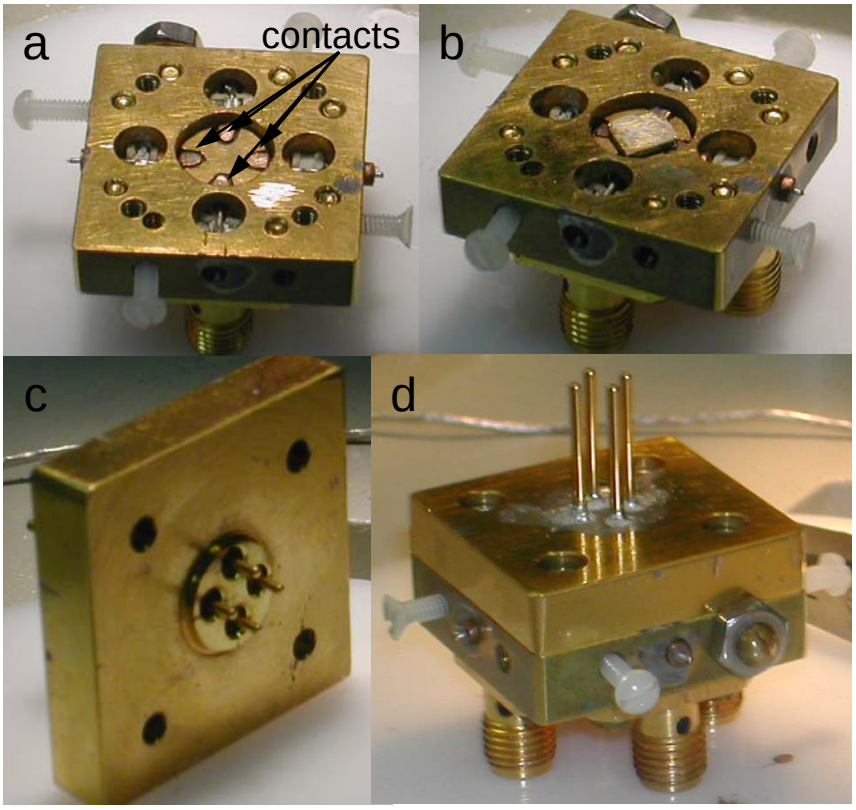

Figure 3.5: (a) Sample holder with four gold contact pads exposed; (b) Sample placed on indium beads to contact pads; (c) Cap with pogo-pins; (d) Assembled sample holder to fully shield sample (Images from Henk Postma).

The sample was mounted into a special sample holder, designed and constructed by postdoc Henk Postma, to prevent cross-talk between the signal leads. Figure 3.5 shows images of the sample holder. The sample is designed with Au leads and pads to contact the sample holder. To mount the chip with the resonator on it, first small beads of indium are placed on the contacts labeled in Figure 3.5a. Next, the chip is inverted

onto the contacts such that the on-chip pads lay on the indium beads (Figure 3.5b). The cap of the sample holder, shown in Figure 3.5c, is carefully placed over the top and fixed with screws (Figure 3.5d). The cap has spring loaded contact pins (pogo-pins) to place force on the chip to ensure good contact between the chip and the sample holder. In addition, the pins on the cap make contact to the back side of the chip. The degenerate Si of the wafer forms a ground plane only 300 nm from the device. The sample is entirely surrounded by a grounded, metallic structure, and the whole sample holder is Au plated for low resistance. Through launchers mounted on the holder, the resonator is electrically connected to RF cables to supply power to the device.

The mounted sample is placed into the vacuum space of a magnet cryostat which can be ramped up to 8 T. Since it is superconducting, the magnet and sample must be cooled with liquid He (4.2 K). The sample is protected by enclosing it in a metal dip stick that is evacuated to 1×10^{-6} torr. The dipper must be evacuated due to the low temperature that the experiment is operated at. Pumping it out prevents gas from condensing on the sample, potentially destroying the device or damping the mechanical resonance. Operating the resonator at low pressure also increases its quality factor due to the lack of damping from air molecules.

After mounting, we measured the resonance characteristics using the technique described above. A network analyzer provides the stimulating RF current to actuate the sample as well as the meter to detect the transmitted signal. By sweeping the frequency of the current, we can locate the resonance and characterize its properties.

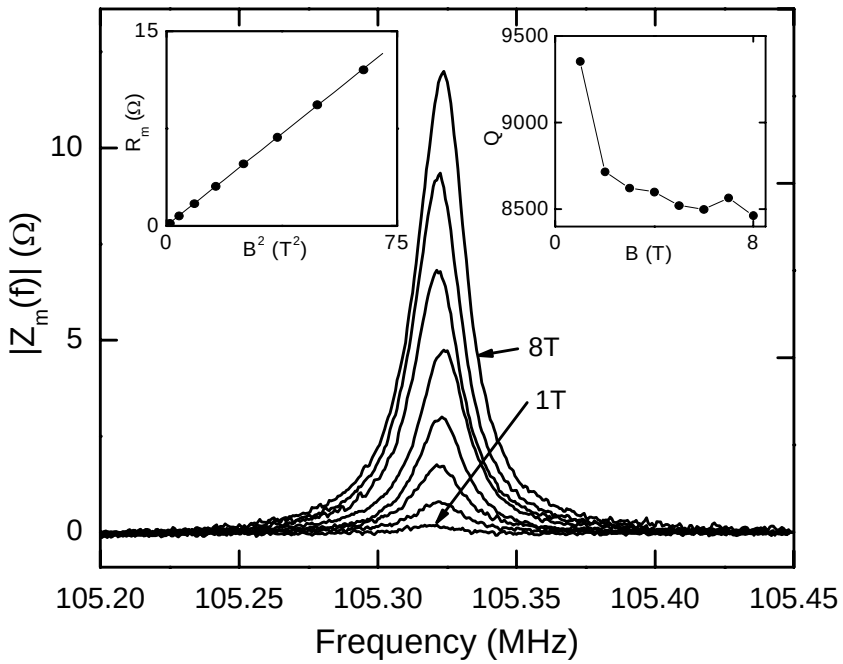

Figure 3.6: Electromechanical impedance vs. frequency for platinum nanowire resonator for increasing magnetic field. Inset Left—B^2 dependence of peak electro-mechanical impedance. Inset Right—quality factor vs. magnetic field.

The resulting curves are plotted in Figure 3.6. Plotted in the left inset, the electromechanical impedance increases with a B^2 dependence, characteristic of magnetomotive drive as predicted by equation (2). The quality factor decreases with increasing magnetic field, as shown in the right inset of Figure 3.6. Some of the decrease can be explained by dissipation of the back EMF through the output resistance it sees. This resonator has a quality factor higher than that of other, "top-down" fabricated beams of comparable size. Carr *et al.*,[13] for example, measure quality factors for single crystal Si beams and find that Q decreases from about 3000 for beams with a surface area-volume ratio of 0.02 nm^{-1} to a value of 1000 for devices with a ratio of 0.06 nm^{-1}. The nanowire device described here possesses a surface area-volume ratio of 0.095 nm^{-1} and *Q* of 8500, highlighting an advantages of bottom-up materials—lower surface dissipation. Smaller

materials have a large surface area to volume ratio, and hence greater dissipation from surface states. Top-down fabrication processes can cause damage and defects such as etch roughness that increase surface dissipation.

The frequency of the beam is nearly a factor of two larger than the predicted frequency of 64 MHz. Anecdotal evidence offers some clues as to the reason for this discrepancy. When the dipstick was placed into the liquid helium cooled dewar/magnet, the sample frequency gradually drifts higher until it stabilizes after several hours. This suggests that the frequency is affected by the temperature of the sample. The most likely explanation is that differential thermal contraction in the sample, namely between the metal layer and the Si/SiO_2 substrate, introduces tension into the beam, increasing the frequency. By taking the coefficients of linear expansion of Si and Au, the strain ε in the beam is estimated to be about 0.003. The tension T can be can be computed from $T = \pi r^2 \varepsilon Y$ and then taking an approximation of the frequency in the presence of tension,[14]

$$f_T = f_0 \sqrt{1 + \frac{L^2 T}{4\pi^2 Y I}}$$

where the moment of intertia $I = \pi R^4/4$. We find a predicted frequency of 94 MHz, in good agreement with the measurement.

When driven with a large enough AC current, the resonator begins to show non-linear characteristics, shown in Figure 3.7. The oscillation amplitude of the resonator shows a hysteresis in the frequency sweep, with the measurement shown in the inset. The details of the nonlinear behavior are fully described in the next section.

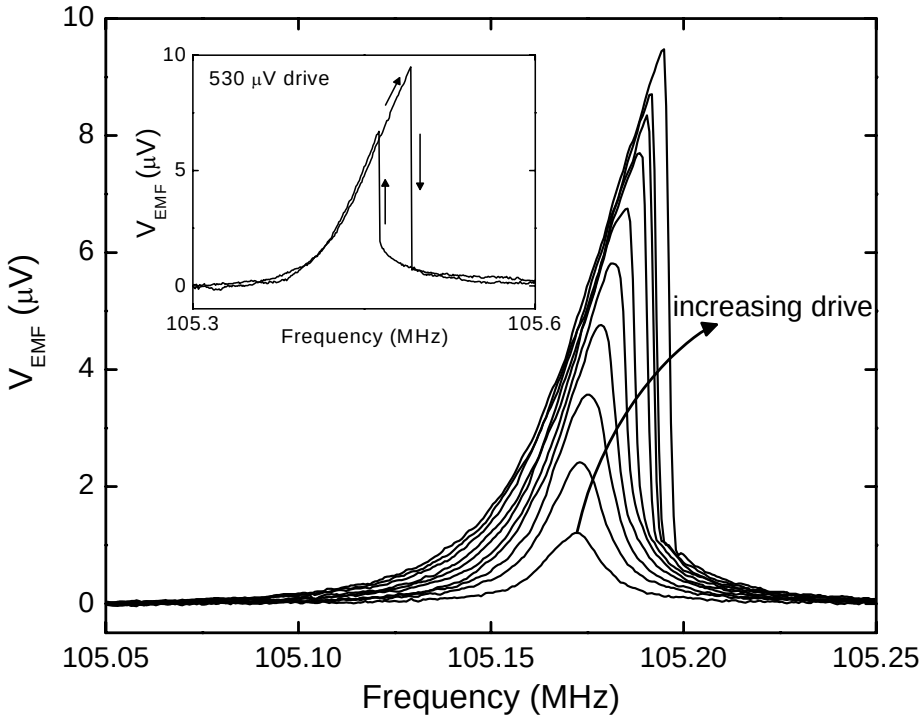

Figure 3.7: Back EMF vs. frequency showing transition to nonlinear resonance with increasing drive. Inset—hysteresis when sweeping frequency up and down.

Note that the resonance frequencies for the plots in Figure 3.7 and inset are different. The resonance would shift slightly if the temperature of the sample was cycled from 4 K to room temperature and back again.

3.5 Non-Linear Mechanical Resonance

In the previous section, we described the initial nonlinear effects measured from the nanowire resonator. This section will describe in detail the theory of the Duffing oscillator. We observed many of the behaviors covered in this section. The remainder of the sections in this chapter will describe further experiments where these effects were measured.

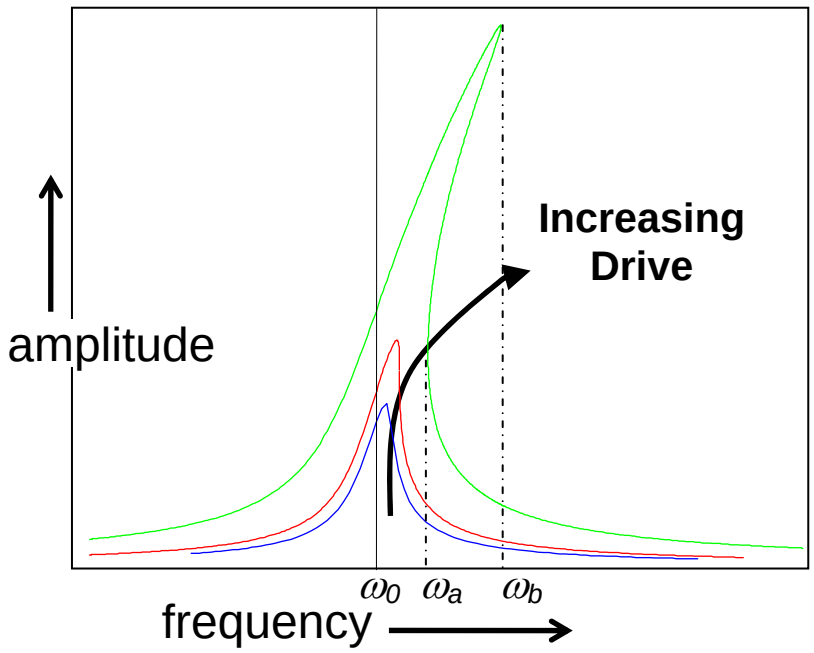

Figure 3.8: Oscillation amplitude vs. frequency for increasing drive strength. ω_o is the frequency in the absence of non-linear behavior.

The non-linear behavior observed arises from the increased tension of the beam as it resonates. At large amplitudes of oscillations the change in the beam length, i.e., the stress on the beam, at the extremes of the motion becomes significant, resulting in a periodically varying tension. Qualitatively, this increases the spring constant of the beam, shifting the resonance frequency, but also distorting the shape of the resonance curve. The increased spring constant increases the frequency, pulling the resonance curve peak to the right at large oscillation amplitudes. Figure 3.8 is a theoretical graph of this distortion for increasing drive amplitude showing the distortion in the resonance curve shape.

We can introduce nonlinearity into resonator theory in a number of ways. It is interesting to contrast the methods of Landau & Lifshitz (L&L)[15] vs. Nayef & Mook

(N&M).[16] Through two seemingly dissimilar methods, both derivations reach an identical equation to describe the Duffing oscillator. For full derivation, see references. I will briefly outline the method and result of each below.

L&L begin by considering the Lagrangian of an anharmonic oscillator expanded up to the fourth order nonlinear term,

$$L[x(t)]: \frac{1}{2}m\dot{x}^2 - \frac{1}{2}m\omega^2 x^2 - \frac{1}{3}m\alpha x^3 - \frac{1}{4}m\beta x^4,$$

and from it, derive the equation of motion which has a third-order restoring force. By successive approximate solutions to the equation of motion, they find a correction to the frequency that is second-order in the amplitude of oscillation. Finally, L&L substitute the correction into the solution of the linear equation of motion for a driven, damped harmonic oscillator to derive an equation that is sixth-order in the amplitude, *a*:

$$\kappa^2 a^6 - 2\varepsilon\kappa a^4 + (\varepsilon^2 + \lambda^2)a^2 = \frac{D^2}{4\omega_0^2} \quad (3)$$

where ε is the detuning from the linear frequency ω_0, *D* is the drive, κ is the non-linear coefficient, and λ is the damping constant.

In contrast, N&M begin with the Duffing equation, which is a directly driven system with cubic nonlinearity,

$$\ddot{x} + \omega_0^2 x + 2\varepsilon\mu\dot{x} + \varepsilon\alpha x^3 = \varepsilon k\cos[(\omega_0 + \varepsilon\sigma)t].$$

A method of multiple timescales is used to find an approximate solution. Taking the steady state in amplitude, frequency and phase, N&M derive a frequency response equation which is once again sixth-order in the amplitude, *a*:

$$\left[\mu^2 + \left(\sigma - \frac{3\alpha}{8\omega_0}a^2\right)^2\right]a^2 = \frac{k^2}{4\omega_0^2} \quad (4)$$

where σ is the detuning frequency from ω_0, k is the drive, α is the non-linear coefficient, and μ is the damping constant. Equations (3) and (4) are perfectly identical if one equates $\kappa = 3\alpha/8\omega_0$. It is somewhat remarkable and very comforting that these two authorities agree. By apparently different approximations L&L and N&M arrive at the same behavior for the Duffing oscillator. L&L's approach is much more intuitive and is derived from fundamental physics. N&M's method is basically an approximate solution to a non-linear differential equation. It is more analytical and also can be used to predict the non-resonant transients of a moving beam. Our measurements will show that the Duffing oscillator well describes the non-linear oscillation properties of our beam.

From the frequency response equation (4), one can describe the amplitude vs. frequency plot, often referred to as a "Tsunami" curve which is graphed in Figure 3.8. At high enough drive strengths, the curve pulls to the right (for $\alpha > 0$), creating a tri-valued region which, for the green curve, is between the frequencies ω_a and ω_b. A stability analysis shows that the middle branch of the three is unstable, so that in measurement a hysteresis is observed. When sweeping the frequency from low to high, the amplitude follows the upper branch until the frequency reaches ω_b, and then switches suddenly to the lower amplitude state. Similarly, the switch is from low to high amplitude is at ω_a when sweeping down in frequency.

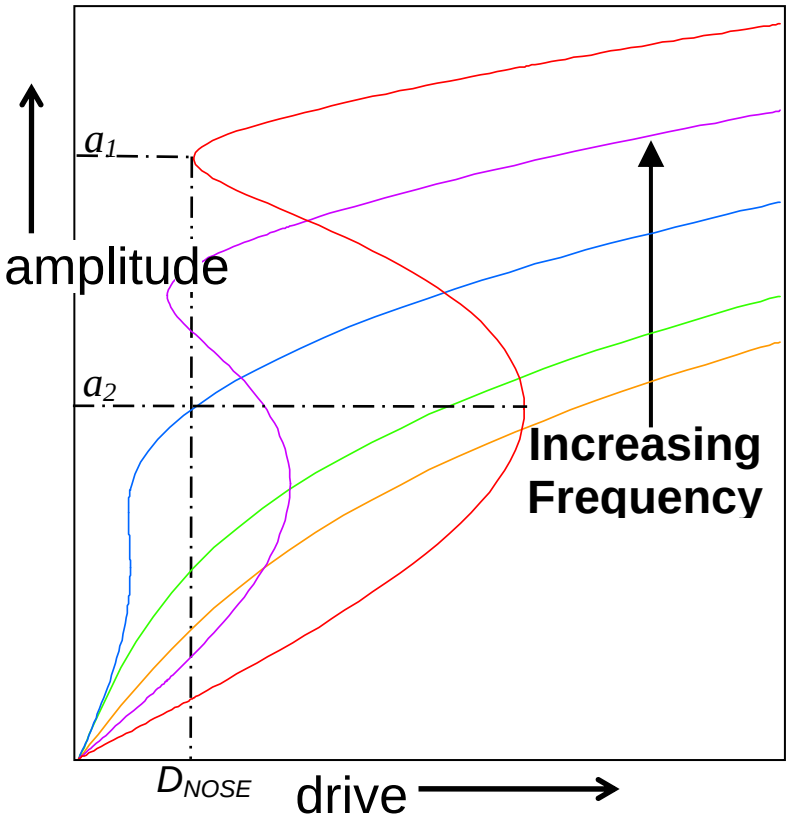

Figure 3.9: Amplitude vs. drive strength for increasing frequency from linear resonance frequency ω_0.

This hysteresis is visible in phase vs. frequency, output amplitude vs. drive amplitude, and phase vs. drive amplitude sweeps. The exact frequency or drive amplitude at which the resonator switches states is subject to some variation due to noise. Section 3.7 investigates this effect further. For a frequency sufficiently detuned from ω_0, as the drive is increased, the oscillation amplitude will switch to the upper branch discontinuously. Figure 3.9 shows the amplitude vs. drive for increasing frequency from the linear resonance frequency ω_0.

For the purpose of observing non-linear behavior such as the basins of attraction described in the next section, a second resonator was fabricated with length of about 2.2

μm, pictured in Figure 3.10. This beam has a predicted frequency of 26 MHz, but a measured frequency of about 45 MHz, probably because of differential thermal contraction of the sample, as observed similarly in the first resonator.

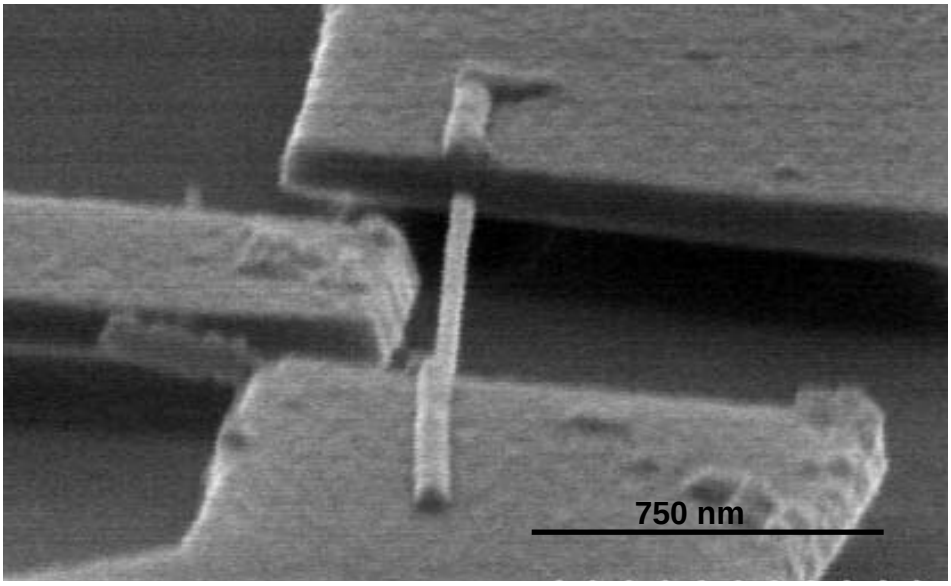

Figure 3.10: SEM image of resonator measured for non-linear studies.

The resonance behavior of this sample is shown in Figure 3.11. For increasing drive amplitude, the resonance curve becomes distorted and hysteretic behavior is observed, as expected. The right graph shows experimental verification of the hysteresis in phase. In each graph, the final two curves are at the same drive amplitude but with the frequency swept in the opposite direction, as indicated by the arrows. Experimentally, the sample can be arbitrarily prepared in the upper or lower stable states simply by sweeping the frequency or drive amplitude from the appropriate direction.

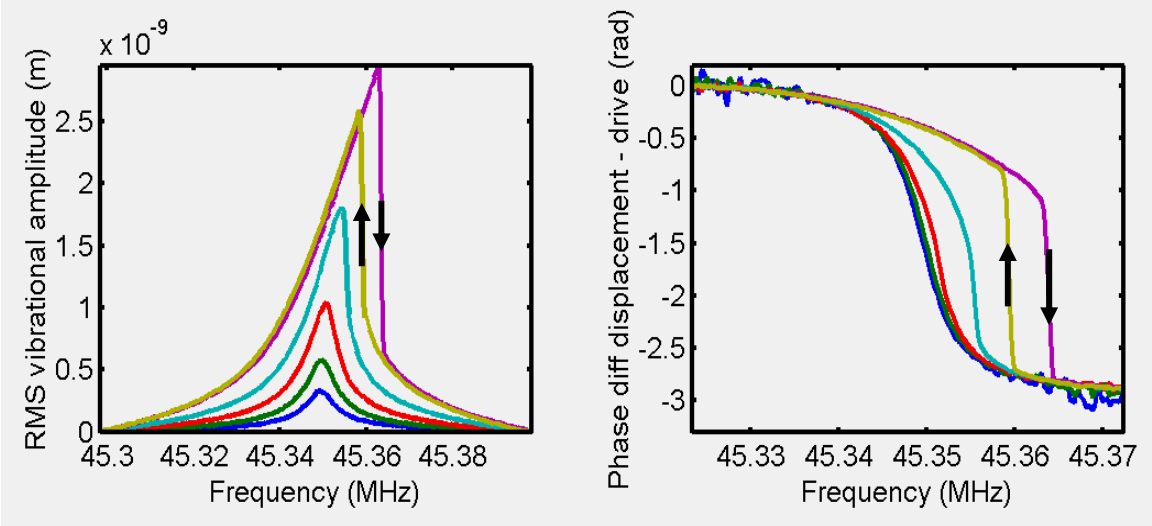

Figure 3.11: Left—vibration amplitude vs. frequency for increasing drive amplitude. Right—phase vs. frequency for increasing drive amplitude. The final two curves in each plot are at the same drive strength, but opposite sweep directions, indicated by the arrows.

3.6 Mapping of the state plane

At a drive larger than the critical drive and a frequency within the tri-valued region (between the frequencies ω_a and ω_b in Figure 3.8), one can plot the phase, with respect to the drive, and the amplitude of the resonator in a polar fashion. Figure 3.12, generated by our theoretical collaborator Oleg Kogan, shows such a plot, called a state plane, with an inset showing the resonance shape and frequency of interest. The three points marked (known as fixed points) correspond to the three points where the resonance curve intersects vertical line in the inset. The red curves indicate the path through phase space that the displacement would take if going from the unstable state B to one of the stable states, A or C. The "ying-yang" shape divides the plane into "two basins of attraction" corresponding to the two stable states. The boundary between the basins is

referred to as the separatrix. A resonator with initial condition of phase and amplitude within one of the basins will settle to the stable state within that basin.[16]

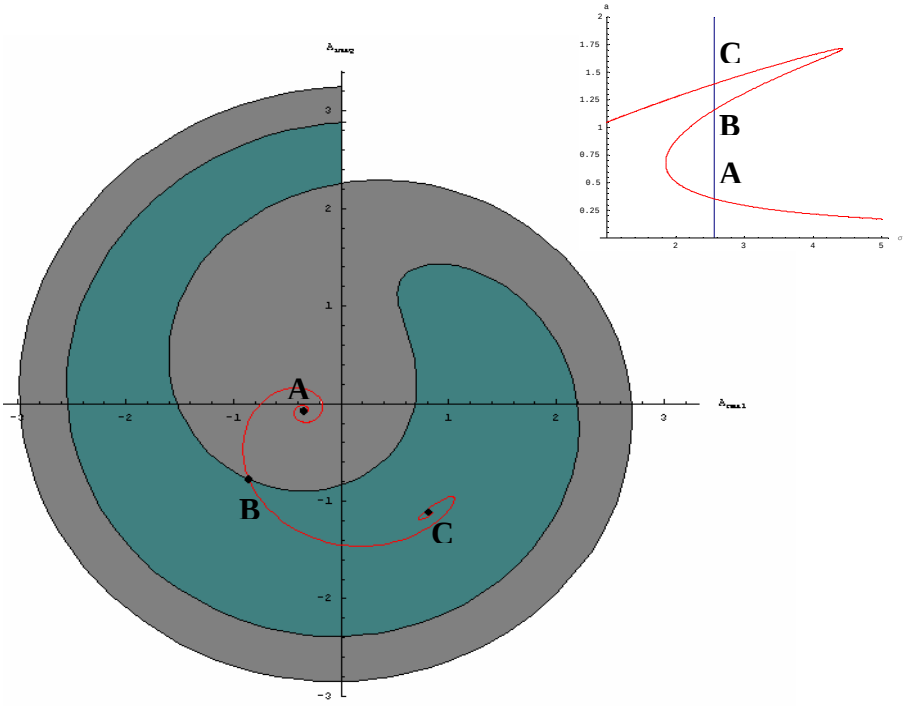

Figure 3.12: Theoretical plot of state plane of the Duffing oscillator. The axes are in-phase and out-of-phase displacement of the beam. Inset—Frequency corresponding to state plane, with respect to resonance curve.

One of our primary goals from research on non-linear resonator was to experimentally measure the separatrix and basins of attraction associated with the Duffing oscillator. The procedure for such a measurement begins with selecting an oscillation frequency for which the device has two stable resonance amplitudes for a large enough driving amplitude. The resonator is driven with some power at this frequency, and the amplitude and phase of the resonance is measured. Next, the drive signal is changed quickly to a final drive amplitude strong enough to produce bistability. The state of the resonator is measured to determine which of the two stable amplitudes

resulted. The relative phase of the two drive signals is varied, tracing a circle in the resonator phase plot. The schematic for this experiment is shown in Figure 3.13. Of particular importance in this setup is the switch that changes from the initial drive to the final drive. Attempts to achieve this measurement with a slower switch (Mini-circuits ZMSW-1211, switching time: 2 μs) were unsuccessful. It is important that the switch be faster than the oscillation frequency of the resonator. The one used (Mini-circuits ZASWA-2-50DR) has a specified switching time of 10 ns.

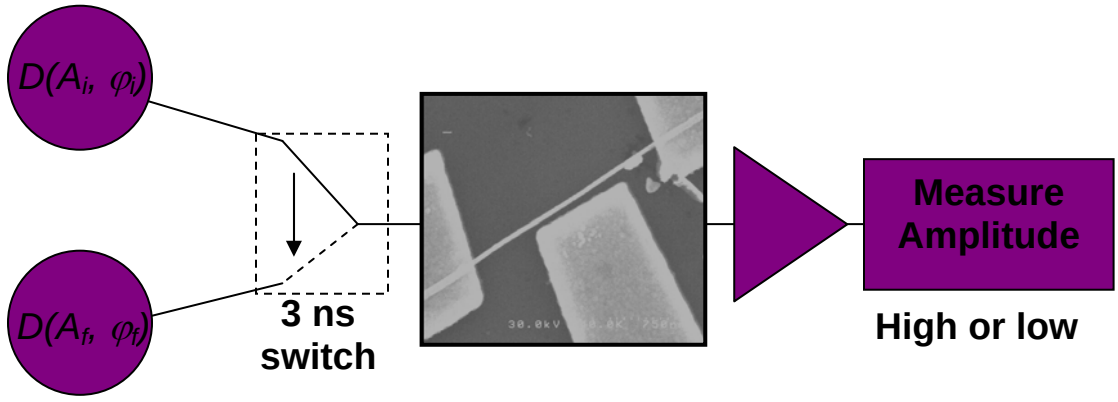

Figure 3.13: Schematic of measurement of basins of attraction of Duffing oscillator. The amplitude and phase of the resonator's drive signal is suddenly switched.

Figure 3.14 plots the data from this initial experiment. This data traces a circle in the phase space of the oscillator, centered at the origin. This is consistent, since the amplitude of the initial drive, and hence the beam displacement, was kept constant while the phase, with respect to the final drive signal, is rotated through 360 degrees. In this plot, one can see a clear transition between relaxing to the upper state and relaxing to the lower state after switching the drive signal.

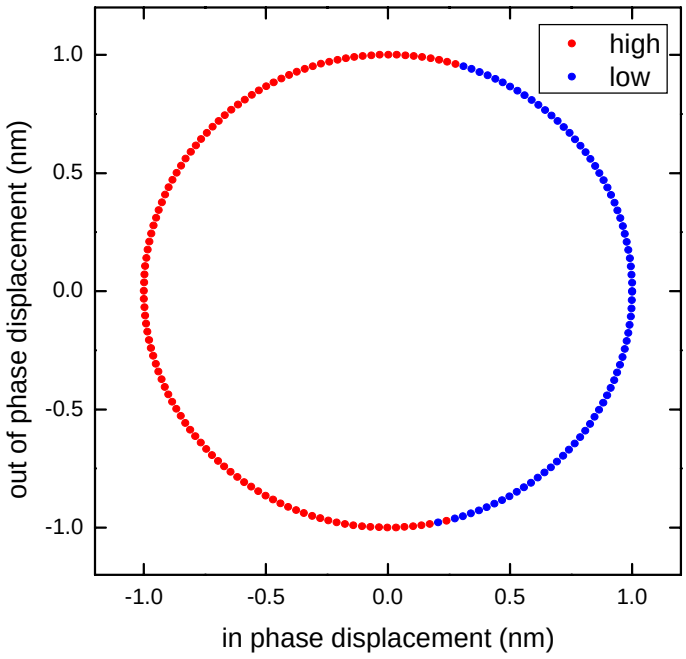

Figure 3.14: Resonator phase plot of final state with respect to initial phase for a fixed initial drive amplitude. To fully map the state plane the initial drive amplitude will be varied.

To map out the whole state plane, the data for Figure 3.14 was collected for a range of driving amplitudes. Figure 3.15 plots our first attempt to measure the basins of attraction of the resonator. There is a glaring gap in the initial amplitudes that we can access. This can be easily explained by referring to Figure 3.9. For the frequencies that exhibit hysteresis there is a range of amplitudes where there are no stable oscillation states. For example, for the detuning frequency corresponding to the red curve, there are not stable resonance amplitudes between a_1 and a_2 for any driving strength. Therefore, at this frequency we cannot access those amplitudes with the current electronic setup. This problem will be addressed later.

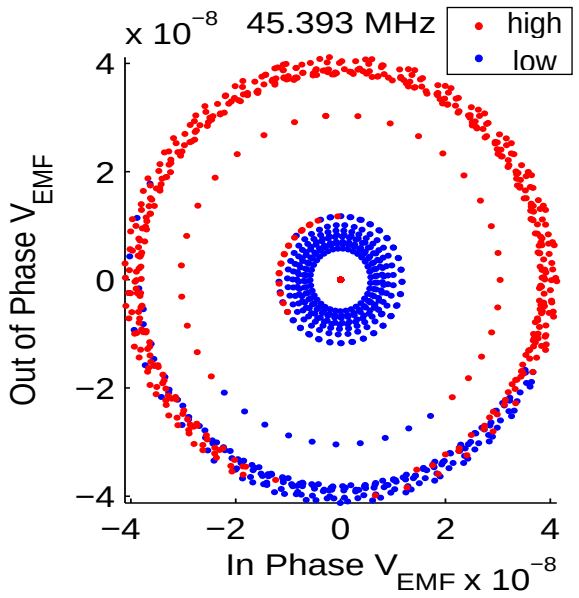

Figure 3.15: Experimental measurement of basins of attraction. Red and blue correspond to the high and low amplitude stable states, respectively.

We repeated the experiment of Figure 3.15 for multiple frequencies within the hysteretic region. As the frequency is changed, corresponding to moving across the hysteresis, the two basins of attraction should exchange area, as depicted in Figure 3.16. Toward the left side of the tri-valued region, the high amplitude state dominates the state plane. As the frequency is swept to the right the low amplitude basin increases in area at the expense of the other. Figure 3.17 shows experimental results of changing frequency. Indeed, the basin corresponding to the low amplitude final state (blue) increases in area at the expense of the high amplitude state (red).

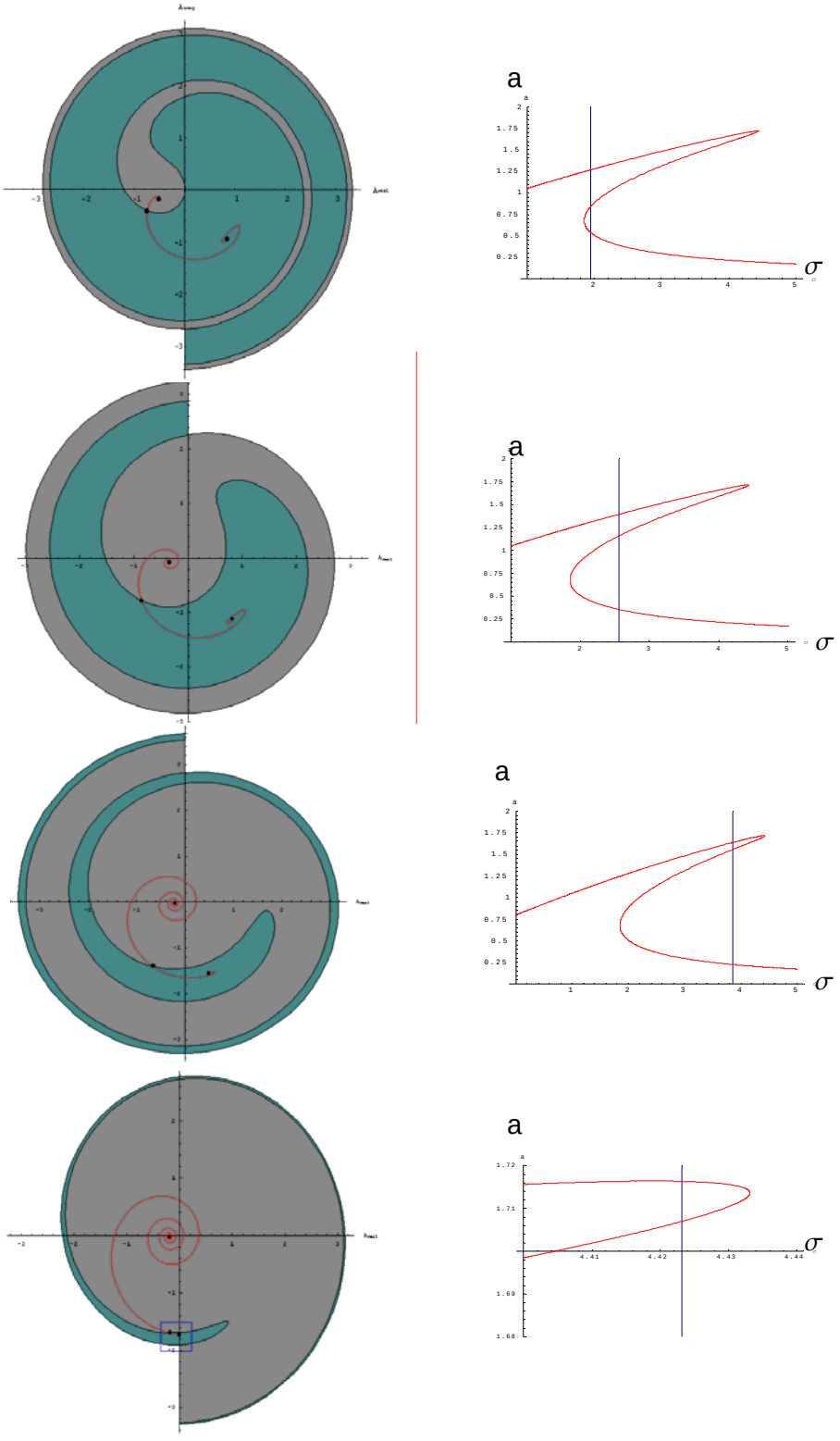

Figure 3.16: Exchange of area of basins of attraction as frequency is varied across tri-valued region (Images from Oleg Kogan).

We also expect an exchange of area when keeping the frequency constant and varying the final state driving strength. The results of the experiment are plotted in Figure 3.18. When increasing the driving strength, the Tsunami curve of Figure 3.8 stretches to the right so that both ω_a and ω_b increase. If the measurement is performed at fixed frequency, then decreasing the drive strength is similar to increasing the frequency in terms of the area exchange of the basins of attraction. The measurement bears this out.

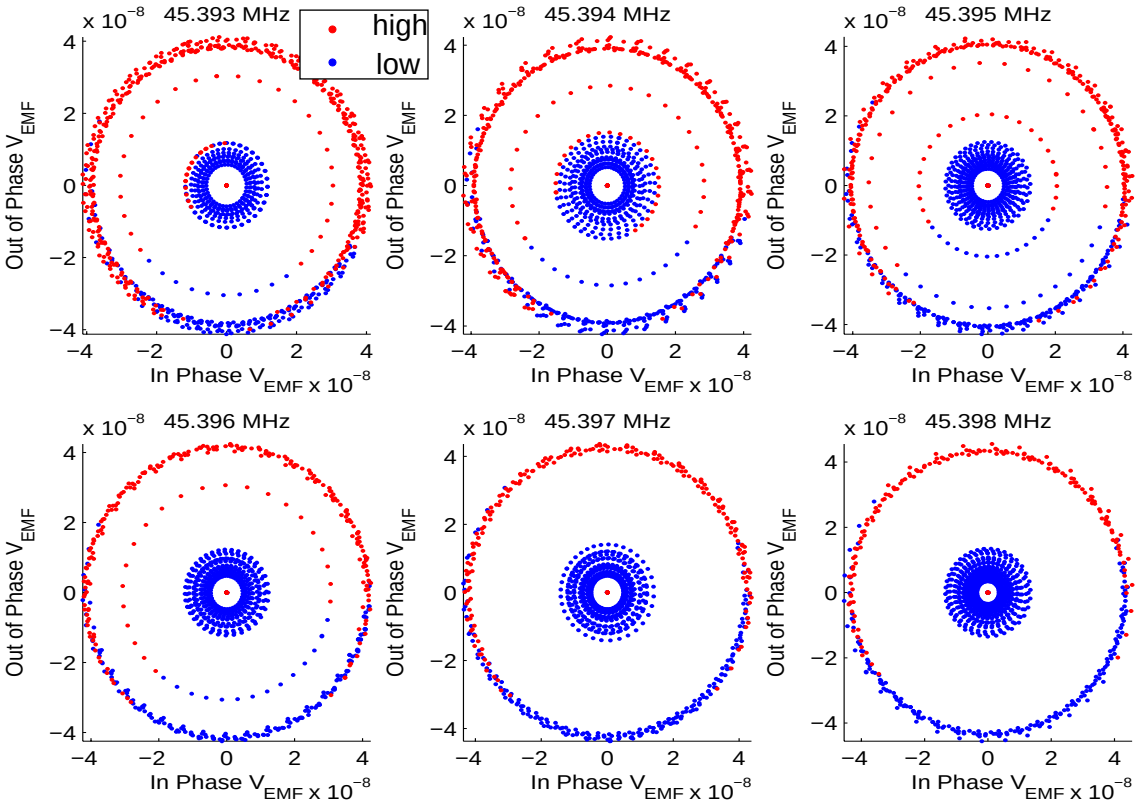

Figure 3.17: Experimental measurement of basins of attraction as frequency is varied through tri-valued region. As the frequency is increased, the low amplitude (blue) basin grows.

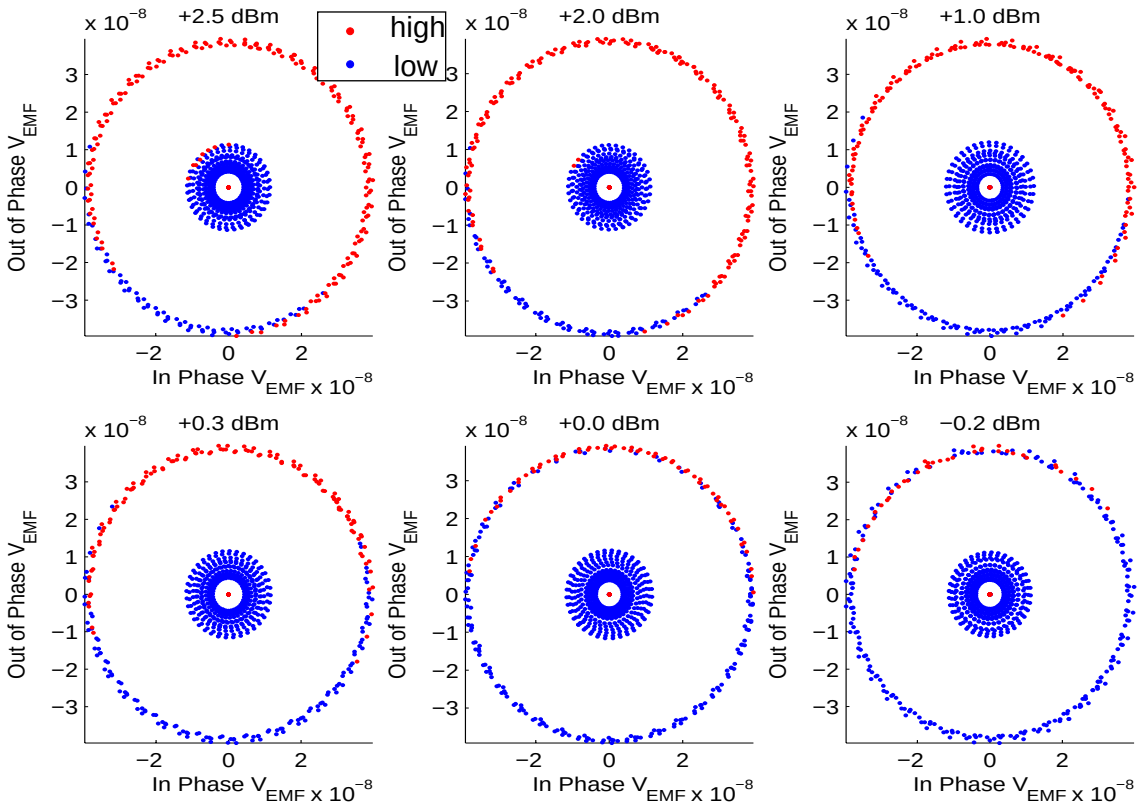

Figure 3.18: Experimental measurement of basins of attraction of resonator for decreasing drive strength. Drive strength is before attenuation. Drive strength at sample is about -70 dBm.

All the data plots of Figures 3.17 and 3.18 have inaccessible regions where there are no stable resonance amplitudes for any drive. However, we can access these regions by use of the gate to shift the frequency. Figure 3.19 plots the variation in the frequency for a DC bias applied either to the gate or directly to the nanowire, where in the latter case, the substrate acts as the gate. Applying bias the directly to the nanowire clearly has a much larger effect, most likely because the resonator has a larger capacitance to the substrate than to the side gate. The frequency decreases with applied voltage, though the result we would expect is not clear. The electrostatic force on the wire should increase its tension, increasing the frequency. However, the electrostatic force itself, when the

variable capacitance is taken into account, lowers the spring constant, decreasing the frequency. We do not understand the slight rise in frequency as very small bias voltages seen in both gate biased and wire biased data. The data indicates that the latter is the dominant effect.

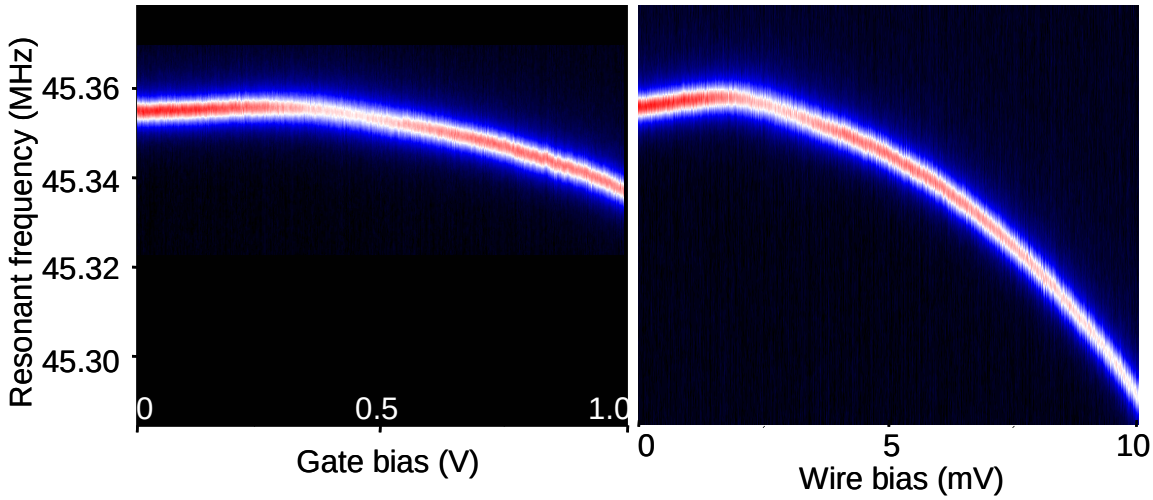

Figure 3.19: Frequency of resonance peak as a function of DC gate voltage. Left—bias on side gate. Right—bias on wire. The color shows the amplitude of the oscillation.

The intermediate amplitudes can now be accessed by tuning the resonant frequency of the beam. Because the gate lowers the frequency of the beam, the DC bias must be applied to the final drive amplitude side as diagramed in the modified measurement apparatus in Figure 3.20. One can understand why the bias is applied to the final drive amplitude side by reference to Figure 3.9. With the bias, the frequency of the state plane corresponds to the red curve with inaccessible amplitudes. However, without the bias, the same frequency corresponds to the green curve, allowing us to access those amplitudes for the initial state. Following the procedures used to collect the data of Figures 3.17 and 3.18 above, with a DC bias of 11 mV, the drive switching experiment

was repeated again for a range of driving strengths, again varying the relative phase of the initial and final drive signals.

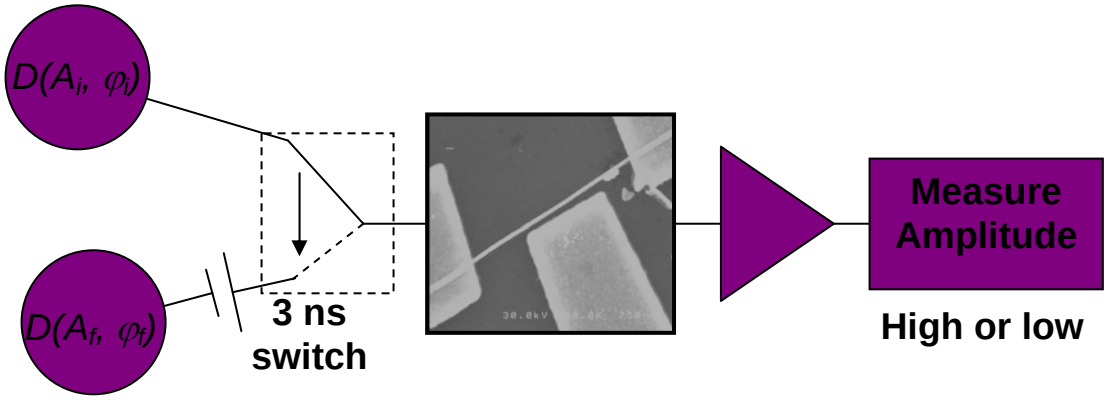

Figure 3.20: Modified measurement setup for measurement of state plane with DC bias of 11 mV added to final drive signal.

Figure 3.21 has plots of the results. To show the basins of attraction clearly, the plot has been recolored in the following way: the state plane was divided up into pixels and the color of each pixel determined by the color of the nearest data point. We have successfully measured the ying-yang shape of the basins of attraction. As the drive strength is increased, the upper state becomes dominant, covering the whole plane. The boundary between the two basins is not well defined due to a number of effects. Noise obviously plays a part in blurring the boundary; its role in switching between stable oscillation modes is addressed in the next section. Additionally, there is no control over any electronic transients that may appear as a result of switching the drive signal. Transient current in the resonator will result in non-resonant forces on the beam that can kick it over the separatrix in a similar manner as noise. It should also be noted that the system we originally set out to study has been modified through the use of gating.

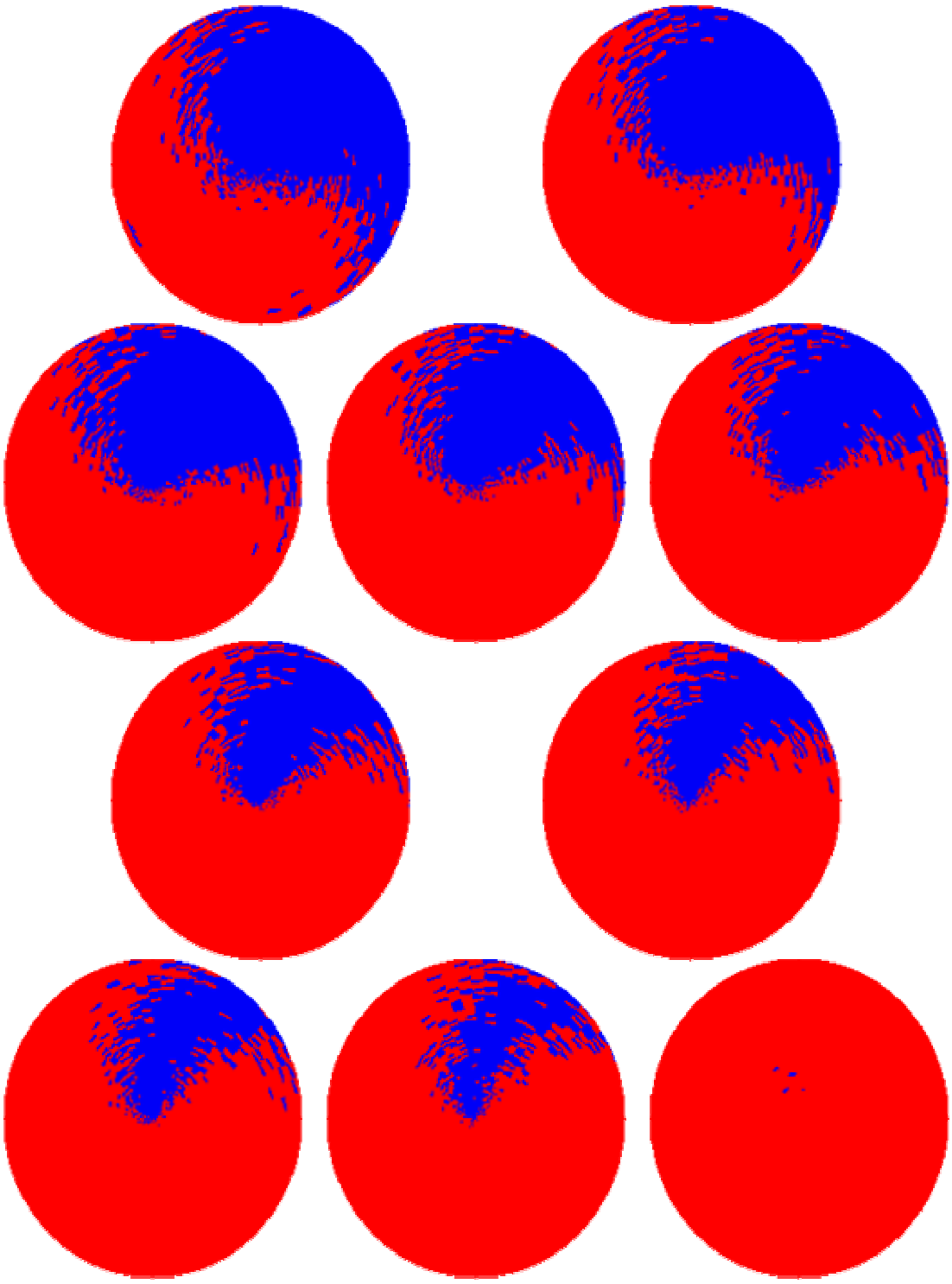

Figure 3.21: Experimental map of platinum nanowire resonator state plane for increasing drive strength from left to right, top to bottom.

3.7 Noise Induced Switching

The effects of noise on physical systems are important to investigate in any experiment. In the non-linear resonator, noise will cause the resonator to switch branches before the tri-valued region has been fully traversed. Figure 3.16, lower left graph, helps to explain this effect in terms of the stability basins. When the resonator is in the upper stable state, within the small area basin, noise can easily "kick" it over the separatrix. Once this boundary is crossed, the sample will settle to the lower stable state. However, the reverse process requires a much larger noise power because the basin boundary is far away from the lower stable state.

We investigated the impact of noise on spontaneous switching at frequencies close to the edge of the hysteretic region in a variety of ways. Initially, the resonator was prepared in the lower state close to the left edge of the tri-valued region. The amplitude of the oscillation is observed until it switches to the upper state and the time is recorded. This process is repeated many times. The wait times are tabulated as a histogram in Figure 3.22.

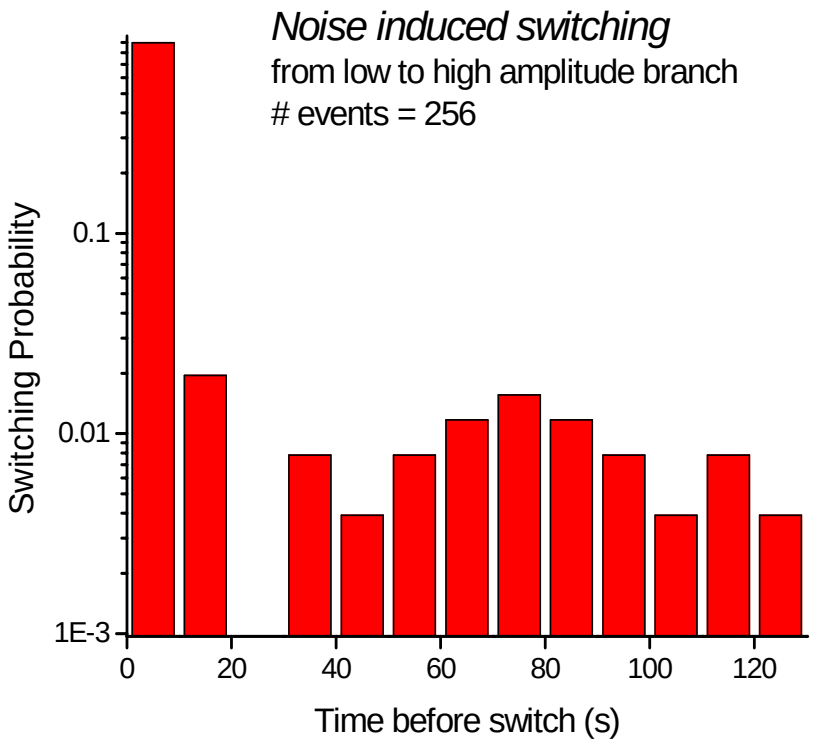

Figure 3.22: Probability of switching event within 10 second intervals. Total number of events is 256.

The wait times are long in the previous experiment, restricting the amount of data we can take. In order to collect a statistically useful amount of data, the experiment was modified by adding a broad-band (white) noise source to the drive line to increase the switching rate. The resonator is again prepared in the lower state at a frequency farther from the left side of the hysteresis, the resonance is monitored until it switches to the upper state, and the time recorded. The procedure is repeated to get enough switching events to perform meaningful statistics. With this data we can plot the probability that the resonator has switched *P(t)* versus time for various noise powers, shown in Figure 3.23. As the noise power is increased, the switching probability for a particular time increases, as one would expect.

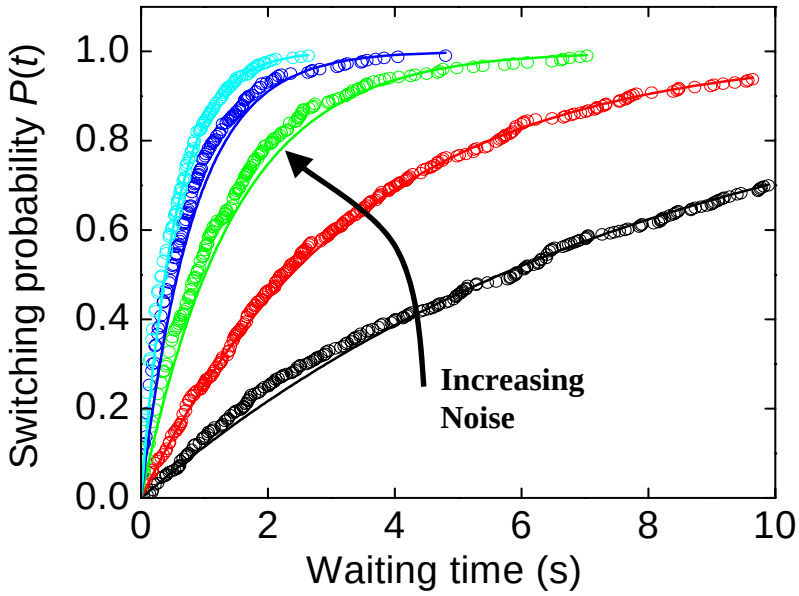

Figure 3.23: Switching probability vs. waiting time for increasing noise power. The solid line is theoretical fit of equation 4. Each curve is 5000 switching events.

The theoretical model, derived by our theorist collaborators Oleg Kogan and Mike Cross, predicts that the probability of switching should follow

$$P(t) = 1 - e^{-t\Gamma}, \quad (4)$$

$$\text{where } \Gamma \propto \delta^{1/2} \exp\left(\frac{-A\delta^{3/2}}{\langle x^2 \rangle}\right),$$

$\langle x^2 \rangle$ is the noise power, A is a factor on the order of unity that depends on the frequency detuning from ω_0, and $\delta = D - D_{NOSE}$. D_{NOSE}, marked in Figure 3.8, is the value of the drive at the left side of the hysteresis in drive amplitude. If the process of switching is considered akin to noise kicking the resonator over an energy barrier, the theory implies a barrier height of $A\delta^{3/2}$. We will seek to verify this prediction.

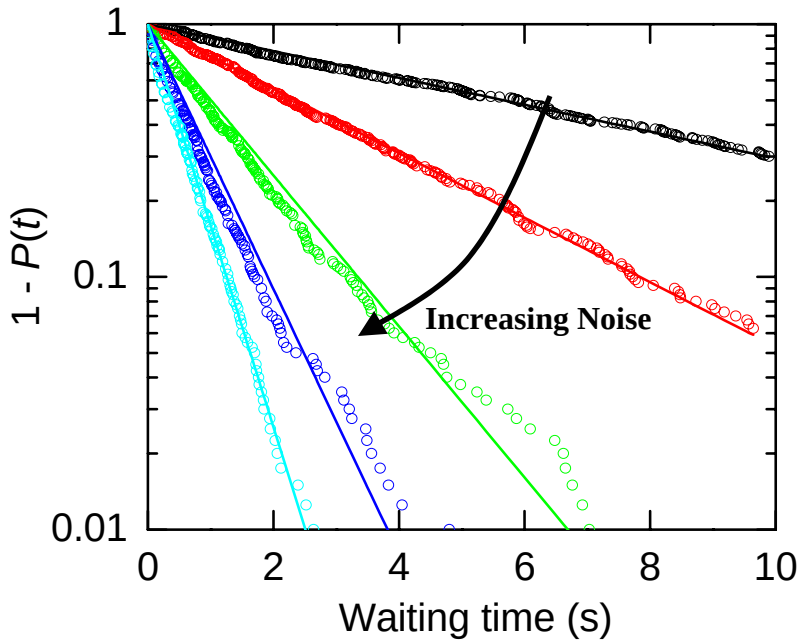

Figure 3.24: Semilog plot of 1-*P(t)* vs. waiting time for increasing noise power.

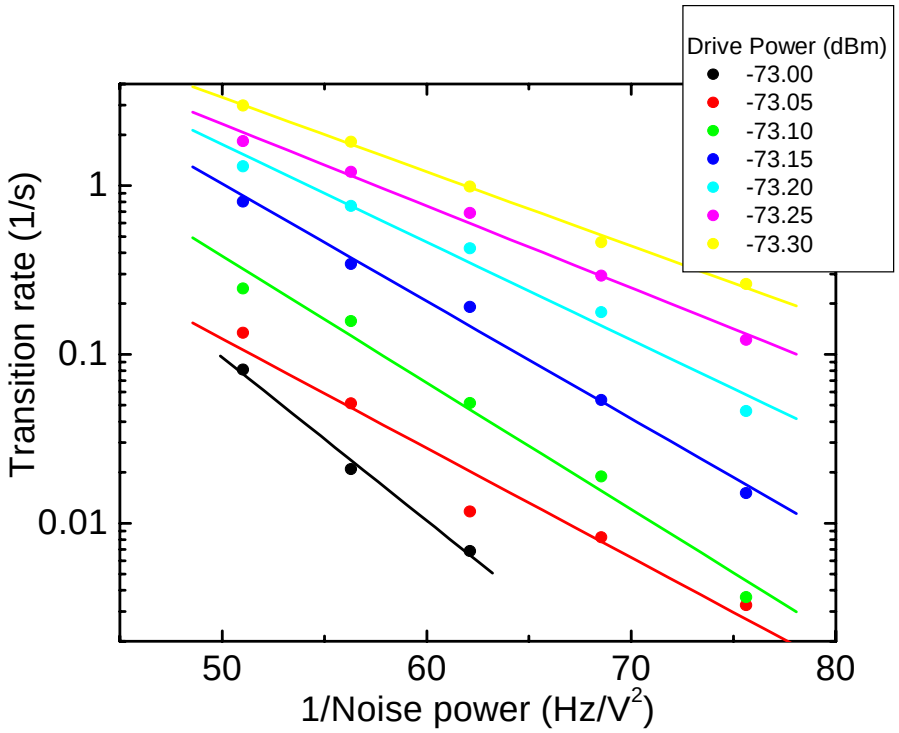

Figure 3.25: Transition rate vs. 1/(noise power) for varying drive power.

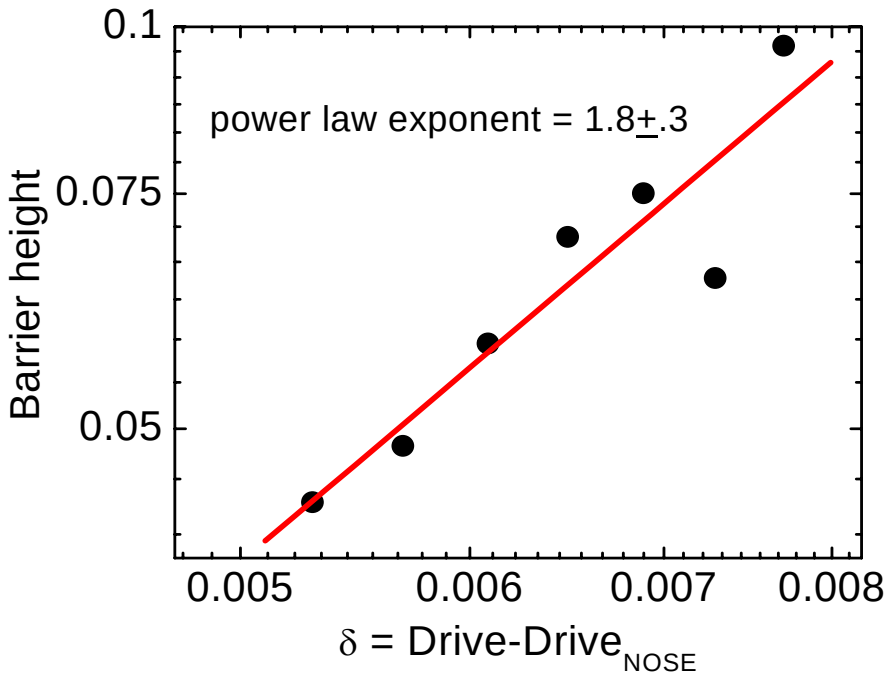

Figure 3.26: Effective energy barrier height vs. driving power. The slope of the line matches with the theory.

By plotting 1-*P(t)* on a semilog axis, as in Figure 3.24, the transition rate Γ for each noise power can be extracted from the slope of the line. The data of Figure 3.24 was collected for a range of drive strengths *D*, extracting Γ for each. For each *D*, the transition rate was plotted against 1/(noise power) again in a semilog plot, shown in Figure 3.25. From the slope of each line in Figure 3.25, the barrier height $A\delta^{3/2}$ can be calculated. Finally, in Figure 3.26, the barrier height is plotted against δ in a semilog plot for the third time. We find that the exponent for δ in the barrier height is 1.8 ± 0.3, in approximate agreement with theory.

3.8 Summary

In this work we have fabricated the first doubly-clamped resonators constructed from “bottom-up” materials, platinum nanowires with diameters about 40 nm and lengths of 1-2 μm. We have developed techniques to detect the resonance modes of high impedance (> 50 Ω), radio frequency devices with magnetomotive techniques and have measured the resonance characteristics of such devices. Our devices exhibit a quality factor much larger than “top-down” fabricated resonators of a comparable size, probably because of reduced surface dissipation.

Non-linear effects arise at relatively low driving amplitude. We have measured the basins of attraction of the beam, verifying that the Duffing oscillator is a good model for the non-linear effects observed. Switching between stable resonance amplitudes is observed and the influence of noise on switching was tested. The results follow the theoretical model for the switching rates well.

References

[1] M. D. LaHaye, O. Buu, B. Camarota et al., "Approaching the quantum limit of a nanomechanical resonator," *Science* **304** (5667), 74-77 (2004).

[2] A. N. Cleland and M. L. Roukes, "Fabrication of high-frequency nanometer-scale mechanical resonators from bulk Si crystals," *Applied Physics Letters* **69** (18), 2653-2655 (1996).

[3] Y. T. Yang, K. L. Ekinci, X. M. H. Huang et al., "Monocrystalline silicon carbide nanoelectromechanical systems," *Applied Physics Letters* **78** (2), 162-164 (2001).

[4] D. A. Harrington, P. Mohanty, and M. L. Roukes, "Energy dissipation in suspended micromechanical resonators at low temperatures," *Physica B* **284**, 2145-2146 (2000).

[5] A. N. Cleland, M. Pophristic, and I. Ferguson, "Single-crystal aluminum nitride nanomechanical resonators," *Applied Physics Letters* **79** (13), 2070-2072 (2001).

[6] S. Sapmaz, Y. M. Blanter, L. Gurevich et al., "Carbon nanotubes as nanoelectromechanical systems," *Physical Review. B, Condensed Matter and Materials Physics* **67** (23), art.no.-235414 (2003).

[7] Y. Huang, X. F. Duan, Y. Cui et al., "Logic gates and computation from assembled nanowire building blocks," *Science* **294** (5545), 1313-1317 (2001).

[8] C. R. Martin, "Nanomaterials - a membrane-based synthetic approach," *Science* **266** (5193), 1961-1966 (1994).

[9] S. Timoshenko, D. H. Young, and W. Weaver, *Vibration problems in engineering*, 4th ed. (Wiley, New York,, 1974), pp.xiii, 521.

[10] *CRC handbook of chemistry and physics*. (CRC Press, Cleveland, Ohio, 1977), p.v.

[11] H. Krommer, A. Erbe, A. Tilke et al., "Nanomechanical resonators operating as charge detectors in the nonlinear regime," *Europhysics Letters* **50** (1), 101-106 (2000).

[12] A. N. Cleland and M. L. Roukes, "External control of dissipation in a nanometer-scale radiofrequency mechanical resonator," *Sensors and Actuators. A, Physical* **72** (3), 256-261 (1999).

[13] D. W. Carr, S. Evoy, L. Sekaric et al., "Measurement of mechanical resonance and losses in nanometer scale silicon wires," *Applied Physics Letters* **75** (7), 920-922 (1999).

[14] H. W. Ch. Postma, I. Kozinsky, A. Husain et al., "Dynamic range of nanotube and nanowire NEMS resonators," Unpublished (2004).

[15] L. D. Landau and E. M. Lifshits, *Mechanics*, 3rd rev. English , repr. with corrections. ed. (Pergamon Press, Oxford ; New York, 1989), p.170.

[16] A. H. Nayfeh and D. T. Mook, *Nonlinear oscillations*. (Wiley, New York, 1979), p.704.

Chapter 4

Carbon nanotube

fabrication and devices

4.1 History and properties of carbon nanotubes

Carbon nanotubes (CNT's) were first discovered in 1991 by Ijima[1], who found a nested form of CNT know as a multi-walled nanotube (MWNT). Soon after, in 1993, Ijima and Ichihashi[2] as well as Bethune[3] et al. discovered that under the proper conditions one can produce single-walled nanotubes (SWNT's), which can have dimensions as small as .4 nm.[4] Since then, CNT's have been an extremely active area of scientific research. Mechanically, CNT's have an unprecedented degree of tensile strength and reversible deformability. Electrically, this material can exhibit or lack a band gap. Due to these interesting properties, nanotubes have been integrated in devices such as transistors[5], room-temperature single-electron transistors (SET's)[6], atomic force microscope tips[7] and other mechanical structures.[8] There have been uses proposed such as nearly frictionless nano-bearings[9], mechanical memory arrays[10], and more fancifully, a space elevator.

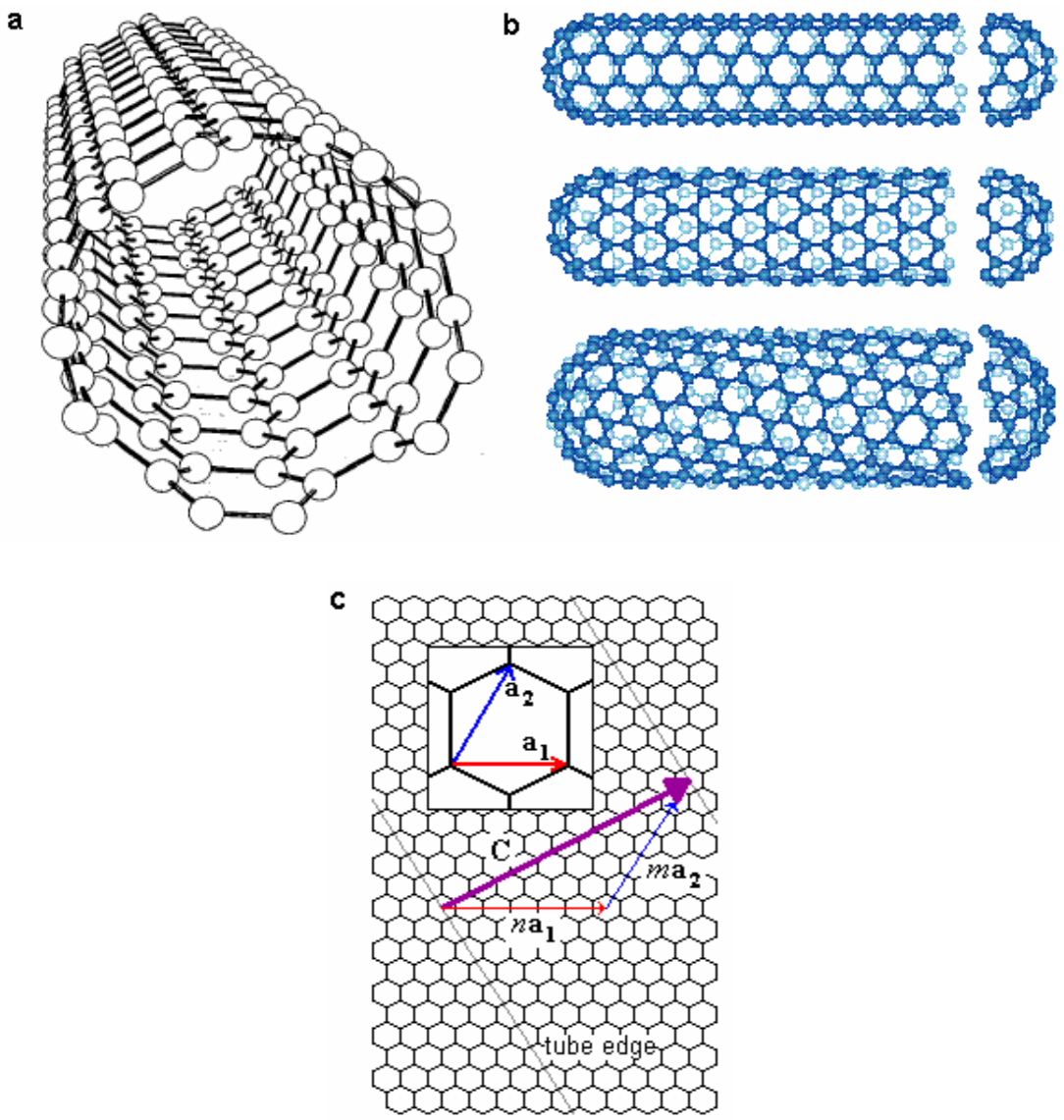

Figure 4.1: Basics of carbon nanotube structure. **a**, hexagonal, sp^2-bonded carbon rings comprise the length of the nanotube. **b**, single-walled nanotubes of various chiralities with endcaps. **c**, vector definition of nanotube chirality (inset: basis vectors $\mathbf{a_1}$ and $\mathbf{a_2}$).

The atomic structure of SWNT's can be understood by beginning with graphite's atomic structure of repeating units of hexagonal rings, which has a sp^2 bonding structure. A SWNT is formed by rolling up a graphene sheet into a tube, as shown in Figure 4.1a. The ends are capped with hemispherical carbon bonded in hexagonal and pentagonal

rings similar to a soccer ball (Figure 4.1b). Another way to think of a SWNT is as an extended fullerene, of which the "bucky ball" (C_{60}) is the most famous.[11] As mentioned above, CNT's come in two "flavors": single-walled nanotubes and multi-walled nanotubes, the latter of which are comprised of multiple nested SWNT's. SWNT's are typically several nanometers in diameter and have been synthesized in lengths up to several hundred microns.[12]

Nanotubes have a variety of interesting and useful properties. In the mechanical regime, they are predicted to have a very large Young's modulus, approximately 1 TPa,[13] greater than that of steel. The large Young's modulus makes CNT's highly desirable for nano-scale resonators, as explained later in this chapter. Carbon nanotubes also have the capability to buckle and restore their shape and are stable to 2800°C in vacuum and 750°C in air.[14] Their robustness and small size make CNT's a nearly ideal source for field emission of electrons[15], an effect that will be described in more detail later.

The particular direction and length of the rolling vector, known as the helicity or chirality of the nanotube, has a profound impact on the electrical properties of a SWNT. The chirality of the SWNT is calculated by finding the vector **C** that is required to traverse the circumference of the tube. The vector can be expressed as a linear combination of the two basis vectors $\mathbf{a_1}$ and $\mathbf{a_2}$ of the hexagonal lattice of the graphene sheet as shown in Figure 4.1c. The chirality is represented as a pair integers (n, m) corresponding to the coefficients of the basis vectors. The specific chirality of a tube determines the electrical properties. The band structure of a carbon nanotube is related to that of a graphene sheet. For graphene, at the high symmetry points of the Brillouin zone, the conduction band touches the valence band, which results in a metallic

conductor. When the sheet is rolled up to form a SWNT, a quantization condition is introduced in the k-vector corresponding to the chiral vector. This requirement cuts sections of the graphene band diagram. These sections are the band structure of the SWNT. If one of the cuts passes through a high symmetry point where the bands touch, the nanotube has metallic conduction properties. Otherwise, it is a semiconductor. This condition can be expressed in terms of the basis vectors: if n-m is a multiple of three, then the tube is metallic, otherwise it has a band gap.

4.2 Fabrication Issues with CNT's

Integrating carbon nanotubes with top-down fabrication techniques entails particular challenges. In the first part of this section, we describe several CNT fabrication techniques and the difficulty in controlling chirality, length and tube orientation. In the next part we present some of our experimental studies on the damage of nanotubes by several standard fabrication techniques. These techniques were chosen because of their applicability to the goal of fabricating a resonator from a single carbon nanotube. We required that the device have low electrical resistance and that the nanotube be damaged as little as possible. Physical damage to the nanotube would lower the quality factor of the device.

4.2.1 Nanotube synthesis

There are several methods to fabricate CNT's that have been developed by researchers in the 1990's. Early methods include arc-discharge and laser ablation. In an arc-discharge process, an electrical arc is produced in a chamber between graphite electrodes, which supply the carbon for the nanotubes.[16] A small amount of transition-metal catalyst impurity is included in the graphite electrodes. The arc vaporizes the graphite, which deposits on the walls of the chamber in a variety of forms resembling soot. Certain regions of the deposit contain a high proportion of CNT's. The laser ablation method is similar to arc discharge, except that the graphite is vaporized by a laser pulse rather than an arc-discharge.[12] Both of these methods produce a high percentage of amorphous carbon, requiring the soot to be purified to yield high quality material. The purification process involves acids that may damage tubes.

In order to build devices, researchers made suspensions of the nanotubes by ultrasonic agitation in organic solvents. The suspension is then dropped onto a chip where the nanotubes, or bundles of nanotubes, stick to the surface by van der Walls forces. One of our goals was to conduct experiments on isolated SWNT's. It is very difficult to achieve a single SWNT with the suspension method. Additionally, we were able to make only poor electrical contacts to these tubes, possibly due to organic solvent adsorbed to the tubes.

More recently, a more subtle method has been developed for growing carbon nanotubes on a substrate by a chemical vapor deposition (CVD) method.[17] In this method, the substrate on which the CNT's are to be grown is seeded with catalytic material such as Fe or Ni. The substrate is placed into a high temperature tube furnace and a gaseous hydrocarbon such as methane or ethylene is flowed over the substrate. At

the high temperature, the hydrocarbon disassociates and the carbon dissolves in the metal catalyst, which becomes supersaturated with carbon. The carbon precipitates out of the particle as a carbon nanotube.[12] The CVD method is highly versatile. The catalyst can be patterned to create local regions from which CNT's grow. Varying the catalyst density can control the density of tubes, to the extreme case of dense "forests" of aligned nanotubes[18], under the right conditions. The selection of hydrocarbon and temperature allows one to grow either MWNT's or SWNT's. There are many variations on this technique. Patterned catalytic growth gives one some influence over the location and length of the nanotubes, though the chirality and orientation are still almost impossible to control.

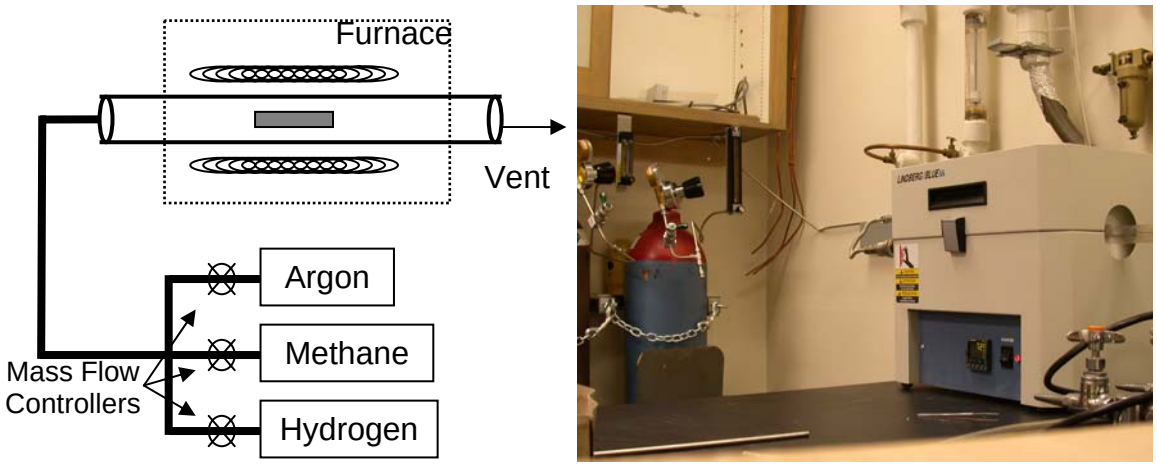

Figure 4.2: Left—schematic of tube nanotube synthesis system. Right—photograph of actual system with tube furnace and gas cylinders visible.

We found that the CVD synthesized tubes are more suitable than the arc-discharge or laser-ablation CNT's for fabricating the nanotube resonator. The nanotubes are of higher quality and it is easier to control the location of the nanotubes. Also, the

CVD method ensures that isolated tubes on the substrate are likely to truly be a single tube, not a small bundle of tubes. Finally, lower resistance electrical contacts were found in CVD synthesized tubes because they are cleaner with respect to solvents and amorphous carbon deposits.

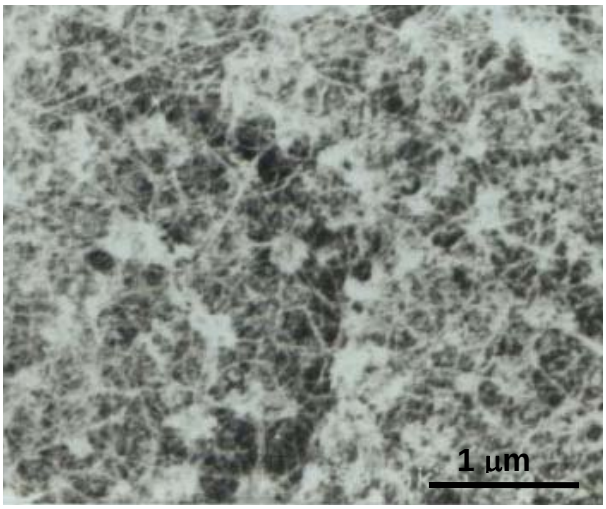

Figure 4.3: Film of SWNT's grown in CVD system of Figure 4.2.

We have set up a CVD tube furnace here at Caltech and grown carbon nanotubes using the patterned catalyst method. Figure 4.2, left, has a schematic of the CVD system while a photograph of the setup is shown on the right. The carbon feed stock is methane. Argon (Ar) is used as an inert gas when cooling or heating the system. Hydrogen (H_2) is added during heating to chemically reduce the catalyst and during CNT growth to reduce the amount of amorphous carbon that is produced in this process. In a typical process the tube furnace is heated to 900°C under Ar and H_2 flow at 500 cm^3/min and 2500 cm^3/min, respectively, after loading a sample that has been seeded with Fe catalyst. Once the furnace temperature has stabilized, the flow is switched to methane and hydrogen flow at

1500 cm^3/min each to grow the carbon nanotubes. After 5-15 minutes, the gas flow is switched back to argon flow at 1000 cm^3/min and the furnace is allowed to cool to room temperature. The growth time determines, to some degree, the length of the tubes synthesized. Figure 4.3 shows an SEM picture of a CNT film grown in this furnace. The process described above produces SWNT's; to grow MWNT's, replace the methane by acetylene and reduce the growth temperature to 800°C.

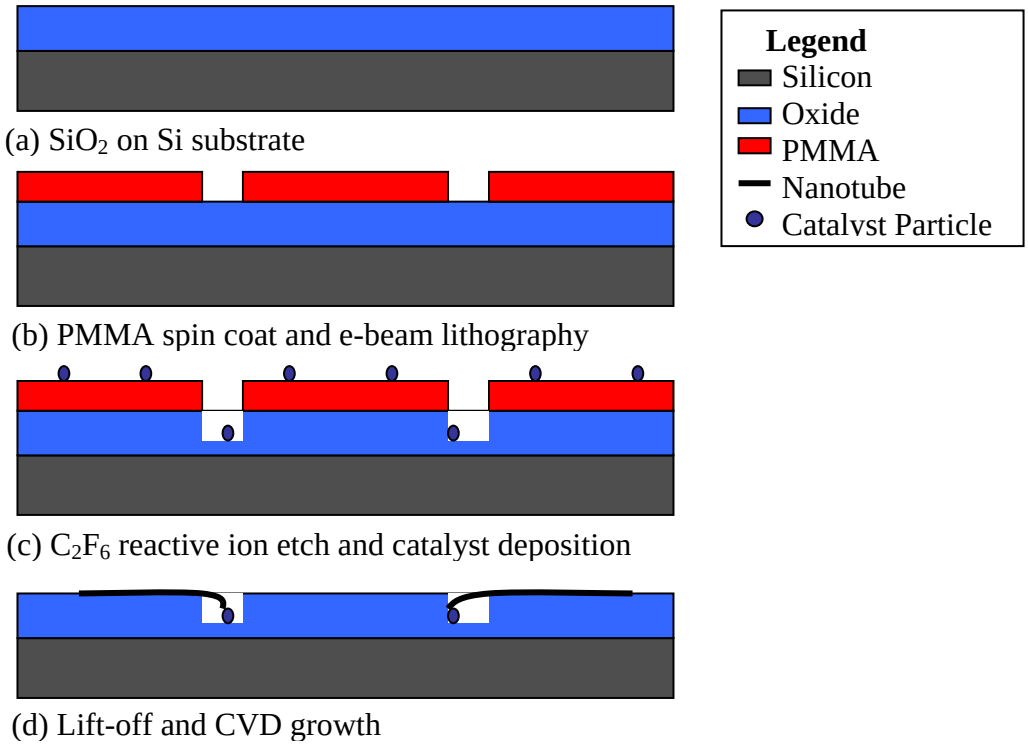

Figure 4.4: Patterned catalyst and nanotube growth procedure.

To conduct experiments on isolated SWNT's we developed a process to place small, isolated areas of catalyst on the surface. Figure 4.4 outlines the procedure, which begins with a silicon chip with thermally grown oxide on the surface. Electron beam lithography is performed on a layer of PMMA to define the areas where the catalyst will

be placed. A short reactive ion etch (RIE) is performed to create sunken sites. The chip is dipped into a solution of 1 mM $Fe(NO_3)_3 \bullet 9H_2O$ in isopropanol and then immediately dipped into hexane. The iron nitrate precipitates out in the hexane and deposits on the surface. An alternative method to deposit the catalyst is to evaporate a very thin film (less than 1 nm) of Fe and/or Ni. Next, the PMMA is stripped off with acetone, leaving the Fe catalyst in the indentations in the oxide. Finally, the chip is place into the CVD system to grow CNT's. Figure 4.5 shows tubes grown in this fashion. All the tubes in this AFM image originate in a hole in the surface where the catalyst was deposited.

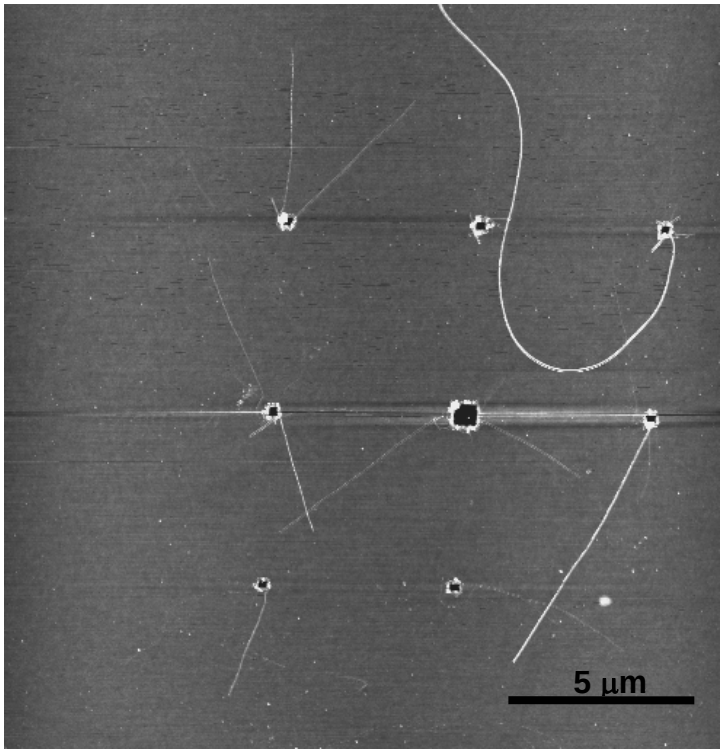

Figure 4.5: AFM image of nanotubes grown by patterned catalyst and CVD synthesis. All the nanotubes originate from catalyst particles in the holes.

Due to the high temperature process required to synthesize CNT's, it is challenging to integrate them with top-down fabricated structures. In order to place electrical contacts by electron beam lithography, for example, onto nanotubes, there must be some marks on the surface to align to. However, gold pads deposited before the synthesis will melt and deform in the tube furnace, an example of which is shown in Figure 4.6. Some methods around this particular problem are to deposit alignment marks after the furnace step or to use materials for alignment marks that will survive the high temperature growth. In particular, an iron alloy (trade name Kanthal), stable to 2000°C has been previously reported to be compatible with nanotube growth.[19]

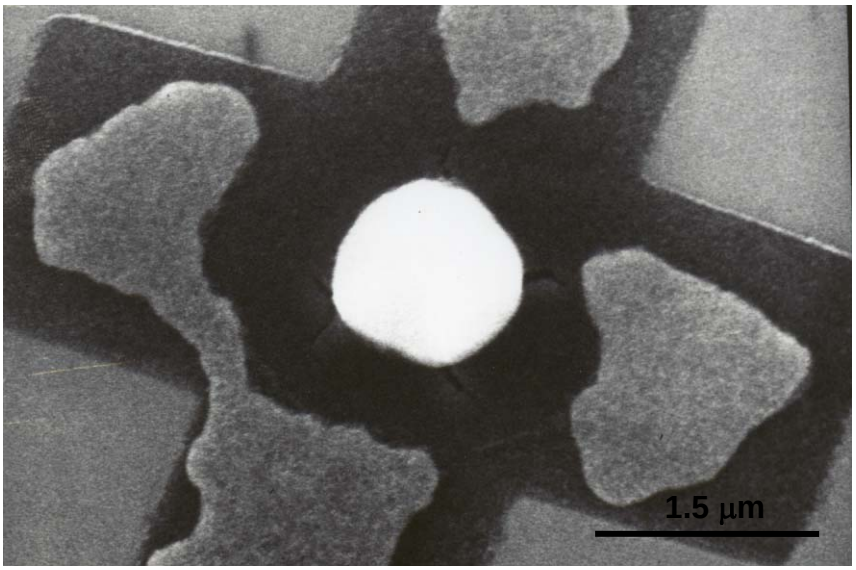

Figure 4.6: Gold alignment mark after CVD nanotube sythesis. The underlying chrome sticking layer shows the original shape of the alignment mark.

The approach we used was to fabricate alignment marks by sputtering of Kanthal. The nanotubes are imaged and mapped using atomic force microscopy (AFM) after synthesis. Electron beam lithography was used again to define the electrical leads.

Evaporation of Cr/Au and lift off complete the process of making electrical contacts to the carbon nanotubes. Stray conduction is minimized by the use of high quality thermally grown SiO_2 on Si wafers.

4.2.2 Fabrication effects on CNT's

Post-synthesis processing can pose a significant threat to the structural integrity or even survival of nanotubes. Damage from microfabrication techniques can reduce the conductivity and degrade the mechanical properties. As an example, Figure 4.7 shows an SEM picture of a carbon nanotube contacted by two metal pads and then subsequently subjected to a reactive ion etch (RIE) process, a common fabrication tool. The tube has been completely etched away where exposed.

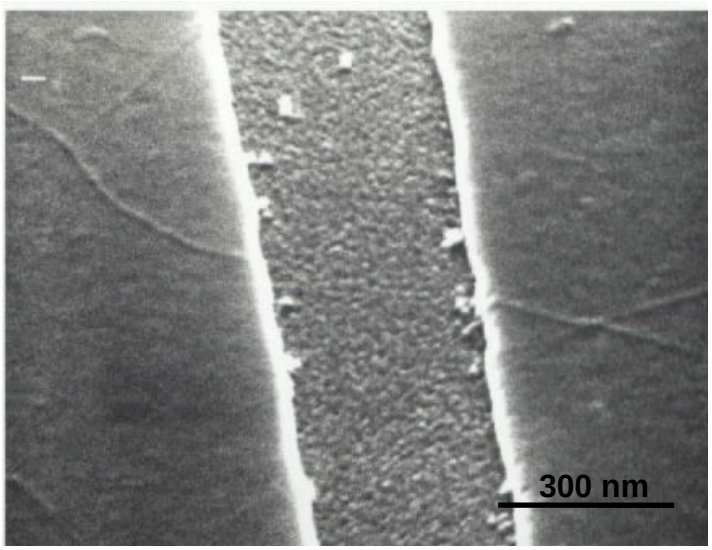

Figure 4.7: SEM picture of destroyed carbon nanotube after RIE etching.

In an attempt to characterize the damage done to CNT's by various fabrication techniques, the conductivity of the tube is taken as a proxy for the damage done by various microprocessing techniques. We made electrical contact, following the procedure outlined in previous chapters, to a collection of SWNT's fabricated using the CVD technique described in the previous section and measured the resistance of each. Next, the samples were subjected to common processing and etching techniques. At intervals, the effective resistances of the tubes were measured. An increase in resistance would indicate some form of damage to the tube.

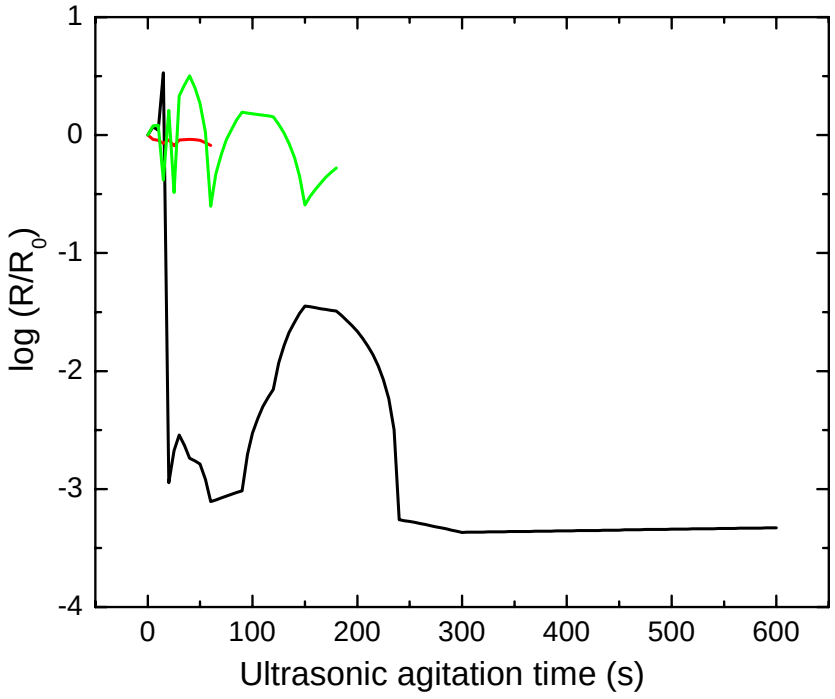

Figure 4.8: Relative change from original resistance R_0 vs. ultrasonic agitation time for three carbon nanotubes.

Ultrasonic agitation is often used to aid lift-off or as a helpful cleaning process in microfabrication. However, since the process involves the transmission of energy to the surface of the chip, it has the potential to damage small structures on the surface. To test

the effect of this process, a sample containing four SWNT's was prepared. The sample was agitated in acetone for 5 sec intervals, rinsed with isopropyl alcohol (IPA) and blown dry with nitrogen. The resistance of each tube was tested at each interval. Figure 4.8 plots the relative change in resistance vs. ultrasonic agitation time. One of the nanotubes did not survive any ultrasonic agitation and is not plotted here. Except for eventually losing contact or breaking, ultrasonic agitation has a relatively benign effect on nanotubes. A normal agitation time for fabrication is about 15 s, so we would expect to be able to use this process on nanotubes.

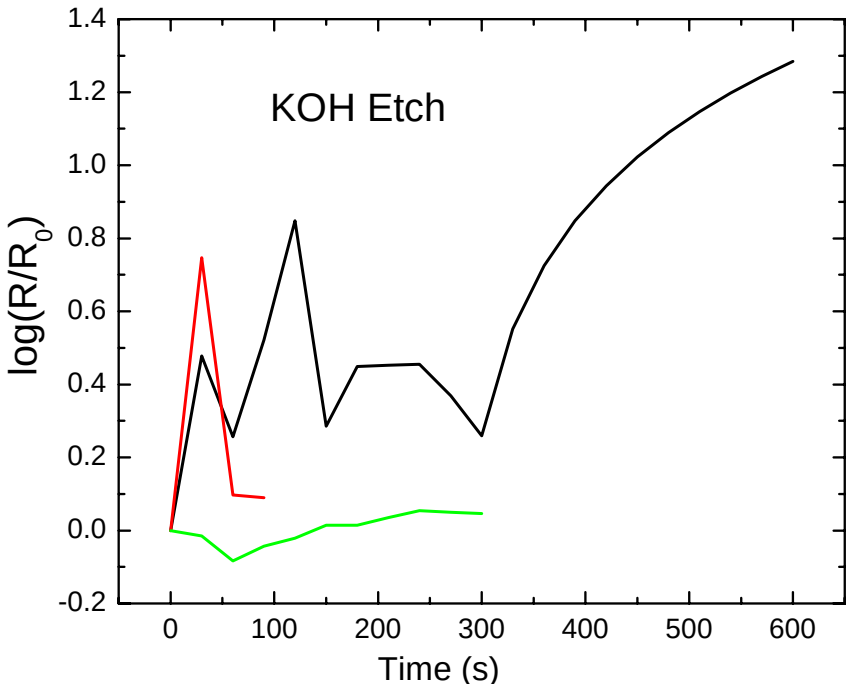

Figure 4.9: Resistance change vs. KOH Etch time for three carbon nanotubes.

The process described in the next section for creating a carbon nanotube resonator requires a sacrifical layer of sputtered Si to be etched away from under the nanotube, once it has been clamped. We tested three processes, all of which etch silicon, to

determine which would have the least impact on the nanotubes. Each will be described briefly and the data presented.

A solution of potassium hydroxide (KOH) is an anisotropic etch that preferentially exposes the (111) planes of single crystal Si. For sputtered Si, a 1 min etch removes 100 nm. A sample of four electrically contacted nanotubes was fabricated. The sample was dipped into 1M KOH solution for 30 s intervals, rinsed in deionized water and then IPA, and finally blown dry with nitrogen. The resistance of each tube was measured at each interval. The results are plotted in Figure 4.9. One of the four tubes did not survive any exposure to the etch. Etching in KOH clearly increases the resistance of tubes, which we interpret as damage.

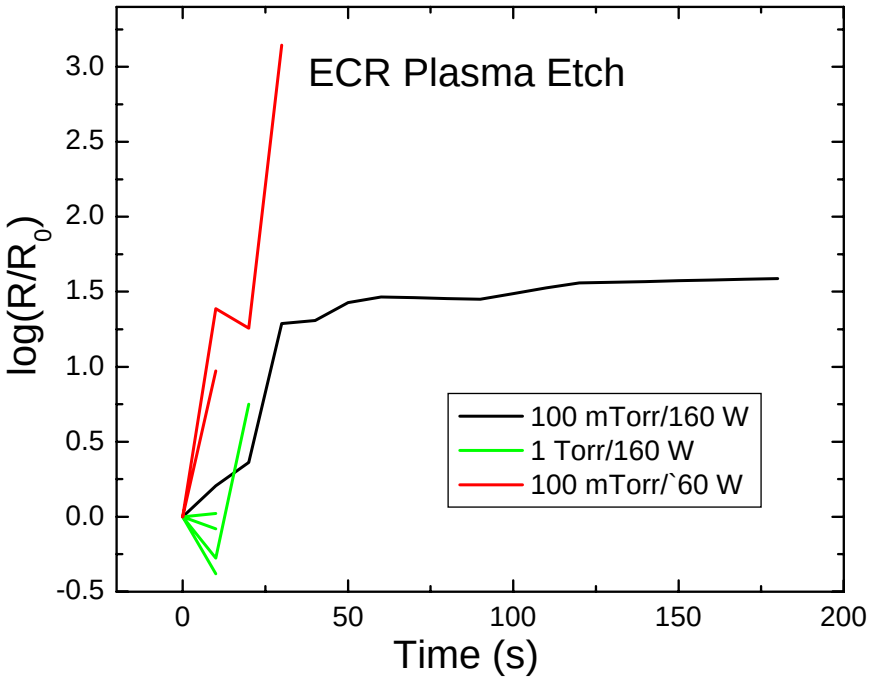

Figure 4.10: Resistance change vs. ECR etch time for various etch conditions.

Electron cyclotron resonance (ECR) etching is a type of low-pressure dry etch process which generates a plasma of molecules and ions that react with the material to be etched. The etch gas was NF_3. To etch 100 nm of Si, 20 s is required in this process. Three different conditions of pressure and input power were used on a total of eleven nanotubes for etch intervals of 10 s. The results are plotted in Figure 4.10. Some tubes did not survive at all and only three survived longer than 20 s. Plasma etch process are undoubtedly harmful to the integrity of carbon nanotubes.

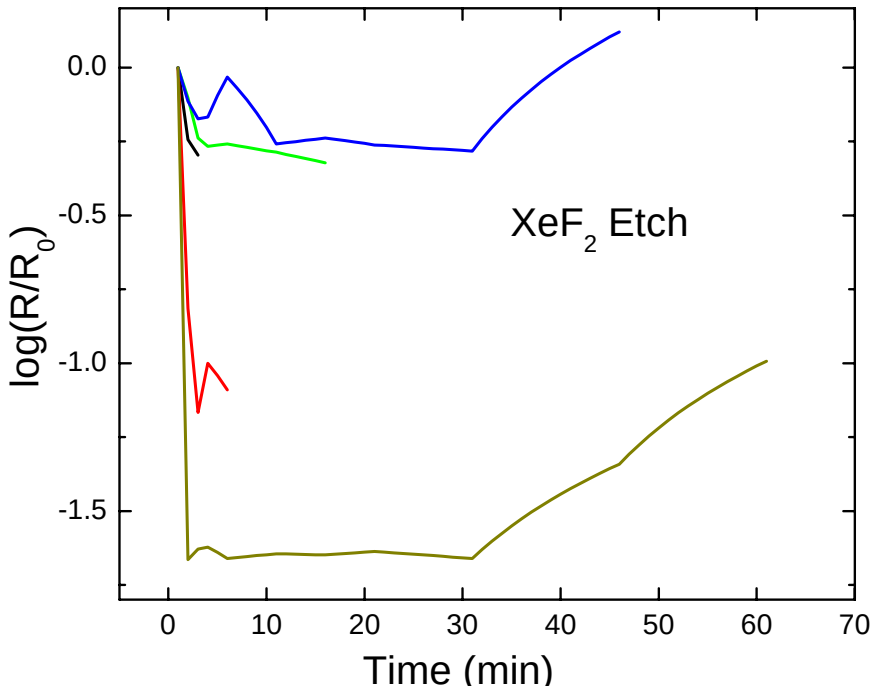

Figure 4.11: Resistance change vs. XeF_2 etch time for five carbon nanotubes.

The final etch technique tested was dry etching with XeF_2 in a low pressure chamber. This etch does not require a plasma, only heating to 80°C. The fluoride reacts with the Si, creating the volatile SiF_4, which is pumped away. This process is considerably slower, requiring 5-7 min to remove 100 nm of Si. Four of five tubes

survived the first interval of 5 min, shown in Figure 4.11. Interestingly, the conductivity of the tubes increases. This may be caused by adsorption of fluorine on the surface of the tubes. It has been previously reported that gas adsorption can influence the conduction properties of carbon nanotubes.[20] It is clear that dry etching with XeF_2 is the least damaging of the Si etch processes tested. In the next section, we make use of these results to design and carry out a process to create doubly-clamped carbon nanotube resonators.

4.3 Doubly-clamped carbon nanotube beam

Carbon nanotubes have many properties that lend them toward being used as ultra sensitive nanomechanical resonators. They have a large Young's modulus and a low density which is important for making high frequency, ultra-sensitive devices. In addition, because they are extremely resilient and can conduct charge, CNT's are an ideal material from which to fabricate electromechanical devices. We developed processes to fabricate and measure a single carbon nanotube resonator.

The CVD method was chosen for synthesizing nanotubes to fabricate into resonators because it offers cleaner, defect free material with low contact resistance. Figure 4.12 shows the fabrication process. A thermally grown SiO_2 on Si chip is prepared with a sputtered Si layer and Kanthal alignment marks. Carbon nanotubes are grown by the CVD method, and then mapped with an AFM. E-beam lithography, evaporation and lift-off create electrical contacts to candidate nanotubes. To complete the structure, the sample is etched in XeF_2, etching the sputtered Si layer and leaving a

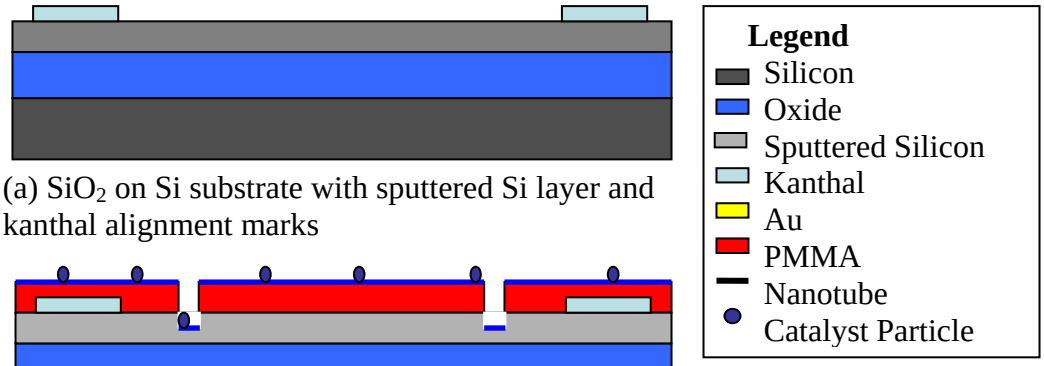

(a) SiO_2 on Si substrate with sputtered Si layer and kanthal alignment marks

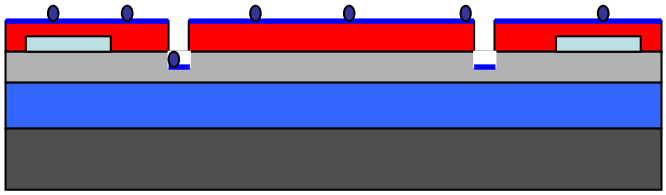

(b) E-beam lithography, RIE and catalyst

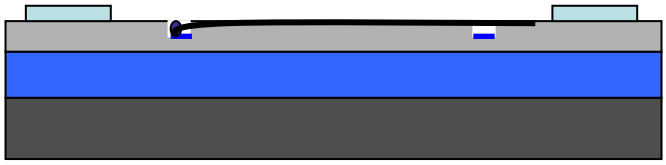

(c) Lift-off and CVD synthesis of nanotubes

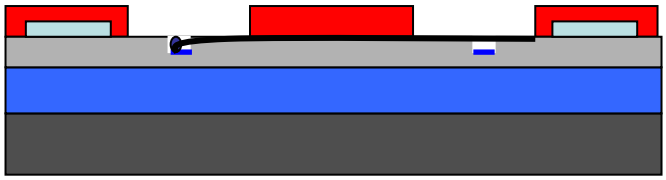

(d) E-beam lithography to define contacts

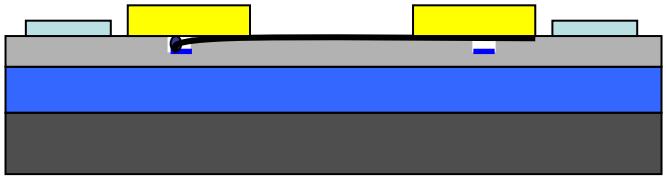

(e) Au evaporation and lift-off

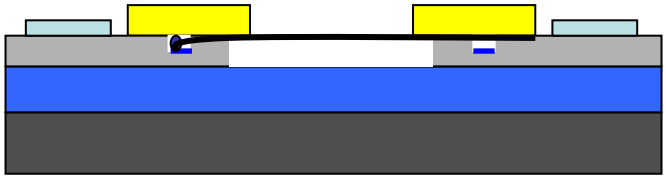

(f) XeF2 etch to undercut nanotube

Figure 4.12: Fabrication process to synthesize SWNT's and integrate them into doubly-clamped mechanical resonators.

freely suspended doubly-clamped carbon nanotube. Figure 4.13 shows an SEM image of a fabricated device.

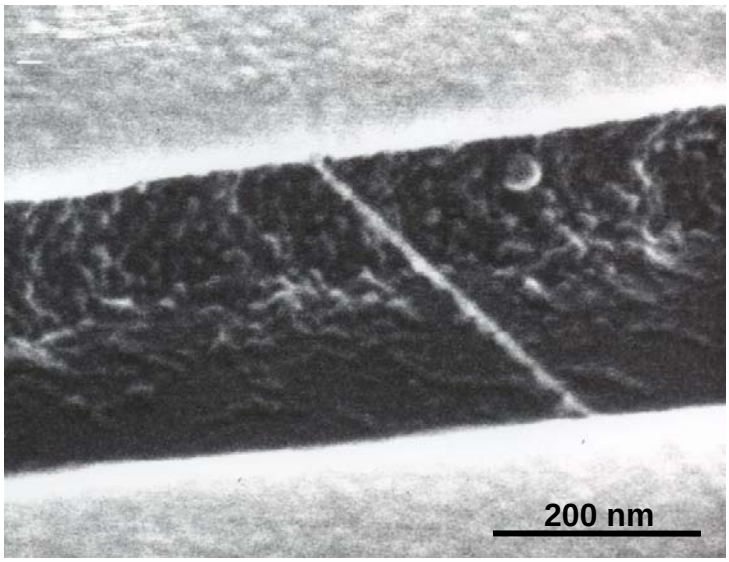

Figure 4.13: SEM image of doubly-clamped carbon nanotube beam.

We fabricated doubly-clamped carbon nanotube structures for measurement by the magnetomotive method described in Section 3.3. To accomplish such an experiment, the total input impedance at the device must be less than about 5 kΩ. However, single walled nanotubes have only a few quantum channels to conduct electrons. Each quantum channel has conductance $2e^2/h$, or about 13 kΩ. In the absence of any other scattering or contact resistance, two quantum channels have a resistance of 6.5 kΩ out of range to directly drive from the RF source. Even with the 50 Ω terminations, as shown in Figure 3.4, the output signal would be divided down to lower power than the noise introduced by the output amplifier. One method to measure a SWNT magnetomotively would be to design a matching circuit composed of capacitive and inductive elements. The matching circuit is impractical for this purpose, however. A single stage matching circuit has a

very narrow pass band and the frequency of the device, though it can be calculated approximately, is not known *a priori*. Another method would be to fabricate two CNT resonators in an electrical bridge configuration, with a null voltage at the common terminal. Then a change in impedance of one or other branches of the bridge will result in a non-zero voltage at the common terminal. Yet another possible method is to use the nanotube as both a resonator and a single-electron-transistor (SET) for detection.[21]

We did not achieve measurements on this device due to the difficult fabrication process and very small yield of low resistance samples. This project is ongoing with collaborators making efforts to fabricate and measure both SWNT and MWNT nanotube resonators magnetomotively.

4.4 Field-emission with integrated grid

We collaborated with the Submillimeter Wave Advanced Technology (SWAT) group at Jet Propulsion Laboratory (JPL) to fabricate electron field emission sources for miniature mass spectrometers and the nanoklystron. JPL has a program to develop miniature mass spectrometers for chemical analysis in space exploration and environmental monitoring for astronaut safety. A key component of a miniature mass spectrometer is an electron beam to ionize the molecules being analyzed. The nanoklystron is an effort under way at JPL to create a terahertz radiation source, which involves an electron resonance chamber at the frequency of interest.[22] The nanoklystron is designed for space applications, specifically for elemental analysis. A key requirement of this project is a nanoscale field emission source that can be integrated into the package.

The specifications for the source are particularly rigorous requiring a current density of 1 kA/cm^2 and a low operating voltage

Carbon nanotubes, in addition to its other outstanding properties, are one of the best materials for generating free electrons through field emission. Table 1 compares the electric field strength required for emission for a variety of materials—CNT's being the lowest.[15] In addition, CNT's have other properties suitable for field emission. Tubes are extremely stable, and therefore have the potential for long life as field emitters. The physical structure of CNT's also brings benefits. When a voltage is applied to a metallic object, electric field lines concentrate at surfaces with a very small radius of curvature. SWNT's can have a radius as small as .7 nm, yielding very high field amplification at the tips.

Material	Threshold electric field (V/μm)
Mo tips	50-100
Si tips	50-100
p-type semiconducting diamond	130
Undoped, defective CVD diamond	30-120
Amorphous diamond	20-40
Cs-coated diamond	20-30
Graphite powder(<1mm size)	17
Nanostructured diamond	3-5
Carbon nanotubes	1-3

Table 4.1: Field emission threshold for various materials.[23]

Single-walled carbon nanotube films grown with the CVD system described in Section 4.2.1 were fabricated on degenerately doped silicon wafers in order to make

electrical contact to the tubes. This sample was tested for field emission along with CVD tubes synthesized by Hoenk at JPL and by Baohe at Brown University. The JPL nanotubes were disordered MWNT's while the samples from Brown were ordered MWNT's grown in an anodized alumina template. The samples were tested in an ultra-high vacuum (UHV) system with pressure of 1 x 10^{-10} torr. The anode was spaced 1 μm away from the sample chip surface. Figure 4.14 shows the current emission density as a function of the electric field. The Caltech sample has the highest threshold electric field and emits a lower current density than the other samples. It is apparent that our nanotubes are not as efficient as field emitters as others. This may have been because of a lower density of emitters on the surface, or poor contact between the substrate and nanotubes. In addition, arcing within the chamber damaged our sample as shown in the SEM image of Figure 4.15.

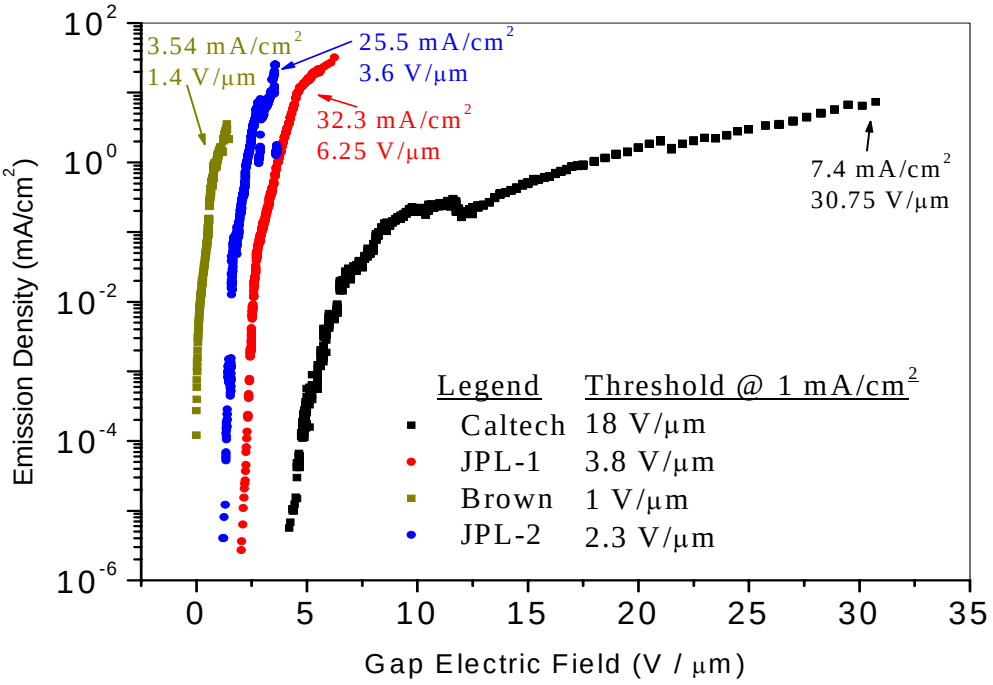

Figure 4.14: Emission current density vs. electric field for nanotubes fabricated by JPL, Brown University and Caltech with the threshold voltage tabulated for each sample.

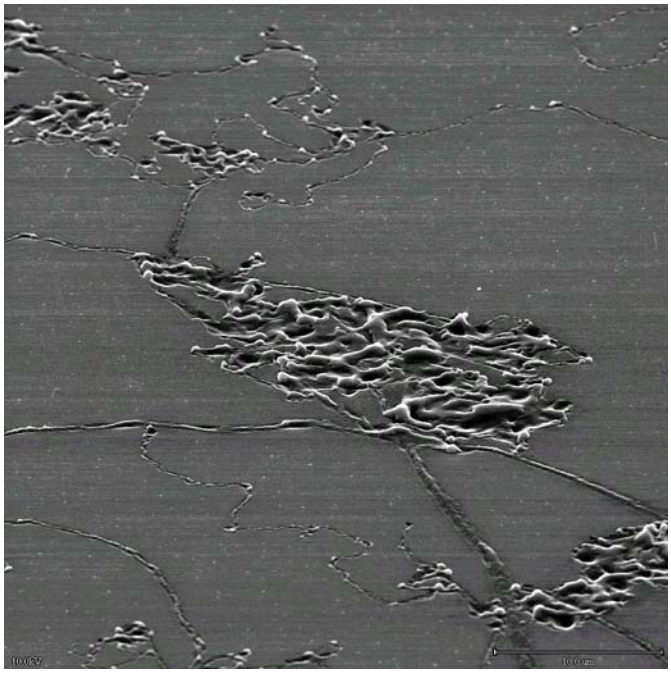

Figure 4.15: SEM image of pitted surface of SWNT field emission sample from arcing within test chamber.

Because of the cost of extra weight in space applications, a critical requirement is that the device operates at low voltage. To minimize the voltage, the anode must be as close to the field emission source as possible. We have designed and a method of integrating a grid onto CVD grown carbon nanotubes and fabricated such structures. Though our tubes don't seem to be the optimal for the nanoklystron, we used them for the integrated grid structure for the purposes of proof of concept.

Figure 4.16 shows the process steps for making the integrated grid structure. The process begins with a disordered mat of SWNT's synthesized on a degenerately n-doped silicon wafer by the process described above. The degenerate Si allows us to have electrical contact to the nanotube from the backside of the chip. Next, the nanotubes are

encased in amorphous Si deposited by sputtering which protects the tubes and sets the gap between the anode and the nanotubes (cathode). Finally, an Au layer of 100 nm is evaporated on top of the sputtered Si. Electron-beam lithography is used to define a grid structure which is transferred to the Au layer by ion beam milling. The tubes are finally exposed by etching the sputtered Si away. This also leaves a suspended, integrated metal grid to extract electrons.

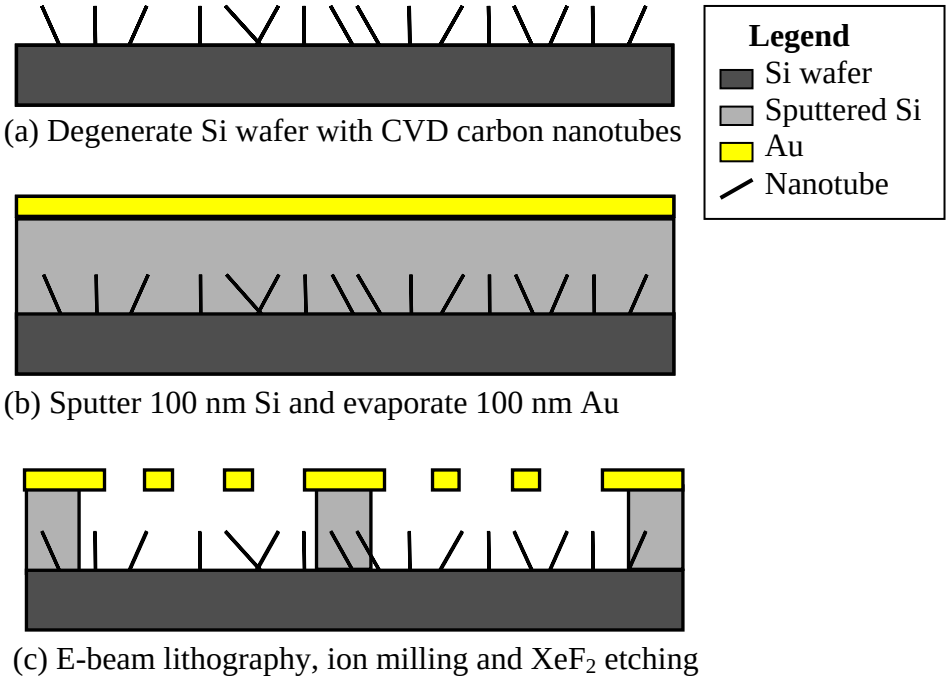

Figure 4.16: Fabrication of integrated grid above CVD grown carbon nanotubes.

The design of the grid involves some trade-offs. The strength and durability of the suspended grid increases as the size of the holes decreases, for a particular lattice constant. This is desirable for the purpose of structural integrity. However, the grid will collect some of the electrons emitted from the carbon nanotube film. Larger grid holes leave less area filled by the grid, and therefore less electrons collected. The fill factor of

the grid will be optimized in future generations of the device. Possibly the most efficient grid structure will lie below the field emission tips.

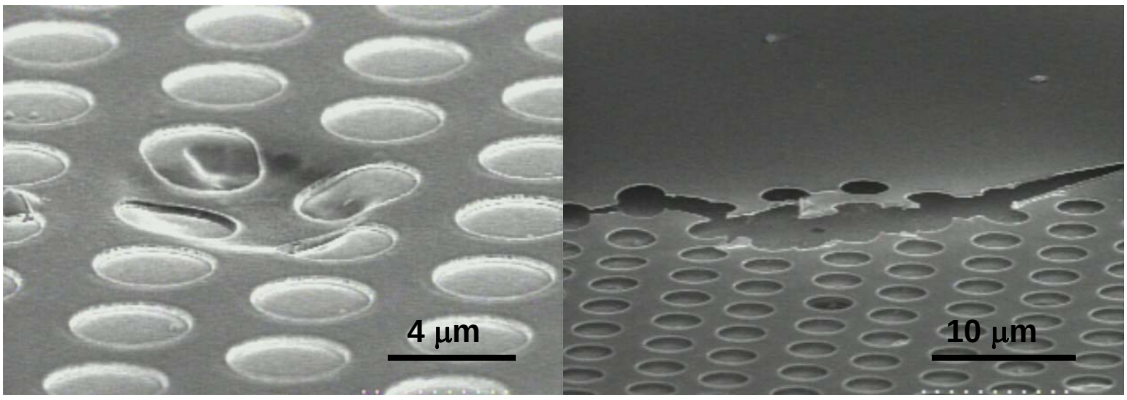

Figure 4.17: SEM images of buckled and torn grids for CNT field emission device.

An issue that has arisen in this process is stress within the evaporated gold layer. Figure 4.17 shows SEM pictures of a buckled and broken grid structures. Grids damaged in this way are not usable because they are shorted to the nanotubes or the degenerate Si wafer. A thicker gold layer may be more stiff and robust to avoid this problem. Also, the holes were close enough together that the grid was completely undercut by the isotropic XeF_2 etch. Eliminating grid holes in a few locations would create supports for the grid as shown in Figure 4.16c.

Some samples were successfully fabricated with integrated grids as shown in the SEM images of Figure 4.18. Unfortunately, all samples that were loaded into the vacuum chamber were not testable because the grid became shorted to the chip. Figure 4.19 shows the sample after being removed from the vacuum chamber. For some reason, the grids collapse within the test setup, perhaps from vibrations of the chamber during pumping. The next generation will use a thicker metal grid layer for increased stability

and robustness. As of this writing, collaborators Dr. Harish Manohara of JPL and undergraduate Wei Dang of Caltech are continuing to fabricate and test these types of structures for the nanoklystron.

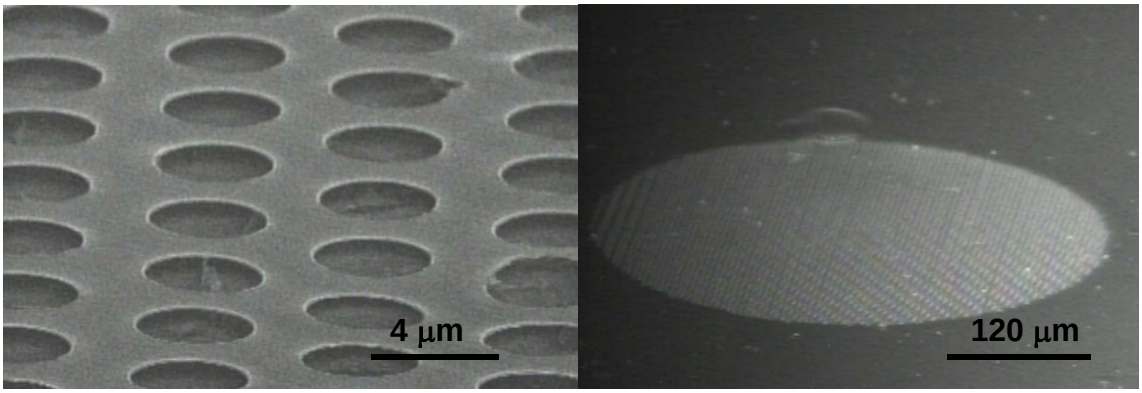

Figure 4.18: SEM images of completed CNT field emission device with integrated grid.

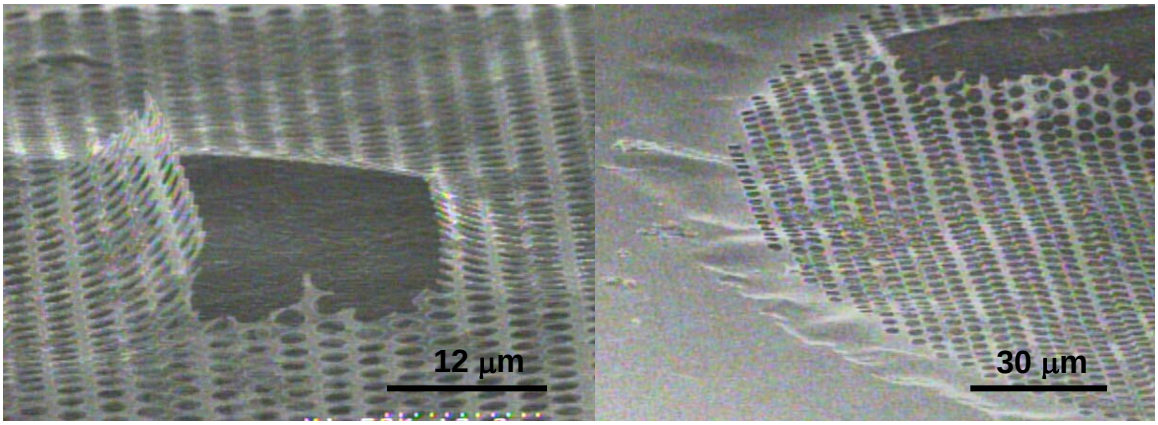

Figure 4.19: SEM images of damaged grids after testing attempt. It is not know exactly when this damage occurred.

4.5 Summary

In this work we have characterized the effects of various microfabrication processes on the conductivity of carbon nanotubes for the purpose of fabricating high-Q nanomechanical resonators. Of the Si etches tested, XeF_2 was found to be the least damaging, while plasma etch processes were the most destructive. Doubly-clamped CNT resonators were fabricated, though not tested. Nanotubes were also explored for field emission and a novel design for integrated extraction grids was fabricated. Both the latter projects are still being pushed forward by collaborators.

References

[1] S. Iijima, "Helical microtubules of graphitic carbon," *Nature* **354** (6348), 56-58 (1991).

[2] S. Iijima and T. Ichihashi, "Single-shell carbon nanotubes of 1 nm diameter," *Nature* **363** (6430), 603-605 (1993).

[3] D. S. Bethune, C. H. Kiang, M. S. de Vries et al., "Cobalt-catalyzed growth of carbon nanotubes with single-atomic-layer walls," *Nature* **363** (6430), 605-607 (1993).

[4] H. Y. Peng, N. Wang, Y. F. Zheng et al., "Smallest diameter carbon nanotubes," *Applied Physics Letters* **77** (18), 2831-2833 (2000).

[5] S. J. Tans, A. R. M. Verschueren, and C. Dekker, "Room-temperature transistor based on a single carbon nanotube," *Nature* **393** (6680), 49-52 (1998).

[6] H. W. Ch. Postma, T. Teepen, Z. Yao et al., "Carbon nanotube single-electron transistors at room temperature," *Science* **293** (5527), 76-79 (2001).

[7] H. J. Dai, J. H. Hafner, A. G. Rinzler et al., "Nanotubes as nanoprobes in scanning probe microscopy," *Nature* **384** (6605), 147-150 (1996).

[8] P. A. Williams, S. J. Papadakis, A. M. Patel et al., "Fabrication of nanometer-scale mechanical devices incorporating individual multiwalled carbon nanotubes as torsional springs," *Applied Physics Letters* **82** (5), 805-807 (2003).

[9] A. N. Kolmogorov and V. H. Crespi, "Smoothest bearings: Interlayer sliding in multiwalled carbon nanotubes," *Physical Review Letters* **85** (22), 4727-4730 (2000).

[10] T. Rueckes, K. Kim, E. Joselevich et al., "Carbon nanotube-based nonvolatile random access memory for molecular computing," *Science* **289** (5476), 94-97 (2000).

[11] H. W. Kroto, J. R. Heath, S. C. O'Brien et al., "C-60 - Buckminsterfullerene," *Nature* **318** (6042), 162-163 (1985).

[12] A. Thess, R. Lee, P. Nikolaev et al., "Crystalline ropes of metallic carbon nanotubes," *Science* **273** (5274), 483-487 (1996).

[13] M. M. J. Treacy, T. W. Ebbesen, and J. M. Gibson, "Exceptionally high Young s modulus observed for individual carbon nanotubes," *Nature* **381** (6584), 678-680 (1996).

[14] P. G. Collins and P. Avouris, "Nanotubes for electronics," *Scientific American* **283** (6), 62 (2000).

[15] J. M. Bonard, H. Kind, T. Stockli et al., "Field emission from carbon nanotubes: the first five years," *Solid-state Electronics* **45** (6), 893-914 (2001).

[16] T. W. Ebbesen and P. M. Ajayan, "Large-scale synthesis of carbon nanotubes," *Nature* **358** (6383), 220-222 (1992).

[17] J. Kong, H. T. Soh, A. M. Cassell et al., "Synthesis of individual single-walled carbon nanotubes on patterned silicon wafers," *Nature* **395** (6705), 878-881 (1998).

[18] S. S. Fan, M. G. Chapline, N. R. Franklin et al., "Self-oriented regular arrays of carbon nanotubes and their field emission properties," *Science* **283** (5401), 512-514 (1999).

[19] J. M. Bonard, T. Stockli, O. Noury et al., "Field emission from cylindrical carbon nanotube cathodes: Possibilities for luminescent tubes," *Applied Physics Letters* **78** (18), 2775-2777 (2001).

[20] J. Kong, N. R. Franklin, C. W. Zhou et al., "Nanotube molecular wires as chemical sensors," *Science* **287** (5453), 622-625 (2000).

[21] S. Sapmaz, Y. M. Blanter, L. Gurevich et al., "Carbon nanotubes as nanoelectromechanical systems," *Physical Review. B, Condensed Matter and Materials Physics* **67** (23), art.no.-235414 (2003).

[22] P. H. Siegel, T. H. Lee, and J. Xu, ""The Nanoklystron: A new concept for THz power generation," *JPL New Technology Report* (2000).

[23] M. S. Dresselhaus, G. Dresselhaus, and Phaedon Avouris, *Carbon nanotubes : synthesis, structure, properties, and applications*. (Springer, Berlin ; New York, 2001), pp.xv, 447.

Appendix

Photonic crystal lasers:

future integrated devices

5.1 Introduction

The technology of photonic crystals has produced a large variety of new devices. However, photonic crystals have not been integrated with mechanical structures or bottom-up nanomaterials. Both approaches have the potential to create novel devices.

The photonic crystal we have fabricated is a suspended slab of material. In a sense it already has a micromechanical aspect. The optical properties can be used with mechanical structures. The photonic crystal laser could be used for integrated optical detection of a nanoresonator beam. The principles of nanomechanical systems could also be used to improve the performance of the laser. For example, heating of the laser limits its performance. The periodic dielectric structure of the photonic crystal laser modifies not only the optical band structure, but also the phononic band structure. Engineering of both band structures simultaneously could increase the heat dissipation, allowing continuous wave lasing.

Photonic crystals can also be constructed out of bottom-up materials. Researchers have built microwave frequency waveguides using “log cabin” stacked dielectric rods.[1] However, it is a challenge to create these at optical frequencies. Metallic nanowires

could serve as the building blocks for such a structure. The hardest challenge of such an experiment is actually the fabrication of the device. Many possibilities for synergy exist between photonic crystals and nanomaterials.

5.2 Basics of photonic crystals

Photonic crystals utilize periodic changes in the index of refraction to engineer the band structure for electromagnetic waves. They have been an extremely active area of research since the pioneering work of Yablonovitch.[2] Photonic crystals have been utilized to create a variety of light trapping devices such as waveguides[3], lasers[4], and optical cavities for cavity quantum electrodynamics.[5] Research is currently underway to apply photonic crystals to diverse fields from atom trapping[6] to chemical sensing.[7] Groups have also fabricated photonic crystal optical fiber[8], some of which trap light in air, rather than dielectric.

The electronic band gap that arises in crystal lattices of atoms is a well known phenomenon that has yielded the incredible advances in computing of the later 20th century. An analogous effect exists with regard to photons. By constructing a periodic lattice of contrasting index of refraction, one can create a material with a photonic band gap, where certain frequencies of light are forbidden from propagating through the material. So called “photonic crystals” have the potential to lead another revolution in information processing, where electrons are replaced by photons. The photonic bands that lie above and below the gap can be referred to, in analogy to solid state physics, the “conduction” band and the “valence” band, respectively.

Photonic crystals have been constructed with band gaps in one, two and three dimensions.[9] The Bragg mirror is an early incarnation of a photonic band gap structure, used to reflect a specific wavelength of light. The mirror is constructed by stacking alternating layers of two materials with different indices of refraction. Each layer has a thickness corresponding to ¼ of the wavelength of the light to be reflected. The constructive and destructive interference of the reflections off of each layer prevent the corresponding wavelength from propagating. The "quarter-wave stack" forms the basis for devices such as the Fabry-Perot filters and distributed feedback lasers.

Maxwell's equations, the basic laws that describe the propagation of light, are scalable in the absence of free charges and currents. Therefore, in theoretical analysis of photonic crystals it is common to normalize physical dimensions by the lattice spacing of the photonic crystal *a*. In this chapter we will refer to the normalized hole radius *r/a* and the normalized slab thickness *d/a* when considering the design and tuning of the device. In addition, a normalized frequency can also be defined,

$$\omega^n = \frac{a\omega}{2\pi c} = \frac{a}{\lambda_0}$$

where ω is the angular frequency, c is the speed of light, λ_0 is the wavelength in vacuum. For fixed normalized dimensions, the wavelength scales with the lattice spacing.

5.3 Design

There are several ways to analyze the behavior of light in periodic structures including solving an electromagnetic master equation[10] and using plane wave

expansion.[11] Another common method is the use of finite-difference time-domain (FDTD) simulation.[12] In an FDTD calculation the spatial and time dimensions are discretized with a fine mesh. Then at each time step the electric and magnetic field and their time derivatives are calculated. This process is iterated to yield the propagation of electromagnetic radiation through the crystal. All the calculations presented here were performed by Dr. Oskar Painter, a senior graduate student at the time.

The microcavity studied here is formed from two basic building blocks: a dielectric slab and a 2-D photonic crystal. The slab provides in-plane confinement through total internal reflection. The photonic crystal alters the propagation of light, with certain frequencies that cannot propagate through the periodic structure. Since the slab is only about half a wavelength thick, the finite thickness of the 2-D photonic crystal must be taken into account.

The 2-D lattice employed in this work is a triangular lattice of air holes in a dielectric material. An ideal 2-D photonic crystal with infinite thickness has modes which can be classified transverse electric (TE) or transverse magnetic (TM), where the electric or magnetic field, respectively, is parallel to the 2-D plane of the photonic crystal lattice.[13] For a finite thickness 2-D photonic crystal the modes are classified even or odd, with respect to the horizontal mirror plane in the center of the slab. For the lower lying bands of the ideal lattice, the even and odd modes guided by the slab may be termed TE-like and TM-like, respectively.[14]

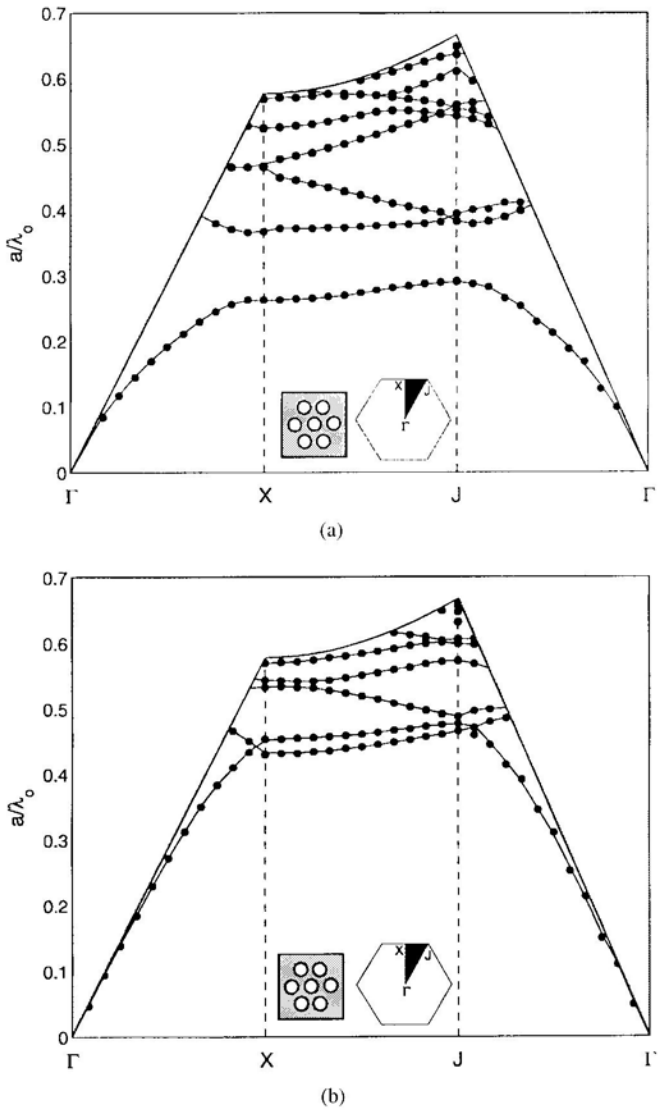

Figure A.1: In-plane band structure of triangular lattice of air holes in a dielectric slab. (a) TE-like modes (b) TM-like modes The parameters used to calculate these band diagrams are r/a = 0.32, d/a = 0.409, n_{slab} = 3.4 and n_{air} = 1.

The in-plane band structure of the triangular lattice photonic crystal is shown in Figure A.1, computed by FDTD simulation. The parameters used in this calculation are: r/a = 0.32, d/a = 0.409, n_{slab} = 3.4 and n_{clad} = 1. The shaded regions in the plots of Figure A.1 are above the light line of photons in the air cladding. Photons with

wavelength and in-plane *k*-vector above the light line can propagate in air, so that these modes are leaky modes. The bands plotted below the light line represent guided modes of the photonic crystal. Comparing the allowed modes in Figures 1a and 1b, we can see that the TE-like modes have a photonic band gap at certain normalized frequencies around 0.3 while the TM-like modes have no band gap. This is favorable for the purposes of creating a defect laser cavity, for it reduces the number of high Q modes, decreasing the threshold for lasing.

The band gap for TE-like modes results in a range of optical frequencies which cannot propagate through the photonic crystal. By removing a single air hole from the center of a triangular lattice, a defect is formed which acts as a potential well and resonant cavity for photons. The photonic crystal surrounding the resonant cavity acts as a mirror for wavelengths within the band gap. Figure A.2 shows a schematic of the device. The power that is radiated in the form of photons from the defect cavity can be divided into a component that escapes out vertically from the slab and a component that tunnels through the finite periods of the photonic crystal. The latter leakage can be improved by adding layers to the lattice, till scattering and absorption begin to dominate the losses. The photons that leak vertically from the waveguide impose a greater limitation on the *Q* factor of the cavity. Smaller air holes increase the effective index of the slab, improving in-plane confinement. The *Q* calculated from FDTD simulation for the devices studied here is 500-600.

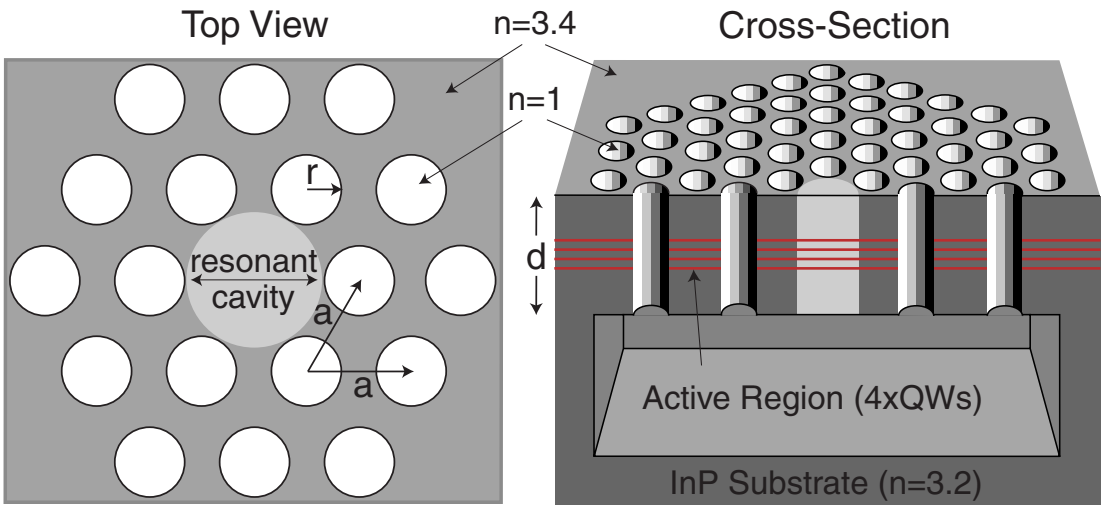

Figure A.2: Left—top view of photonic crystal defect laser showing triangular lattice and cavity with missing hole. Right—cross section of device showing suspended structure and quantum wells for optical gain.

To create a structure that exhibits lasing, there are two main components: a high-Q optical cavity and an optical gain material. The optical medium selected for this device is eptiaxially grown III-IV semiconductor material with quantum wells. Electron-hole pairs are excited by optical pumping. The quantum wells provide a region where electron-hole recombination can emit photons into the cavity modes. Details of the epitaxy can be found in Section 5.5.

5.4 Tuning

The effects of the in-plane confinement on the wavelength of cavity modes can be approximated by separating the in-plane and vertical components of momentum,

$$\omega^2 \approx \omega_{2D}^2 + \left(\frac{c}{n_{eff}^z}\right)^2 k_z^2$$

where ω_{2D} is the in-plane frequency of the confined mode, $k_z = 2\pi/\lambda_z$ is the wavevector corresponding to the vertical confinement, and n^z_{eff} is the effective index determined by the overlap between the perforated slab and the field pattern of the 2D mode. The fundamental guided mode of a dielectric slab, for strong confinement, has $\lambda_z = 2d$. Substituting into equation (2) and normalizing as proscribed by equation (1), we find

$$\omega^n \approx \sqrt{\left(\omega^n_{2D}\right)^2 + \left(\frac{1}{2n^z_{eff}}\right)^2 \left(\frac{d}{a}\right)^{-2}} \quad .(1)$$

For the defect cavities fabricated in this work, the thickness d is constant. Therefore with constant r/a, the normalized frequency will increase with increasing lattice spacing a.

The change in the in-plane frequency component with r/a is more complicated due to its effect on the band structure of the crystal. It can be argued that as r/a increases, the frequency increases due to the reduced fraction of dielectric material. In this work we vary the parameters a, d/a and r/a to measure their effect on the photonic crystal defect modes.

5.5 Fabrication

The geometry of this device is a perforated slab of optical semiconducting material. The material must provide the light emission which will be trapped in the photonic crystal defect cavity. This is achieved by the presence of quantum wells. In addition, the material must have low surface recombination of electrons and holes. Surface recombination is not light emitting, so it reduces the pumping efficiency of the device. This process is particularly important because the geometry of this device results

in a large surface area to volume ratio. Light is trapped in-plane by total internal reflection, which is maximized by having air cladding on both sides of the slab. To create a suspended slab of material, a sacrificial layer is included.

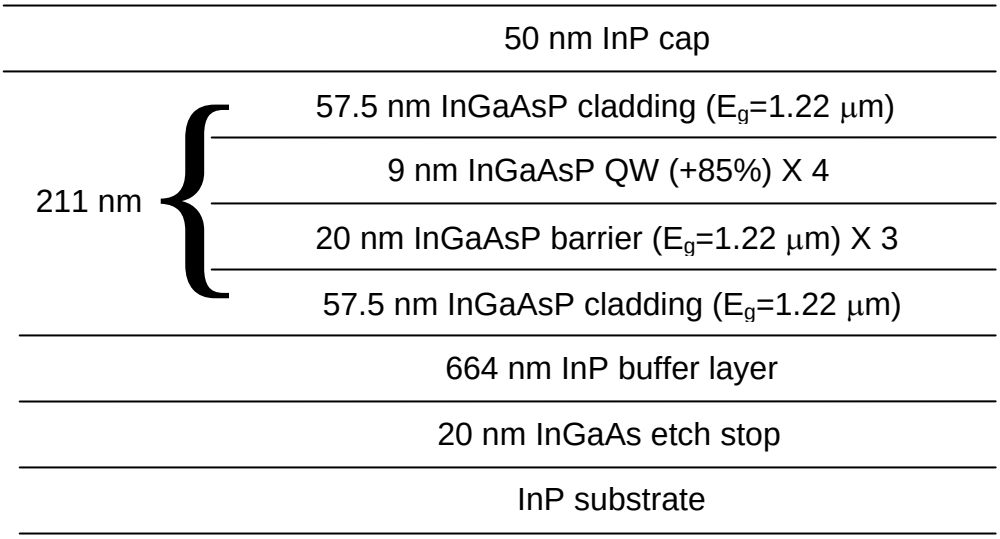

Figure A.3: Schematic of epitaxial layers for defect lasers.

Figure A.3 depicts the epitaxial layers of the wafer used to fabricate this device. Collaborators J. D. O'Brian and P. D. Dapkus at USC used metal-organic chemical vapor deposition (MOCVD) to grow the epitaxial layers on an InP substrate. Going up from the InP substrate, the epitaxy contains a thin InGaAs etch stop layer, InP sacrificial layer, four quantum wells with barrier layer, and finally a InP cap. The quantum wells are comprised of 0.85% compressively strained InGaAsP layers with peak emission at 1.55μm. The barriers between the quantum wells are also InGaAsP with a bandgap corresponding to photons of wavelength 1.22μm. Two cladding layers identical to the barrier layers surround the quantum wells, further isolating them from the surface and

increasing the total thickness of the final device. The InP buffer layer will be etched away to leave a suspended slab structure at the end of the fabrication.

A series of mask layers is used to transfer a perforation pattern through the active region to the InP sacrificial layer. Electron beam lithography defines the pattern in a 100 nm resist layer of 2% polymethyl methacrylate (PMMA). Argon ion beam etch transfers the pattern to an underlying metal layer of Cr/Au. Next, a C_2F_6 reactive ion etch (RIE) is used to etch the holes into a SiO_2 layer. The final dry etch step is a Cl_2 chemically assisted ion beam etch (CAIBE) that perforates the optical material through to the InP sacrificial layer. To suspend the patterned slab, the InP sacrificial layer must be reomoved. A gently agitated hydrochloric acid (4:1) solution is used to selectively etch away the InP, leaving the photonic crystal structure surrounded by air.

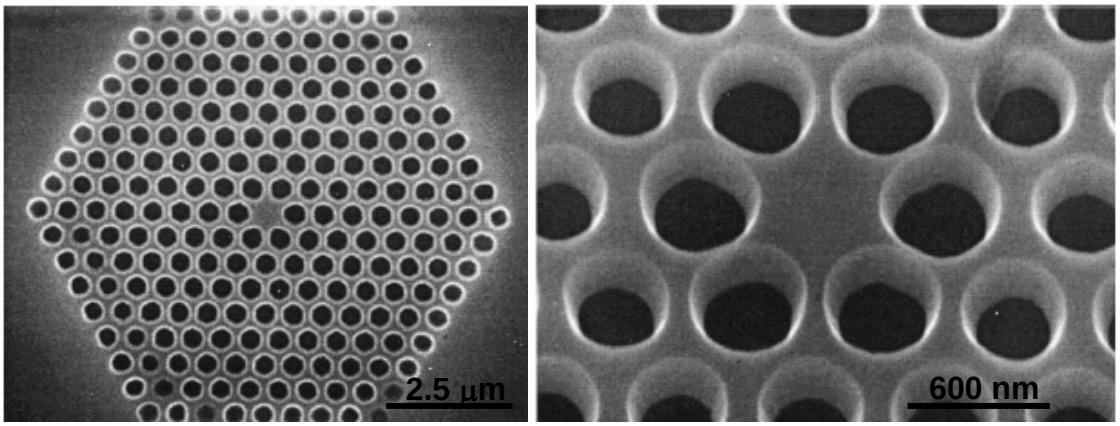

Figure A.4: Left—completed photonic crystal. Right—detail of defect area of device.

SEM images of completed devices is shown in Figures 4 and 5. The fabrication process results in a suspended slab of optical material perforated with a triangular lattice of holes 8 periods deep surrounding a single missing hole in the center. We fabricated an

array of devices varying the lattice constant *a* and the hole radius *r*, shown in Figure A.5. The average diameter of each device was about 8 mm and they were space by 10 mm. The lattice constant is varied from 564 nm to 470 nm and the normalized hole radius *r/a* for each lattice spacing is varied from 0.30 to 0.37.

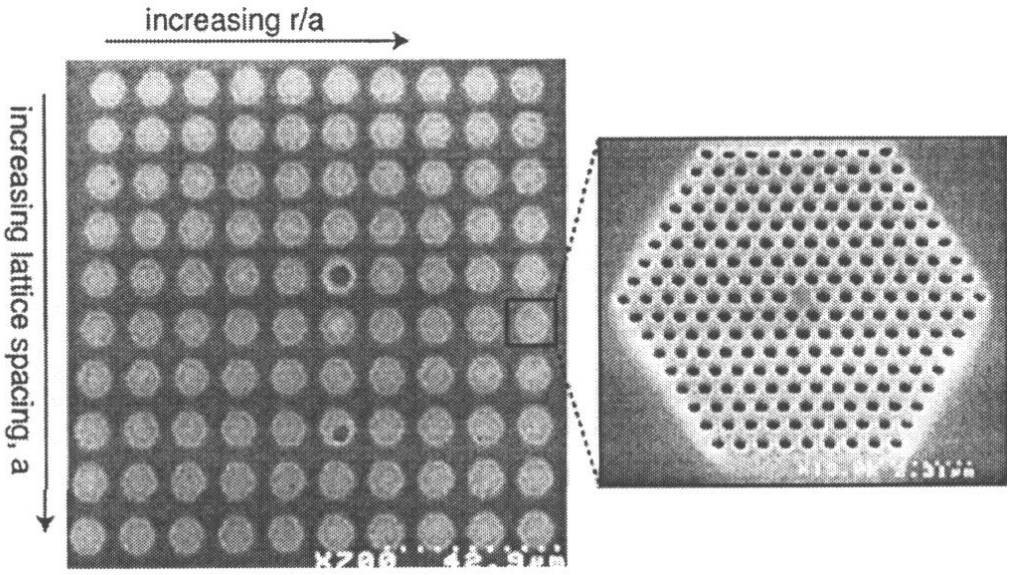

Figure A.5: Array of photonic crystal devices with magnification of one device. The lattice constant is varied from 564 nm to 470 nm and the normalized hole radius *r/a* for each lattice spacing is varied from 0.30 to 0.37.

5.5 Measurement

To pump this structure, electrons within the quantum wells must be excited to the conduction band. They then relax to the valence band, emitting light of a frequency corresponding to the band gap of the quantum well. If the defect mode of the cavity has

the same frequency, the light will resonate in the defect cavity. If the cavity Q is high enough, the trapped light will cause stimulated emission from the quantum wells, resulting in lasing.

The sample was mounted on an X-Y-Z stage and illuminated with light from an 830 nm semiconductor laser diode at a normal incidence. A high numerical aperture, long working distance 100X lens is used to image the devices, focus the pump light and collect the resulting photoluminescence (PL). The spot size of the beam can be focused down to 1 μm, though a 4 μm spot size provided the lowest lasing threshold. This is because a larger spot size pumps the surrounding quantum wells in the photonic crystal to transparency so that they doesn't absorb the evanescent light from the defect mode. A spot size of 4 μm was used throughout this work. The collected light is filtered by a GaAs wafer to remove the pump beam and then fed into an optical spectrum analyzer (OSA).

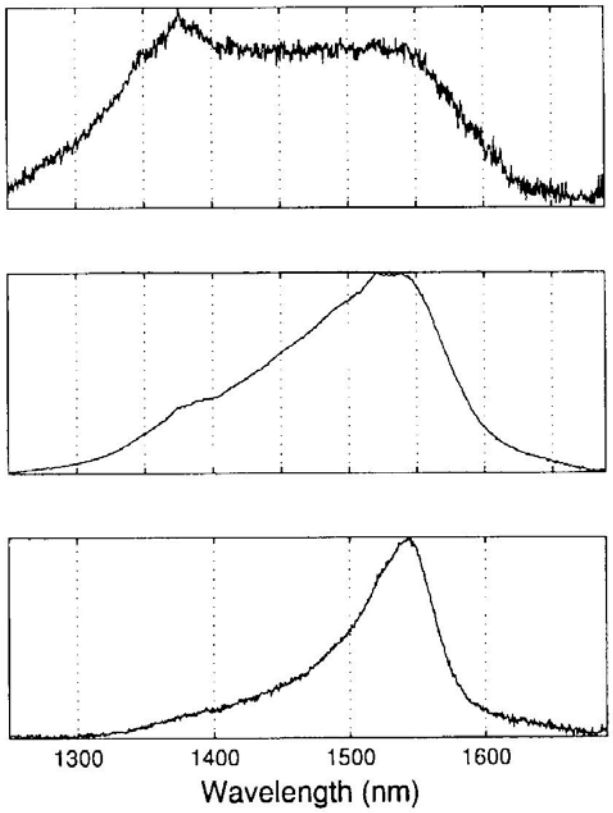

Figure A.6: Photoluminescence at three pump powers for an unpatterned area on the substrate with 4 mm spot size. The bottom plot corresponds to 20 μW continuous wave pump power. The middle plot is 170 μW pump power with a 50% duty cycle. The top plot is the PL for 7 mW peak pump power with 10 ns pulses and 3 μs period, the same pumping as used for testing the defect cavity lasers.

We first pumped and collected at an unprocessed, unpatterned area of the sample to measure the PL in the absence of photonic crystal, plotted in Figure A.6. The peak pump power is increased from bottom to top in Figure A.6. At low pump power the peak emission is at 1545 nm corresponding to the lowest energy level in the quantum wells, as shown in the bottom plot of Figure A.6. At higher pump power, shown in the middle plot, another peak at 1380 nm appears, corresponding to the first excited state of the

quantum well. At pumping conditions identical to those used for these experiments (7 mW peak power, (10 ns pulse with a 3 μs period) the PL is quite broad covering almost a 400 nm range, as shown in the top plot of Figure A.6. The broadening arises due to heating of the substrate at high pump power. The broadening is useful in that it expands the range of frequencies that the quantum wells will emit into, though heating also increases the amount of non-radiative recombination of electrons and holes.

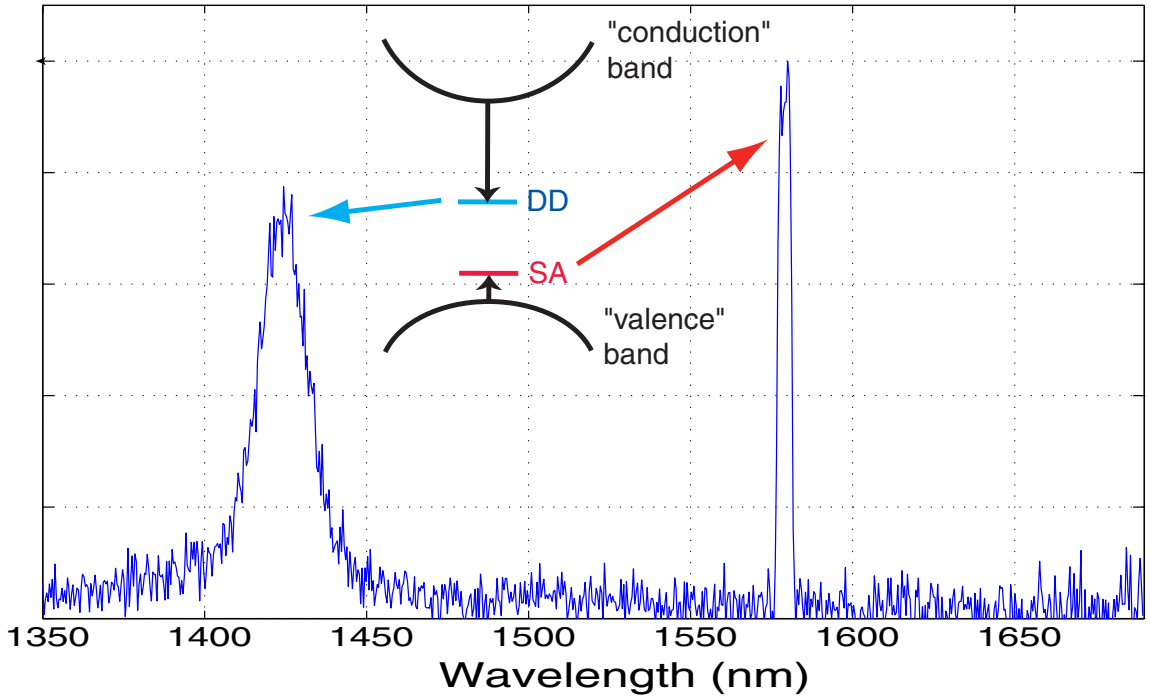

Figure A.7: Sub-threshold photoluminescence from a typical photonic crystal defect cavity.

The PL from the photonic crystal defect cavity devices was markedly different. Figure A.7 shows the PL from a typical device. The photonic crystal suppresses emission into the photonic band gap except for two resonance peaks that correspond to defect

cavity modes. The inset shows a schematic of the band structure showing where the two modes lie relative to the photonic band gap. The longer wavelength mode at 1580 nm corresponds to a weakly localized shallow "acceptor" (SA) mode, while the other is a strongly localized pair of degenerate deep "donor" (DD) modes at 1425 nm.

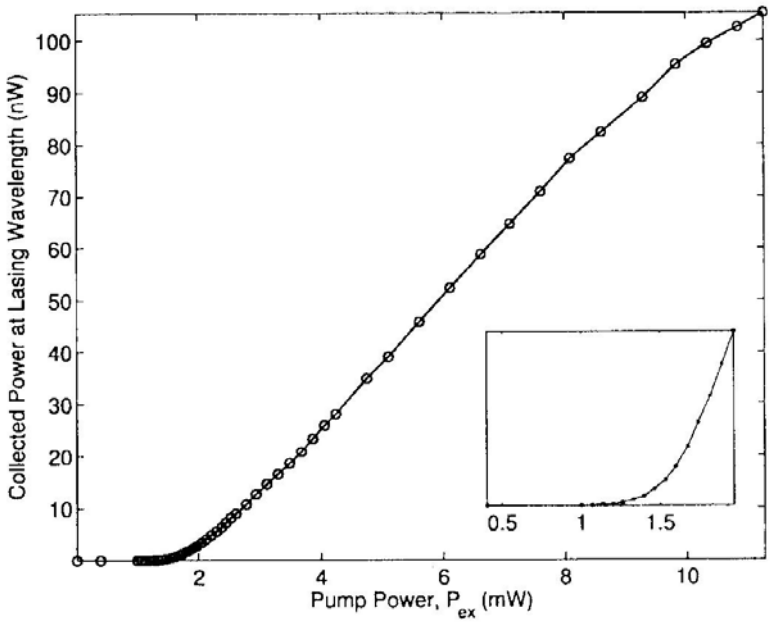

Figure A.8: Collected lasing optical power at 1580 nm vs. external peak pump power of a defect cavity device.

Each device was tested for lasing by pumping it with the diode laser at 7 mW peak pump power with 10 ns pulses and 3 μs period. The lasing from each defect cavity was always the longer wavelength SA mode, due to a theoretical Q five times that of the DD modes. The collected light power is plotted versus the peak pump power to show the lasing threshold. The inset gives a magnified plot of the "knee," showing that the threshold pump power is 1.5 mW, from which we estimate an absorbed power of 500 μW due to reflections from the lens and sample surface. Lasing was obtained for duty cycles of up to 1%, corresponding to a 30 ns pulse. Lasing at higher duty cycles does not occur probably because of heating in the suspended membrane. The membrane is poorly heat

sunk so that nonradiative Auger recombination, which increases exponentially with temperature, consumes the excited electrons and holes in the quantum well.

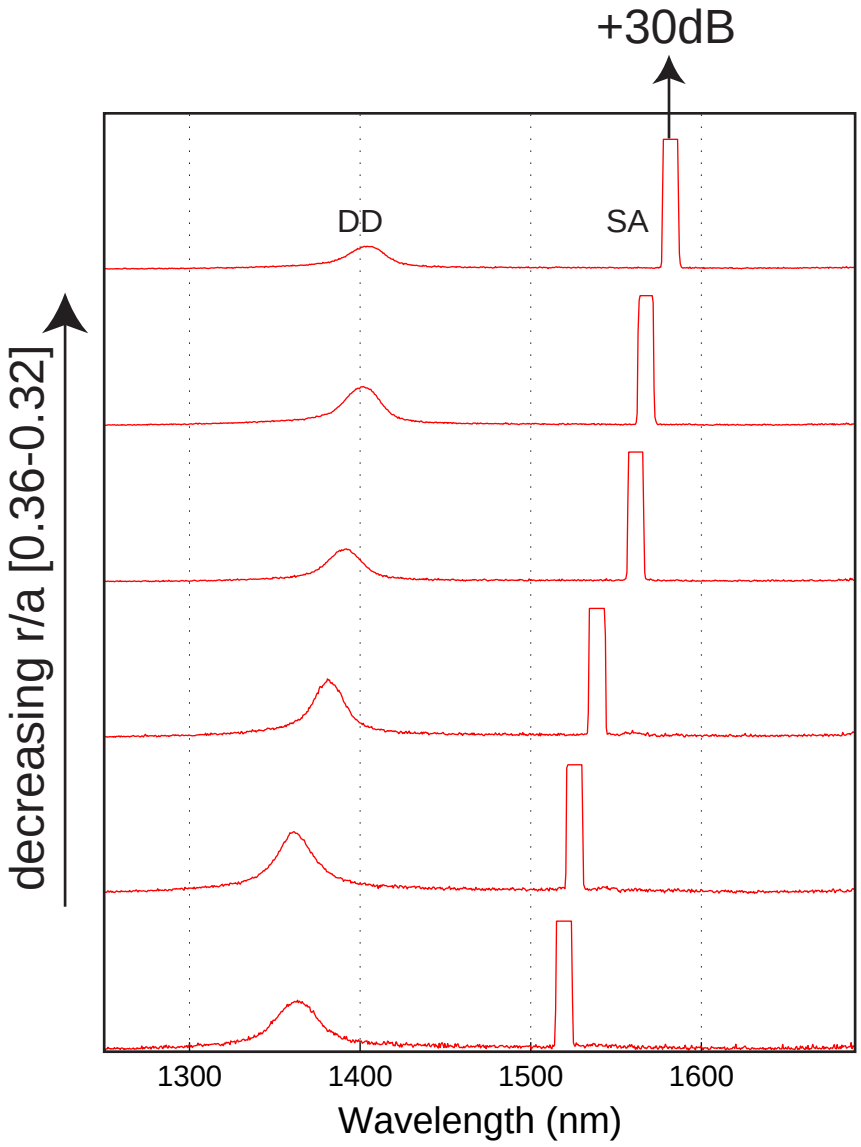

Figure A.9: Photoluminescence from a set of defect cavities, showing tuning as a function of *r/a*. The lattice spacing in this case is 490 nm while the radius of the air holes ranges from 165 nm to 150 nm.

The PL for a set of devices with constant lattice spacing of 490 nm and r/a that varies from 0.36 to 0.32 is shown in Figure A.9. As the normalized hole radius is

decreased both the SA and DD modes increase in wavelength as expected. The lasing wavelength of the SA modes can be tuned lithographically from 1520 nm to 1580 nm. The lasing wavelength increases by about 10 nm for a reduction of the diameter of the air holes by about 5 nm, close to the resolution of our lithography.

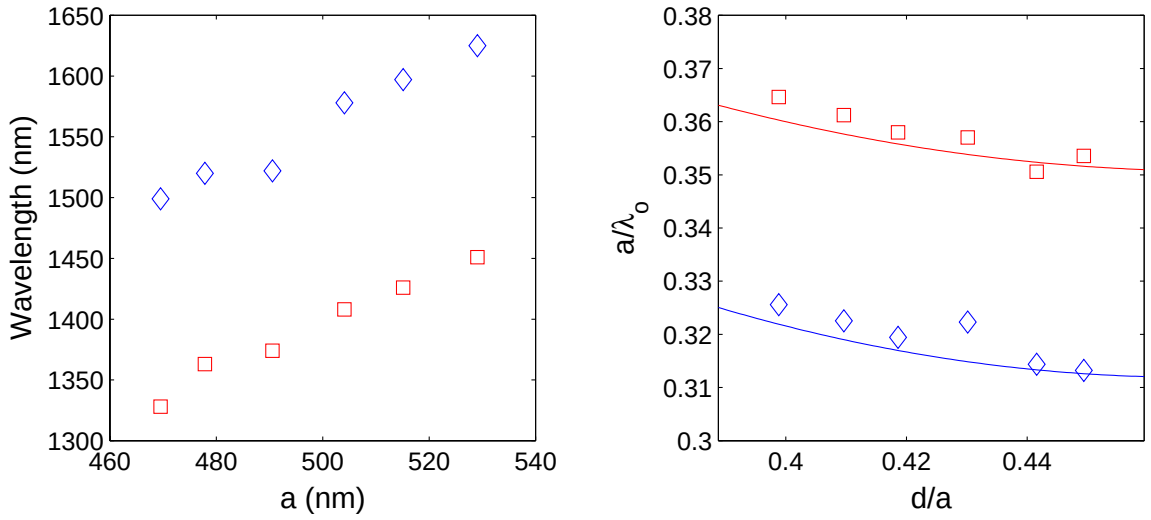

Figure A.10: Left—emission wavelength for SA laser peak (diamonds) and DD peak (squares) for increasing lattice spacing. Right—SA and DD wavelengths for normalized slab thickness. The lines plot FDTD simulations of the SA and DD mode frequency.

If the normalized hole radius *r/a* is held constant at 0.35, then varying the lattice constant will vary the normalized slab thickness *d/a*. Figure A.10 plots the wavelength of the SA and DD photoluminescence peaks as a function of the lattice constant, and in the right graph, plots the corresponding normalized frequency a/λ_0 versus *d/a*, both for fixed *r/a*. Due to the scaling of Maxwell's equations, the wavelength increases with *a* as expected. Also, the normalized frequency decrease slightly with increasing *d/a* as predicted by equation (1). The dashed curves in the right plot of Figure A.10 show the

theoretical predictions of the locations of the SA and DD from FDTD simulation which agree well with the measured data.

5.6 Summary

Photonic crystals can be used to create high-Q optical cavities. By adding a gain medium to the structure a laser can be constructed. We have constructed a laser of wavelength about 1.55 μm from a suspended perforated optical slab. The slab is perforated with a triangular lattice of circular air holes. The frequency of the lasing mode can be tuned over 150 nm by varying the lattice spacing, hole radius or slab thickness. Integration of photonic crystals with nanowires and other nanomechanical devices has the potential for revolutionary devices.

References

[1] E. Ozbay, B. Temelkuran, M. Sigalas et al., "Defect structures in metallic photonic crystals," *Applied Physics Letters* **69** (25), 3797-3799 (1996).

[2] E. Yablonovitch, "Inhibited spontaneous emission in solid-state physics and electronics," *Physical Review Letters* **58** (20), 2059-2062 (1987).

[3] M. Loncar, J. Vuckovic, and A. Scherer, "Methods for controlling positions of guided modes of photonic-crystal waveguides," *Journal of the Optical Society of America. B, Optical Physics* **18** (9), 1362-1368 (2001).

[4] M. Loncar, M. Hochberg, A. Scherer et al., "High quality factors and room-temperature lasing in a modified single-defect photonic crystal cavity," *Optics Letters* **29** (7), 721-723 (2004).

[5] J. Vuckovic, M. Pelton, A. Scherer et al., "Optimization of three-dimensional micropost microcavities for cavity quantum electrodynamics," *Physical Review. A* **66** (2), art.no.-023808 (2002).

[6] J. Vuckovic, M. Loncar, H. Mabuchi et al., "Design of photonic crystal microcavities for cavity QED," *Physical review. E, Statistical Physics, Plasmas, Fluids, and Related Interdisciplinary Topics* **6501** (1), art.no.-016608 (2002).

[7] M. Loncar, A. Scherer, and Y. M. Qiu, "Photonic crystal laser sources for chemical detection," *Applied Physics Letters* **82** (26), 4648-4650 (2003).

[8] J. C. Knight, J. Broeng, T. A. Birks et al., "Photonic band cap guidance in optical fibers," *Science* **282** (5393), 1476-1478 (1998).

[9] J. G. Fleming, S. Y. Lin, I. El-Kady et al., "All-metallic three-dimensional photonic crystals with a large infrared bandgap," *Nature* **417** (6884), 52-55 (2002).

[10] R. D. Meade, K. D. Brommer, A. M. Rappe et al., "Electromagnetic Bloch waves at the surface of a photonic crystal," *Physical Review. B, Condensed Matter* **44** (19), 10961-10964 (1991).

[11] H. S. Sozuer, J. W. Haus, and R. Inguva, "Photonic bands: Convergence problems with the plane-wave method," *Physical Review. B, Condensed Matter* **45** (24), 13962-13972 (1992).

[12] P. R. Villeneuve, S. H. Fan, and J. D. Joannopoulos, "Microcavities in photonic crystals: Mode symmetry, tunability, and coupling efficiency," *Physical Review. B, Condensed Matter* **54** (11), 7837-7842 (1996).

[13] J. D. Joannopoulos, Robert D. Meade, and Joshua N. Winn, *Photonic crystals: molding the flow of light*. (Princeton University Press, Princeton, N.J., 1995), pp.ix, 137.

[14] P. R. Villeneuve, S. Fan, S. G. Johnson et al., "Three-dimensional photon confinement in photonic crystals of low-dimensional periodicity," *IEE Proceedings. Optoelectronics* **145** (6), 384-390 (1998).